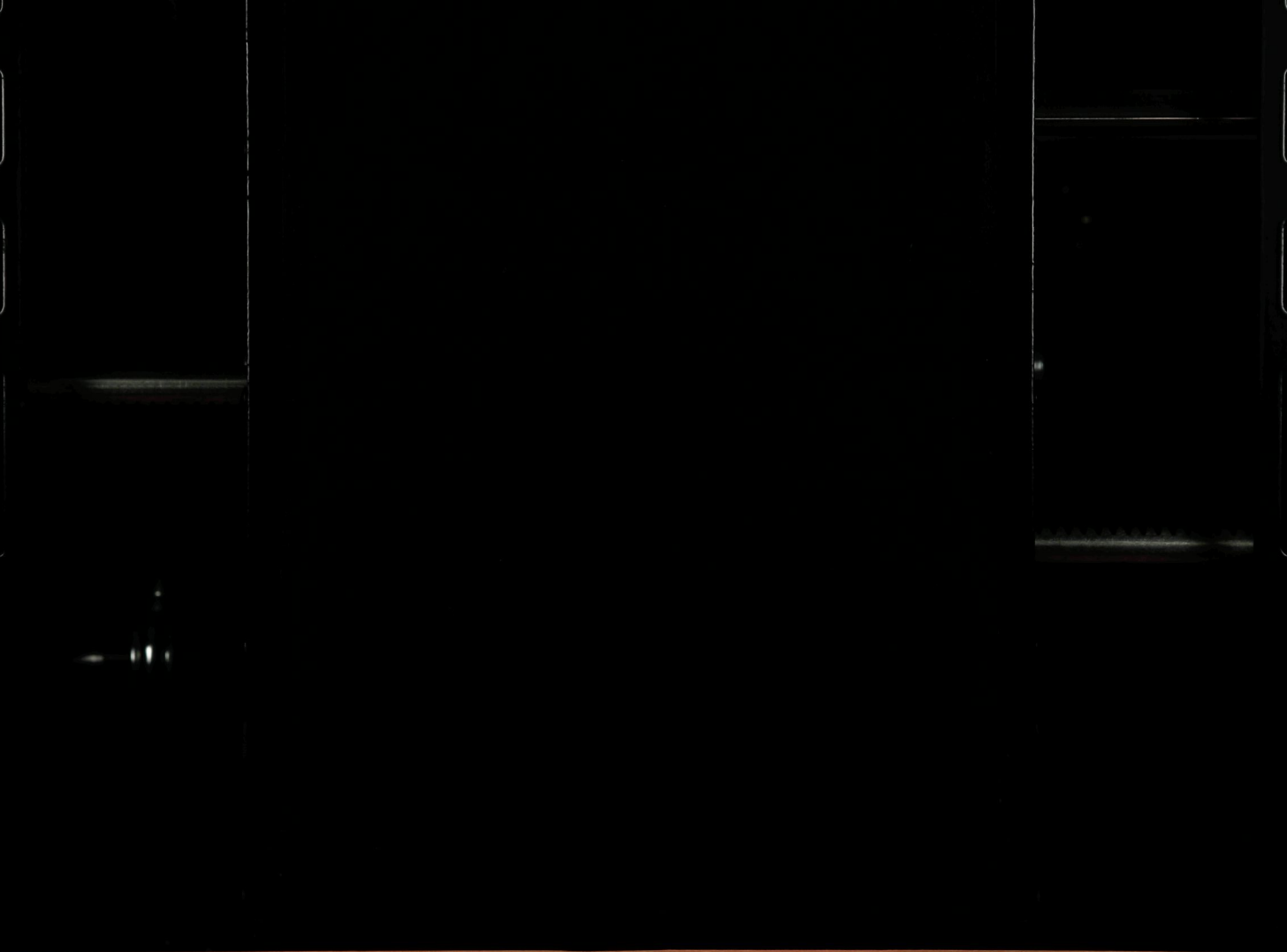

ANL-7632

Argonne National Laboratory

REACTOR DEVELOPMENT PROGRAM PROGRESS REPORT

October 1969

The facilities of Argonne National Laboratory are owned by the United States Government. Under the terms of a contract (W-31-109-Eng-38) between the U. S. Atomic Energy Commission, Argonne Universities Association and The University of Chicago, the University employs the staff and operates the Laboratory in accordance with policies and programs formulated, approved and reviewed by the Association.

MEMBERS OF ARGONNE UNIVERSITIES ASSOCIATION

The University of Arizona	Kansas State University	The Ohio State University
Carnegie-Mellon University	The University of Kansas	Ohio University
Case Western Reserve University	Loyola University	The Pennsylvania State University
The University of Chicago	Marquette University	Purdue University
University of Cincinnati	Michigan State University	Saint Louis University
Illinois Institute of Technology	The University of Michigan	Southern Illinois University
University of Illinois	University of Minnesota	University of Texas
Indiana University	University of Missouri	Washington University
Iowa State University	Northwestern University	Wayne State University
The University of Iowa	University of Notre Dame	The University of Wisconsin

Printed in the United States of America
Available from
Clearinghouse for Federal Scientific and Technical Information
National Bureau of Standards, U. S. Department of Commerce
Springfield, Virginia 22151
Price: Printed Copy $3.00; Microfiche $0.65

ANL-7632
Reactor Technology

ARGONNE NATIONAL LABORATORY
9700 South Cass Avenue
Argonne, Illinois 60439

REACTOR DEVELOPMENT PROGRAM PROGRESS REPORT

October 1969

Robert B. Duffield, Laboratory Director
Stephen Lawroski, Associate Laboratory Director

Division	Director
Chemical Engineering	R. C. Vogel
EBR-II Project	M. Levenson
Metallurgy	M. V. Nevitt
Reactor Engineering	L. J. Koch
Reactor Physics	R. Avery

Report coordinated by
A. Glassner and A. D. Rossin

Issued November 25, 1969

FOREWORD

The Reactor Development Program Progress Report, issued monthly, is intended to be a means of reporting those items of significant technical progress which have occurred in both the specific reactor projects and the general engineering research and development programs. The report is organized in accordance with budget activities in a way which, it is hoped, gives the clearest, most logical overall view of progress. Since the intent is to report only items of significant progress, not all activities are reported each month. In order to issue this report as soon as possible after the end of the month editorial work must necessarily be limited. Also, since this is an informal progress report, the results and data presented should be understood to be preliminary and subject to change unless otherwise stated.

The issuance of these reports is not intended to constitute publication in any sense of the word. Final results either will be submitted for publication in regular professional journals or will be published in the form of ANL topical reports.

The last six reports issued in this series are:

March 1969	ANL-7561
April-May 1969	ANL-7577
June 1969	ANL-7581
July 1969	ANL-7595
August 1969	ANL-7606
September 1969	ANL-7618

REACTOR DEVELOPMENT PROGRAM

Highlights of Project Activities for October 1969

EBR-II

The reactor was shut down on October 16 for scheduled maintenance, installation of reactor modifications, and installation of the instrumented subassembly. It has achieved a cumulative operational total of 30,040 MWd prior to the shutdown.

Preferred orientation induced during fuel fabrication has been found to be responsible for anomalous shortening of vendor-produced Mark-IA fuel during irradiation. The preferred orientation, or texture, is believed to result from stress on the fuel pin during transformation from the gamma to the alpha phase while the pins were being centrifugally bonded. (Pins produced by impact bonding in the cold line of the Fuel Cycle Facility have nearly random orientation and do not shorten during irradiation.) Tests have shown that irradiation shortening of centrifugally bonded pins is prevented by heat treating the pins before they are irradiated.

ZPR-3

After the standard stainless steel matrices were aligned and the new back-mounting plates installed, the construction of Assembly 58 on ZPR-3 began. To study persistent errors in the calculation of central reactivity worths in plutonium cores, two "benchmark" reactors, Assemblies 58 and 59, both simple-composition Pu-carbon cores, will be studied. One will have a depleted uranium reflector; the other will be lead-reflected.

ZPR-6

Calculation of the sodium-void coefficient for Assembly 5, a 2700-liter uranium carbide core, has been made by 1-D and 2-D diffusion methods and compared with measurements. Agreement was within 20% at the core center. Fuel loading of Assembly 6A, a 4000-liter ^{235}U core, is about 80% complete.

ZPR-9

Measurements have been made in three different null-reactivity zones in Assembly 25 to determine capture and fission rates in ^{235}U, ^{239}Pu and ^{238}U. The first two zones involved depleted and enriched uranium, the third depleted uranium and 0.95 kg of plutonium. Reactivity worth of each constituent was measured in each zone; additional materials and other parameters were studied in the first zone.

Assembly 25 has been unloaded from the reactor and preloading for the FTR-3 assembly has begun.

ZPPR

The reactivity worth of the peripheral control ring in FTR-2 has been obtained in a step-wise removal experiment; comparison with calculation has shown satisfactory agreement. Subsequently a sodium-stainless steel shield with an azimuthal span of 80 degrees was added to the full length of the core plus the axial reflector of the assembly. Its reactivity effect was +0.048% $\Delta k/k$. To simulate fuel storage, 25 kg of fissile material of core composition was substituted for shield composition in the shield region. The reactivity effect of the stored fuel was $\leq$0.4 Ih.

TABLE OF CONTENTS

TABLE OF CONTENTS

I. LIQUID METAL FAST BREEDER REACTORS--CIVILIAN

A. Physics Development--LMFBR

1. Theoretical Reactor Physics

a. General Fast Reactor Physics

(i) Reactor Dynamics (D. A. Meneley)

Last Reported: ANL-7618, pp. 2-4 (Sept 1969).

(a) QX1--Coolant-voiding Case. One of the problems associated with the use of reactivity feedback tables in LMFBR safety-analysis codes* is the interdependence of the various feedback terms. An example of such interdependence is that between the Doppler and sodium void. Sodium voiding hardens the spectrum, therefore decreasing the statistical weight of the resonance energy range in the system multiplication. Therefore, in terms of a coefficient formulation of the Doppler feedback, sodium voiding reduces the size of the coefficient. Negative feedback accumulated due to any temperature rise from initial conditions up to the start of voiding is reduced, typically by a factor of two for complete voiding.

A simple model relating the Doppler coefficient to sodium volume fraction has been applied in at least one instance.** This model may be capable of reducing errors such as are described below, due to the interaction effect. It has two weaknesses. First, the local spectral shift depends on the void size as well as on sodium fraction. Second, the temperature dependence of the Doppler feedback varies with spectrum. It is not feasible to construct a reactivity table which accounts for these two effects, either by the criterion of reasonable simplicity or that of reasonable cost. Cost is important because of the large number of static-flux calculations which would be needed to prepare the table entries. If a third interactive feedback term is added, such as gross fuel redistribution in space, the situation degenerates still further. Simple cases may be run with the QX1 code to permit estimates of the magnitude of interaction effects.

The problem described below is based on the same reactor as was studied previously (see Progress Report for July 1969, ANL-7595, pp. 5-7). The initial conditions were changed by setting the axial buckling to zero, then readjusting the zone enrichments in the core

*Fox, J. N., et al., GEAP-5273 (1966); Agrawal, A. K., et al., ANL-7607 (to be published).

**MacFarlane, D. R., et al., Theoretical Studies of the Response of Fast Reactors during Sodium Boiling Accidents, Proc. Int. Conf. on the Safety of Fast Reactors, Aix-en-Provence (1967).

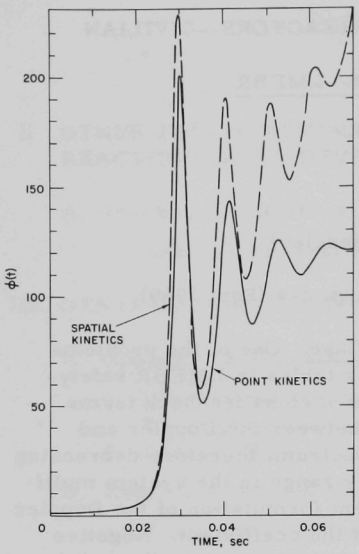

Fig. I.A.1. Amplitude Function following Uniform Sodium Voiding Initiated at t = 0

to obtain a critical system. This was done in order to eliminate uncertainty in the model due to the variation of axial buckling with sodium density. The new critical enrichments (Pu/U+Pu) were 0.12936 and 0.16778 in core zones 1 and 2, respectively. The excursion was initiated by a uniform linear decrease in sodium density with time, going to zero at 0.160 sec. This case is very roughly similar to a flow coastdown accident driven by coolant voiding. The initial reactivity ramp rate defined in the point kinetics sense was \$41.438/sec; however, the reactivity rate was reduced significantly with time due to the nonlinear dependence of diffusion coefficient on sodium density.

The amplitude function for this case is shown in Fig. I.A.1. Referring to the equivalent plot in ANL-7595, Fig. I.B.1, p. 7, it is seen that the discrepancy between point and spatial kinetics at the first peak in that case was around 2%. (This peak-flux discrepancy was found to be independent of ramp rate up to ~\$50/sec.) Figure I.A.1 shows a first-peak discrepancy of over 10%, attributable largely to the neglect of the coolant-void spectrum change in the point kinetics case. The excess energy at 0.070 sec was 47% higher than that given by point kinetics.

(ii) Analysis of Neutronic Characteristics of Reactors and Fuel Cycles (D. A. Meneley)

Last Reported: ANL-7595, pp. 8-12 (July 1969).

At the request of Oak Ridge National Laboratory, mass-balance data have been extracted from two fuel-cycle problems which were done in connection with a small series of survey calculations reported in ANL-7595. The reactor was taken from one of the recent 1000-MWe studies as being representative of a stainless steel clad and structure design with oxide fuel and sodium coolant. The volume fractions were the same as those listed for "Core 1" in Table I.B.4 of ANL-7595, p. 9. Calculations were performed for the "Reference" and "Mo Clad" cases. The two cases were identical geometrically; dimensions are listed in Table I.A.1. Subdivisions of the reactor into burnup regions for the calculation are also shown.

TABLE I.A.1. Reactor Geometry

	Ring	Radium (cm)
Radial Dimensions		
Core Zone 1	1	7.60
	2	20.10
	3	33.11
	4	46.21
	5	59.33
	6	72.46
	7	87.38
Core Zone 2	8	96.98
	9	107.07
Core Zone 3	10	123.70
Radial Blanket	11	136.94
	12	150.21
Reflector	13	163.40

Axial Dimensions (Axial symmetry assumed)[a]

	Region	Height (cm)
Core	1	38.10
Axial Blanket	2	50.80
	3	63.50
	4	76.20
Reflector	5	129.54

[a]Axial regions extend radially through all radial rings. Radial blanket and reflector replace "axial blanket" designations outside outer core radius.

The calculations were carried out with the two-dimensional synthesis fuel-cycle program SYNBURN, which has been checked with favorable results against the direct two-dimensional fuel-cycle code BURN2D.* The equilibrium calculation with fixed feed isotopic distribution was performed; cycle time was adjusted to achieve an average core discharge burnup of 104,500 MWd/MT, and charge enrichment was adjusted so that the unpoisoned k_{eff} at the end of cycle was 1.0. Fluxes were recalculated at each of five time nodes during the converged cycle time of 309.5 full-power days. A tantalum shim control (in ring 9) was adjusted at each of these nodes to maintain criticality. Scatter-reload fuel management was used. In core zones 1 and 2, half the subassemblies were refueled

*Toppel, B. J., ANL-7332 (1967).

at each cycle. In core zone 3, one third were refueled (zone 3 differs from zone 2 only in the batch fraction). The inner radial blanket was refueled in thirds, and the outer in quarters.

Midequilibrium cycle masses are given in Table I.A.2 for the reference reactor and the molybdenum-clad case.

TABLE I.A.2. Midequilibrium Cycle Loadings (kg)

Isotope	Zone 1	Zone 2	Zone 3	Axial Blanket	Radial Blanket Row 1	Radial Blanket Row 2
			(a) Reference Core			
U-235	0	0	0	37	18	22
U-238	5290	2500	2500	14,600	7660	8520
Pu-239	633	387	387	274	160	126
Pu-240	277	182	184	9	5	4
Pu-241	85	65	64	~0	~0	~0
Pu-242	37	25	25	~0	~0	~0
			(b) Molybdenum Clad			
U-235	0	0	0	40	20	23
U-238	5113	2402	2411	14,749	7715	8565
Pu-239	703	453	457	201	117	90
Pu-240	319	215	218	4	3	2
Pu-241	103	82	83	~0	~0	~0
Pu-242	43	29	29	~0	~0	~0

The molybdenum-clad substitution case does not represent a proper redesign of the reference system in any way. For example, it is not clear that a reactor designed for molybdenum clad would have the same fuel volume fractions as the reference case, since each fuel pin design would be based on optimizing the overall system. The whole purpose of the analysis was to estimate the magnitude of penalties involved with such refractory clad substitutions in a reference reactor designed for steel clad.

2. Experimental Reactor Physics

a. Fast Critical Experiments--Experimental Support--Illinois

(i) Pulsed, Cross-correlation, and Noise Measurements (C. E. Cohn)

Not previously reported.

(a) Simple Turn-on Initialization for Digital Systems. When power is applied to a digital system, measures must be taken to insure that the flip-flops in the system will be initialized to the correct state. Also,

destruction of memory contents by the turn-on transient must be prevented. Currently, these functions are performed by various "system normalizers," "initial-condition drivers," and other more or less elaborate arrangements.

The initialization can be done more simply and economically with the power switch arrangement shown in Fig. I.A.2.* Here the power switch is a two-pole, three-position rotary with shorting contacts. The extreme positions of this switch are the OFF and ON positions; the middle position is traversed during every switching operation. One of the poles switches the power, while the other switches the initialization circuit.

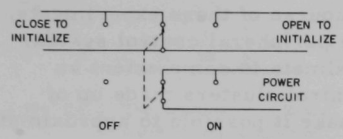

Fig. I.A.2. Power Switch Incorporating Initialization Circuit

In the OFF position, the power circuit is open, but the initialization circuit is closed. On switching to the middle position, the power comes on, but the initialization is held without interruption by the shorting contacts. Switching to the ON position opens the initialization circuit with no interruption to the power.

On turnoff, an analogous sequence takes place. Switching from the ON position to the intermediate position actuates the initialization with no interruption in the power. Switching to the OFF position brings down the power while holding the initialization during the turn-off transient.

The above description applies to an initialization circuit that closes to initialize. A circuit that opens to initialize would be connected differently than shown in Fig. I.A.2. Additional initialization circuits could be connected to additional poles.

Ordinarily, solid-state power supplies come to equilibrium after turn-on in just a few cycles of the line voltage. Therefore, normal operation of the switch would give enough dwell time in the middle position to wait out the turn-on transient, with no conscious pause or hesitation required.

b. FFTF Critical Assembly Experiments--Planning and Evaluation (A. Travelli)

Last Reported: ANL-7618, pp. 6-9 (Sept 1969).

(i) Calculation of the Worths of Various Control Clusters in FTR-2. The worths of peripheral control clusters in FTR-2 are of special interest in the FFTF critical program because such values can be

*Cohn, C. E., Simple Turn-On Initialization for Digital Systems, Electronic Design 17 (No. 13), 78-79 (June 1969).

related directly to the work of the peripheral control system of FFTF and of the next critical assemblies (FTR-3 and engineering mockup). The experiments in which the control ring of FTR-2 was gradually removed in preparation for the shielding experiments provide an excellent test of the computational methods used to calculate the worth of such a control cluster. The experiments are described in detail in Sect. I.A.4.d.

The nominally two-drawer-thick peripheral control ring of FTR-2 was progressively removed in the course of these experiments, in such a manner that the configuration of the peripheral control system resulting at the end of each step would approximate to some extent an intermittent ring of equally spaced square control clusters made up of four matrix tubes. These conditions would make it possible to approximate closely, if not exactly, the FFTF peripheral control system.

The rather large increase in reactivity that accompanied the removal of control material at each step was compensated approximately by depleting a small central region of the core of fissile elements. This procedure made it possible to measure accurately the change in reactivity occurring at every step of the experiment, because the multiplication constant of the reactor was at all times very close to unity.

The calculation of the reactivity worths of various numbers of control ring drawers inserted in 2 x 2 clusters at a position located in the FTR-2 reflector and adjacent to the core boundary was performed in the DIFF-2D diffusion code,* in R-θ geometry and with cross-section set 29601 (see Progress Report for November 1967, ANL-7399, p. 37). This cross-section set contains only six energy groups and is the most convenient set currently available at ANL for use in preliminary calculations of this type, even though it was prepared for a somewhat different composition considered during an earlier stage of the FFTF critical program.

The core and reflector compositions and dimensions used in the calculations were those of Assembly ZPPR/FTR-2 (see Progress Report for April-May 1969, ANL-7577, p. 42; for July 1969, ANL-7595, pp. 24-26). In the R-θ formulation of the problem, a pair of control-ring matrix tubes in the reflector adjacent to the core are represented as the section of an annulus whose radial thickness is the thickness of two drawers and whose angular arc is such that the area of the annular section is equal to the cross-sectional area of two matrix tubes. This section of annulus is placed next to $\theta = 0$, with a reflective boundary. Thus the basic size of the unit of control composition is a cluster of four matrix tubes, occupied by eight drawers. By specifying the other angular boundary of the problem as being reflective and at $\theta = \pi/n$, the resulting configuration considered in the calculation corresponds to a cylindrical core with n four-tube control

*Toppel, B. J., ANL-7332 (1967).

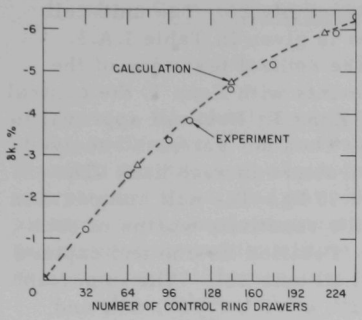

Fig. I.A.3. The Dependence of Reactivity on the Number of Control Drawers in FTR-2

clusters. The values of n = 9, 18, and 27 used in this analysis lead to three of the four calculated points shown in Fig. I.A.3. For each of these points the Δk in percent is the value of k_{eff} calculated in the DIFF-2D problem minus the value of k_{eff} calculated for the same assembly with the control ring replaced by reflector material. The DIFF-1D code was used for the latter problem. In both types of problem the axial leakage was simulated by a DB^2 absorber. The value of transverse buckling used (6.064×10^{-4} cm^{-2}) was the one which, with cross-section set 29601, gave the same k_{eff} for Assembly ZPPR/FTR-2 when the calculation was run for a one-dimensional cylindrical problem as when the calculation was run for a two-dimensional RZ problem (k_{eff} = 1.0048).

Every experimental point in Fig. I.A.3 corresponds to a loading whose k_{eff} was determined experimentally and which was obtained from a previous loading by reducing the number of the control drawers. The abscissa of the point indicates the number of control drawers in the loading. The ordinate of the point indicates, with a reversal of sign, the sum of the changes in reactivity measured during all subsequent removals of control material. Thus, the ordinate of any experimental point corresponds closely to the total worth of the control drawers indicated by the abscissa. This representation does not take into account the effect of the depletion in the small central zone of the core on the worth of the control drawers, nor does it take into account the difference between intermittent annulus of control material and the rather irregular configurations used in the experiments; these effects should be rather small, however, and may be neglected in preliminary calculations.

The comparison of the calculated control worths with the experiments, as shown in Fig. I.A.3, is quite satisfactory. In particular, the figure indicates excellent experimental verification of the curvature of the calculated curve, which indicates the mutual shielding that control clusters exert on each other as they are moved closer and closer together.

3. ZPR-6 and -9 Operations and Analysis

a. Zoned Critical Experiments (L. G. LeSage)

Last Reported: ANL-7618, pp. 9-10 (Sept 1968).

(i) ZPR-9 Assembly 25 Experiments. The experiments with ZPR-9 Assembly 25 have been completed. These measurements were made

for three different null-reactivity zones in Assembly 25. The unit-cell null drawer loadings of each of the null zones is given in Table I.A.3. Zone 1 was loaded first and included the entire central test zone of the assembly. After completion of the measurements with Zone 1, the central 21 drawers in each half were loaded to form Zone 2. Because approval to load more than one kg of plutonium into ZPR-9 had not yet been received, Zone 3 consisted of only the front 3 in. of 5 drawers in each half. The total plutonium loading in Zone 3 was about 0.95 kg. The null composition was carefully determined in each zone, and the reactivity worths of each of the constituent materials were measured. Detailed fission and capture rate measurements were also made in each null unit-cell. The important fission and capture rates, c^{28}/f^{25}, f^{28}/f^{25}, f^{49}/f^{25}, c^{28}/f^{49}, f^{28}/f^{49}, α^{28}, and α^{49} can be determined from this data for the appropriate unit cells.

TABLE I.A.3. ZPR-9 Assembly-25 Null-zone Drawer-loading Arrangements

Zone 1:	1/16 Al, 1/4 D, 1/32 E, 3/8 D, 1/32 E, 1/4 D, 0.025 Al, 0.035 D, 3/16 D, 1/32 E, 3/8 D, 1/32 E, 1/4 D, 1/16 Al
Zone 2:	1/16 Al, 7/8 D, 1/8 E, 7/8 D, 1/16 Al
Zone 3:	1/4 stainless steel frame, 11/16 D, 1/8 ZPR-3 Pu, 3/4 D, 3/16 Al

Note: All dimensions are in inches. E, D, Al, and Pu designate, respectively, enriched uranium, depleted uranium, aluminum (45% dense), and plutonium-aluminum alloy.

The following additional measurements were also made with Assembly 25, Zone 1:

(a) Both α^{25} and α^{49} were measured by the reactivity-reaction rate method.

(b) The perturbation denominator was measured.

(c) The central reactivity worths of a number of additional materials were measured.

(d) Radial ^{235}U, aluminum, and stainless steel reactivity traverses were made to test the spectral convergence in the zone.

(e) The radial and axial activation traverses were made with ^{235}U and ^{238}U foils.

(f) A series of central null-composition reactivity measurements were conducted to check experimentally some aspects of the null-reactivity technique. These measurements were made with both Zone 1 and Zone 2.

b. Coolant Reactivity Experiments (R. A. Karam)

Last Reported: ANL-7513, pp. 15-20 (Oct 1968).

(i) Analysis of Sodium-void Coefficient. The measured values of the sodium-void coefficients in Assembly 5 of ZPR-6, the 2700-liter uranium carbide core, have been reported previously.* Those results have recently been analyzed with ENDF/B data. The analysis reported here pertains to the measurements in the axial direction comprising the determination of the void coefficient in sections 4 in. long in the 9 central drawers per half (equivalent outer radius of 9.35 cm).

Two cross-section sets were generated for the homogeneous composition of Assembly 5 for the configurations with and without sodium. The resonance-region ^{238}U cross sections were corrected in both sets for spatial self-shielding according to equivalence theory. Finally, the sets were weighted with the fine structure of the fluxes in the unit cell.

Three sets of calculations and the measured values are compared in Table I.A.4. The first-order perturbation (FOP), one-dimensional diffusion calculations were performed with the MACH-1 code, using the set

TABLE I.A.4. Measured and Calculated Sodium-void Coefficient as a Function of Axial Direction in Normal Loading of Assembly 5 of ZPR-6

Sections Voided	ΔZ[a] (cm)	Sodium Weight (kg)	Sodium-void Coefficient			
			Measured[b]		Calculated (Ih/kg)	
			Ih/Section	Ih/kg Na	1-D Diffusion[c]	2-D Diffusion[d]
A	0.0-5.08	0.886	1.02	1.15	0.591	0.509[e] (0.797)[f]
B	0.0-10.16	1.772	1.98	1.12	0.582	0.473 (0.779)
C	10.16-20.32	1.955	1.90	0.97	0.420	0.350 (0.628)
D	20.32-30.48	1.955	0.85	0.44	0.116	0.081 (0.333)
E	30.48-40.64	1.955	-0.40	-0.20	-0.287	-0.264 (-0.061)
F	40.64-50.80	1.955	-2.00	-1.02	-0.732	-0.640 (-0.494)
G	50.80	1.955	-2.64	-1.35	-1.161	-0.959 (-0.857)
H	60.96-71.12	1.955	-3.00	-1.54	-1.518	-1.108 (-1.050)
All Sections (Measured or Calculated)	0.0-71.12	13.502	-3.95	-0.293	-0.252[g]	-0.341 (-0.116)
All Sections (Summed)	0.0-71.12	13.502	-3.31	-0.245		

[a]ΔZ is the axial length of each section in each half of the core.
[b]Typical uncertainty in each measurement was 0.10 Ih (1% Δk/k = 476 Ih).
[c]Calculated with the set appropriate to the sodium-in configuration with one-dimensional (1-D) diffusion code and first-order perturbations.
[d]Difference in k calculation.
[e]Calculated with set appropriate to sodium-in configuration.
[f]Calculated with two sets; one for the sodium-in and one for the sodium-out configurations.
[g]Difference in k calculation with change in reflector savings due to sodium removal taken into consideration.

*Karam, R. A., et al., ANL-7310 (1968), p. 167.

appropriate for the sodium-in configuration. In these calculations the unperturbed fluxes, assumed to have a cosine axial distribution, were used. It is seen that the spectral component of the sodium-void coefficient (according to FOP the value in Sect. A is 98% spectral and 2% leakage) is incorrectly predicted. The agreement between the calculated and measured values improved as a function of Z, the axial height. The spectral component fraction of the void coefficient decreases as a function of Z, and in Sect. H the coefficient is 95% leakage and 5% spectral. Thus the improvement in agreement was primarily due to the leakage component and might be fortuitous since the unperturbed fluxes, assumed to have cosine distribution, were used.

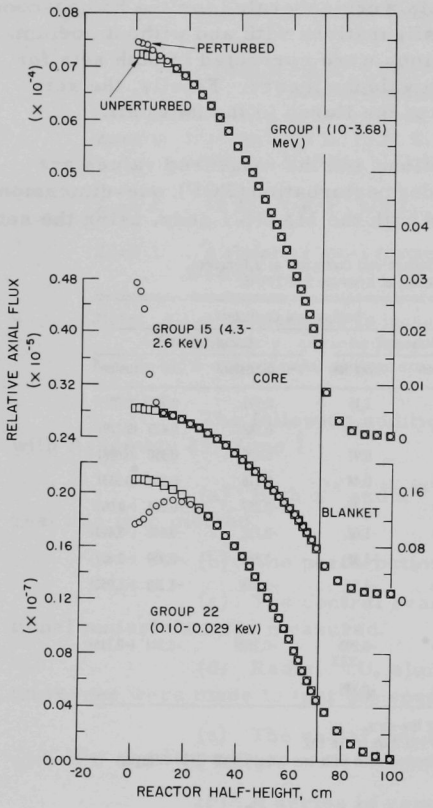

Fig. I.A.4. Comparison of Perturbed and Unperturbed Fluxes due to Sodium Voiding in a 2-in. Section at Core Center

A check on these assumptions was obtained with two-dimensional diffusion, k calculations, using the same cross-section set. The results show that at the core center, where the leakage component is nil, the unperturbed fluxes increased the coefficient by 15-20%. Comparison of the perturbed fluxes due to sodium voiding in Sect. A with the unperturbed fluxes in group 1 (10-3.68 MeV), group 15 (4.3-2.6 keV), and group 22 (0.10-0.029 keV) is shown in Fig. I.A.4. It is seen that the perturbation in groups 1, 15, and 22 is significant. The two-dimensional results also show that the axial distribution of the fluxes does not have a cosine shape.

The last of two-dimensional diffusion, k calculations (values in parenthesis) were obtained using two different cross-section sets: one for the sodium-voided region and one for the normal core composition. Although the size of the voided region may not be large enough to justify the use of cross sections averaged with the fundamental-mode spectrum of the sodium-free core, a difference in k of only 0.2% was calculated with the two sets for the homogeneous composition of Assembly 5 without sodium. This indicates

that the difference between the values calculated with two-dimensional diffusion is due to the spatial self-shielding correction to the ^{238}U cross sections and the weighing with the fine structure of the fluxes.

The calculated coefficients shown in Table I.A.4 should be multiplied by 1.10, the ratio of calculated to measured normalization integral.* With this correction the calculated and measured values are within 20% of each other at the core center. The agreement in Sect. H is worse, however, indicating that the previous agreement with the FOP value was fortuitous.

4. ZPR-3 and ZPPR Operations and Analysis

a. Routine Operation of the Critical Facilities (P. I. Amundson and R. G. Matlock)

Last Reported: ANL-7618, pp. 10-11 (Sept 1969).

(i) ZPPR Operation. Operation of ZPPR has been entirely devoted to the FTR Program. Major activities included boron control-ring removal, neutron spectra, and reaction-rate traverse measurements.

(ii) ZPR-3 Operation. All materials used in Assembly 57 have been unloaded and placed in storage. The special aluminum matrix-tube bundles have been replaced with standard stainless steel tubes and the matrices have been aligned.

New back-mounting plates have been installed on the assembly. Installation of control-safety rod drives for Assemblies 58 and 59 (simple-composition Pu-C cores) has begun.

(iii) Computer Development. Modifications have been made to the data-system routines to type a "done" message to the Remote Teletype indicating extraneous interrupts received from the Multiplexor. There is no way to disregard the extraneous interrupt since one data word is taken for each interrupt and decoding of the extraneous data is already in progress before it is possible to determine if extra interrupts have occurred. When the "done" message is received, the operator may reinitialize the data-system routines and continue taking data.

A reactivity-traverse CRT display was added to the data systems allowing for live display of rod position versus count rate.

With the gradual expansion of data-acquisition techniques, utilization of an expanded monitor system is necessary. Efforts have been initiated to update all software source decks to the most recent monitor-system releases.

---

*Karam, R. A., Nucl. Sci. Eng. 37, 192 (1969).

An XY plotter program to plot the analyzed data from reactivity traverse runs has been written.

A program has been completed to read the incremental magnetic-tape data-acquisition system, convert the thermocouple readings to temperatures, and log the results.

b. Clean Critical Experiments (P. I. Amundson)

Last Reported: ANL-7618, pp. 11-15 (Sept 1969).

The essential purpose of the construction of ZPR-3 Assemblies 58 and 59 is to study the persistent error in the calculation of central reactivity worths. These assemblies will be constructed with a single-drawer core cell, which consists of two plutonium-aluminum plates and fourteen graphite plates, and thus these systems also form a natural continuation of the series of "benchmark" physics assemblies. The cell differs from the cell of Assembly 53 in that the mixed-fuel column has been replaced by a second plutonium column (and a graphite column). This gives a core with no U-238 present, and a lower critical mass and volume. The effect of moving the two fuel columns together may be studied.

The two assemblies will differ from each other in the reflector. One will be 12 in. of depleted uranium blocks; the other will be 12 in. of blocks of lead.

TABLE I.A.5. Composition of ZPR-3 Assemblies 58 and 59 (10^{24} atoms/cc)

Isotope	Core	Reflectors	
		Uranium	Lead
Pu-239	0.002138		
Pu-240	0.000102		
Pu-241	0.0000098		
Al	0.000222		
C	0.06030		
U-235		0.000084	
U-238		0.03998	
Fe	0.007429	0.004540	0.004540
Cr	0.001978	0.001209	0.001209
Ni	0.000809	0.000494	0.000494
Pb			0.02778

Preliminary values for the compositions of the core, as used in the design calculations, are given in Table I.A.5. The standard single-drawer core cell is: CCCC Pu CCCCCCC Pu CCC, where each plate is 0.125 in. thick and Pu represents a ZPR-3 Pu/Al plate. Cross sections in 24 groups were prepared from MC^2 using ENDF/B data. Because of the importance of the Doppler calculations to safety criteria for ZPR-3, the Pu-239 fission and capture cross sections in the energy region between 275 eV and 25 keV were obtained (at 300°K) from the IDIOT Code, and below 275 eV from the RABID Code. Recent values of the Pu-239 resonance parameters were used. Cross sections were also found for the cell with two fuel-plate columns moved together. The cross sections for the uranium reflector of Assembly 53 were used, and lead cross sections were adapted from the Bondarenko data.

Spherical MACH-1 calculations were run using both fuel-plate configurations and both reflectors. The critical radii for the uranium and lead reflectors with the plates separated were 30.4 and 28.3 cm, giving critical masses (Pu-239 + Pu-241) of 100.6 and 80.5 kg, respectively, both well below the permissible 430 kg plutonium. Moving the plates produced changes ≈0.1 kg in the critical masses. The central spectra for the four cases are compared in Table I.A.6. The only significant differences are in the last few groups where the reduced resonance self-shielding in the plates apart remove more of the low-energy neutrons. The central spectrum for Assembly 53, calculated with the standard ENDF/B Pu-239 data, is also shown. The adjoint for one case is given in the last column.

TABLE I.A.6. Normalized Central Spectra

Group	Lower Energy	Plates Together, U Reflector	Plates Apart, U Reflector	Plates Apart, Pb Reflector	Plates Together, Pb Reflector	Assembly 53	Adjoint,[a] Plates Apart, U Reflector
1	3.68 MeV	0.0294	0.0295	0.0288	0.0287	0.0254	6.664
2	2.31	0.0544	0.0547	0.0538	0.0536	0.0458	6.827
3	1.35	0.0888	0.0893	0.0888	0.0883	0.0732	6.896
4	821 keV	0.0964	0.0969	0.0970	0.0965	0.0824	7.165
5	498	0.0935	0.0940	0.0947	0.0942	0.0869	7.518
6	302	0.0852	0.0857	0.0866	0.0861	0.0849	7.842
7	183	0.0761	0.0765	0.0774	0.0770	0.0791	8.120
8	111	0.0669	0.0673	0.0681	0.0677	0.0712	8.376
9	67.4	0.0601	0.0604	0.0611	0.0608	0.0651	8.569
10	40.9	0.0541	0.0544	0.0549	0.0546	0.0593	8.753
11	24.8	0.0472	0.0475	0.0478	0.0475	0.0523	8.966
12	15.0	0.0425	0.0428	0.0428	0.0426	0.0478	9.124
13	9.12	0.0379	0.0380	0.0379	0.0377	0.0428	9.265
14	5.53	0.0318	0.0320	0.0317	0.0315	0.0363	9.386
15	3.35	0.0286	0.0287	0.0283	0.0282	0.0326	9.510
16	2.03	0.0249	0.0249	0.0244	0.0244	0.0279	9.747
17	961 eV	0.0294	0.0291	0.0284	0.0287	0.0335	10.153
18	454	0.0212	0.0206	0.0201	0.0207	0.0238	10.996
19	275	0.0097	0.0092	0.0090	0.0095	0.0106	11.616
20	61.4	0.0171	0.0150	0.0148	0.0169	0.0167	12.049
21	13.7	0.0040	0.0030	0.0030	0.0040	0.0022	11.594
22	3.06	0.0006	0.0004	0.0004	0.0007	0.0002	11.743
23	0.683	0.0002	0.0001	0.0001	0.0002	0	11.276
24	0.0028	0	0	0	0	0	14.489

[a]Unnormalized.

The basic configuration (fuel columns separated and a uranium reflector) was converted to a cylinder (L/D = 0.9; shape factor = 0.95) giving a half-height very close to 10 in. and a radius corresponding to a loading of 81 drawers in each half of the reactor matrix (106 kg Pu-239 + Pu-241). For the lead-reflected system, the critical loading will be about 65 drawers in each half (85 kg Pu-239 + Pu-241).

c. Doppler Experiments (R. E. Kaiser)

Last Reported: ANL-7618, p. 15 (Sept 1969).

The final tests and modifications of the Doppler mechanism have been completed. A small leak at an electrical connection in the vacuum manifold was repaired.

P-wave resonance effects for the analysis of the U-238 reactivity Doppler experiment in ZPR-3 Assembly 53 have been evaluated. P-wave resonances in the unresolved region contribute about 2% of the total reactivity change.

d. Mockup Critical Experiments (W. P. Keeney)

Last Reported: ANL-7618, p. 17 (Sept 1969).

The experiments with ZPPR Assembly 1 continued. This ZPPR assembly is the Assembly 2 of the FTR Resumed Phase-B Critical Experiments Program (FTR-2). With the completion of the ZPPR annual containment tests, the shield portion of FTR-2 experimental program was begun. Reported here are the results of the control-ring removal, the shield installation, and the fuel-storage experiment. The proton-recoil spectrum measurements were done in the shield and reflector, and the radial reaction-rate traverses of Pu-239, U-238, and B-10 have been measured with traverse counters at axial elevations of 3 and 22 in. These data are now being processed.

(i) Core Depletion, Control-ring Removal, and Shield Addition. The shield experiment required the removal of the B_4C control ring from the FTR-2 assembly. Replacement of the control ring with a radial reflector was performed in steps, with the resulting reactivity effects compensated by alternately substituting depleted uranium for the plutonium fuel in the central region of the core. Control-ring material was symmetrically removed from each of the assembly quadrants whenever possible. The step-wise substitutions performed in removing the control ring and establishing a critical configuration are summarized in Table I.A 7, Loadings 96 to 114. The reference for this experiment, Loading 1-96, is identical to the ZPPR FTR-2 Reference Critical Configuration (see Progress Report for July 1969, ANL-7595, p. 25). As the core depletion and control-ring removal proceeded, the subcriticality of resulting configurations was measured using the inverse-kinetics method, and the results are given in Table I.A.7. As shown, approximately 29 kg of fissile mass was removed from the core to compensate for the substitution of radial reflector for the control ring.

The subcriticality data presented in Table I.A.7 were evaluated using two sets of delayed-neutron fractions: those corresponding to the ZPPR FTR-2 Reference Critical Configuration (see Progress Report for July 1969, ANL-7595, p. 24) and those listed in Table I.A.8. The effect on the calculated k_{ex} values was insignificant.

TABLE I.A.7. ZPPR FTR-2 Core Depletion, Control-ring Removal, and Shield-addition Loading Summary[a]

Loading No.	Radial Reflector Composition Substituted for Control Composition, Matrix Position	No. of Control-ring Drawers Remaining (Halves 1 and 2)[a]	Depleted U Substituted for Pu Fuel Matrix Position	Total Fissile Mass in Halves 1 and 2 (kg)[b]	k_{ex} (% $\Delta k/k$)[c]
96	Reference	240	-	527.041	+0.086 ± 0.001
97	-	240	137-37	525.043	-0.480 ± 0.030
98	144-28 145-29 144-29	234	-	525.043	-
99	130-28 130-46 130-29 144-45 130-45 144-46 -(145-29)	224	-	525.043	-0.159 ± 0.005
100	-	224	136-37 137-36 137-38 138-37	519.050	-1.618
101	125-38 145-29 125-39 145-30 126-38 148-35 126-39 148-36 129-44 149-35 129-45 149-36	200	-	519.050	-
102	129-29 138-48 129-30 138-49 135-25 139-48 135-26 139-49 136-25 145-44 136-26 145-45	176	-	519.050	-0.800 ± 0.070
103	134-25 140-25 134-26 140-26 134-48 140-48 134-49 140-49	160	-	519.050	-
104	131-27 143-27 131-28 143-28 131-46 143-46 131-47 143-47	144	-	519.050	-0.226 ± 0.003
105	-	144	136-36 136-38 138-36 138-38	515-054	-1.36 ± 0.20
106	125-35 138-25 125-36 138-26 126-35 139-25 126-36 139-26 135-48 148-38 135-49 148-39 136-48 149-38 136-49 149-39	112	-	515.054	-0.607 ± 0.027
107	125-37 137-48 126-37 137-49 137-25 148-37 137-26 149-37	96	-	515.054	-0.120 ± 0.001
108	-	96	135-37 137-35 137-39 139-37	507.064	-1.69 ± 0.25
109	127-31 146-30 127-32 146-31 127-42 146-43 127-43 146-44 128-30 147-31 128-31 147-32 128-43 147-42 128-44 147-43	64	-	507.064	-0.849 ± 0.061
110	-	64	135-36 135-38 139-36 139-38	503.068	-1.60 ± 0.25
111	132-26 141-26 132-27 141-27 132-47 141-47 132-48 141-48 133-26 142-26 133-27 142-27 133-47 142-47 133-48 142-48	32	-	503.068	-0.301 ± 0.006

TABLE I.A.7 (Contd.)

Loading No.	Radial Reflector Composition Substituted for Control Composition, Matrix Position	No. of Control-ring Drawers Remaining (Halves 1 and 2)[a]	Depleted U Substituted for Pu Fuel, Matrix Position	Total Fissile Mass in Halves 1 and 2 (kg)[b]	k_{ex} (% $\Delta k/k$)[c]
112	-	32	136-35 136-39 138-35 138-39	495.077	-1.52 ± 0.18
113	126-33 147-33 126-34 147-34 126-40 147-40 126-41 147-41 127-33 148-33 127-34 148-34 127-40 147-40 127-41 148-41	0	-	495.077	-0.306 ± 0.007
114	-	0	-(135-36) -(135-38) -(139-36)	498.073	+0.167 ± 0.003
120	Sodium/Stainless steel shield installed. Reactor configuration identical to Loading 114	0		498.073	+0.215 ± 0.003
122	Sodium/Stainless steel shield installed. Reactor configuration identical to Loading 113	0	135-36 135-38 139-36	495.077	-0.260 ± 0.004

[a]Substitutions were made in mirror image positions in both Halves 1 and 2. Only the Half 1 positions are listed. Negative substitution listings indicate inverse substitution.

[b]Pu-239 + Pu-241 + U-235.

[c]For all subcritical cases all of the fueled safety and control rods were fully inserted in the core. For all the supercritical cases the excess reactivity is that which the reactor would contain had all rods been inserted. With the exception of Loading No. 100 all of the $-k_{ex}$ values were measured with the inverse-kinetics technique. A repeated failure in the computer data-acquisition system required this subcritical value to be determined from the calibration of the subcritical counters obtained from Loading No. 99.

TABLE I.A.8. Calculated Beta Fractions for the ZPPR FTR-2 Shield Configuration

Group	$\beta_i^{(U-235)}$	$\beta_i^{(U-238)}$	$\beta_i^{(Pu-239+Pu-241)}$	$\beta_i^{(Pu-240)}$	Group	$\beta_i^{(U-235)}$	$\beta_i^{(U-238)}$	$\beta_i^{(Pu-239+Pu-241)}$	$\beta_i^{(Pu-240)}$
1	1.91663-06	1.86568-05	5.84633-05	1.64766-06	4	2.05281-05	5.56835-04	5.04630-04	2.05958-05
2	1.07432-05	1.96614-04	4.30781-04	1.60647-05	5	6.45600-06	3.22907-04	1.58466-04	7.53218-06
3	9.48226-06	2.32493-04	3.32317-04	1.12983-05	6	1.31138-06	1.07636-04	5.38477-05	1.70651-06

Notes: β_{eff} = 3.08293-03; ℓ = 5.20426-07 sec; Ih/% ρ = 1.03853 + 03.

The effective source used for the detector in determining k_{ex} by the equation k_{ex} = S/(Equilibrium Count Rate) was determined by the use of a rod drop in the subcritical system. The power history was recorded before, during, and after the drop, until equilibrium power was again reached. The usual point kinetics equations were used to calculate k_{ex} for each time interval. The calculated values of the initial and final reactivity divided by the assumed source strength are independent of the assumed source. This same quotient soon after the rod drop is a function of the assumed source. The best value of the source was found by adjusting the source until the quotients after the drop were constant. The error in this source determination was found from the change in this source necessary to cause an initial deviation of the quotient after the drop from the constant value found above by an amount equal to the rms error in these values of the quotient.

With the removal of the control ring completed, the sodium-stainless steel shield was added to the assembly. The shield extended the length of the FTR-2 core and axial reflector, had a thickness of approximately 2 ft, and an azimuthal span of 80°, and contained 62.7-vol % stainless steel, 23.5-vol % sodium, and 13.8-vol % void. An interface view of the resulting assembly is shown in Fig. I.A.5 and is designated the ZPPR FTR-2

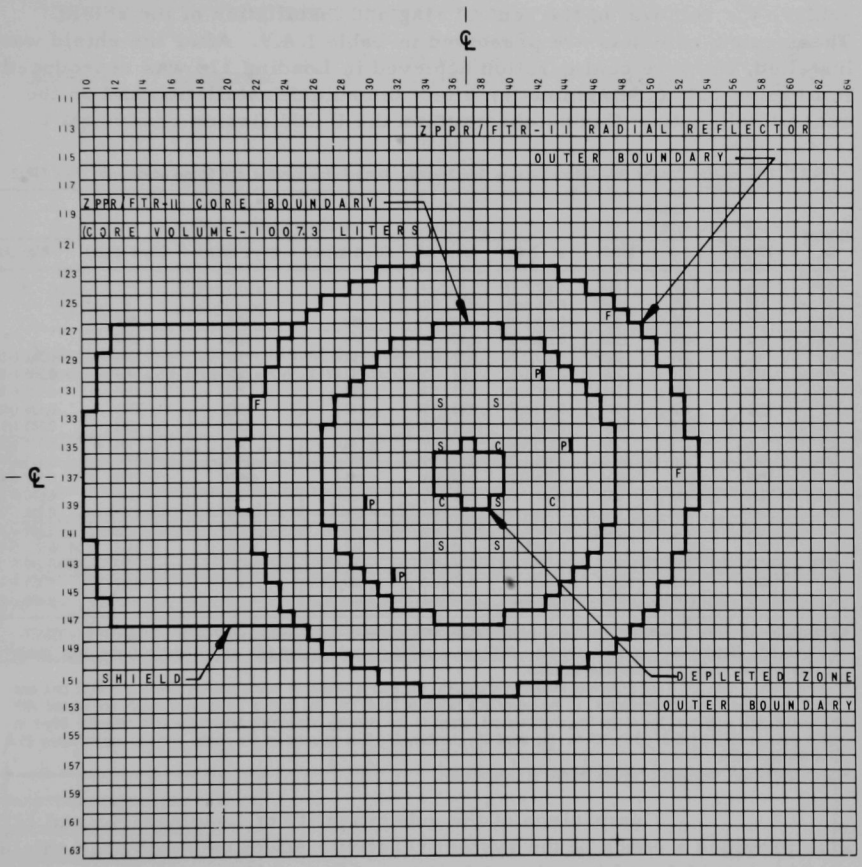

ZPPR HALF I

(HALF 2 IS A MIRROR IMAGE OF HALF 1)

S - SAFETY ROD C - CONTROL ROD P - DRAWER ADJACENT TO POISON SAFETY ROD

| - POISON SAFETY ROD (WITHDRAWN DURING OPERATION)

F - U-235 FISSION CHAMBER (FRONT OF CHAMBER AT REACTOR MIDPLANE. NO F's IN HALF 2)

Fig I.A.5. ZPPR FTR-2 Shield Configuration (Loading 1-120)

shield configuration (Loading 1-120). As indicated in Table I.A.7, Loadings 114 and 120, the installation of the shield caused a reactivity effect of +0.048% $\Delta k/k$.

Subcritical neutron flux data were monitored by the three U-235 fission chambers (see Progress Report for June 1969, ANL-7581, p. 26) and the operational chambers as the loading changes proceeded to achieve the removal of the control ring and installation of the shield. These count-rate data are presented in Table I.A.9. After the shield was installed, the core configuration achieved in Loading 113 was reproduced in Loading 122 to determine the effect the shield installation had on the subcritical neutron flux as observed on the U-235 fission chambers.

TABLE I.A.9. Neutron Counter Data Obtained during Core Depletion, Control-ring Removal, and Shield Addition for ZPPR FTR-2

Loading No.	Fission Chamber Data (c/sec)[a]			Operational Chamber Data[b]					
	132-22	126-47	137-52	Ch. 7 (A)	Ch. 8 (A)	BF_3-1 (c/sec)	BF_3-2 (c/sec)	BF_3-3 (c/sec)	Pico (A)
96[c]	960	1456	1647	0.122 (-8)	-	-	-	-	-
97	310	472	543	0.430 (-9)	0.54 (-9)	-	-	-	-
98	397	595	685	0.555 (-9)	0.68 (-9)	253	1796	2594	
99	894	1416	1520	0.115 (-8)	0.17 (-8)	556	3764	5364	
100	90.5	145	162	0.113 (-9)	0.17 (-9)	54.8	387	589	0.361 (-10)
101	118	217	219	0.161 (-9)	0.22 (-9)	72.9	501	769	0.566 (-10)
102	199	322	394	0.254 (-9)	0.31 (-9)	112	757	1169	0.912 (-10)
103	293	422	570	0.340 (-9)	0.43 (-9)	147	1031	1515	0.124 (-9)
104	845	1238	1600	0.950 (-9)	0.14 (-8)	402	2592	4003	0.343 (-9)
105	186	272	353	0.210 (-9)	0.27 (-9)	88.0	578	934	0.733 (-9)
106	367	516	800	0.405 (-9)	0.50 (-9)	166	1070	1751	0.157 (-9)
107	1898	2578	4907	0.196 (-8)	0.27 (-8)	844	5069	7774	0.807 (-9)
108	137	188	357	0.149 (-9)	0.20 (-9)	61.5	384	646	0.600 (-10)
109	287	469	713	0.323 (-9)	0.41 (-9)	126	779	1329	0.124 (-9)
110	154	252	384	0.171 (-9)	0.15 (-9)	68.8	418	732	0.669 (-10)
111	1021	1407	2331	0.980 (-9)	0.14 (-8)	367	2118	3678	0.392 (-9)
112	192	261	437	0.185 (-9)	0.21 (-9)	69.6	404	727	0.739 (-10)
113	1007	1503	2278	0.100 (-8)	0.15 (-8)	380	2127	3827	0.389 (-9)
122	2745	1789	2693	0.117 (-8)	0.175 (-8)	406	-	-	0.458 (-9)

[a]U-235 fission chambers manufactured by Westinghouse. Model 6376 located in matrix positions 132-22 (r = 87.68 cm) and 126-47 (r = 84.14 cm). Model 6376A located in 137-52 (r = 82.79 cm). Front of chambers aligned with reactor axial midplane. Data monitored for time intervals yielding ≤1% counting statistics.

[b]The Pico, Ch. 7, and Ch. 8 are B-10-lined ionization chambers. The Pico is located in matrix position 136-55 (r = 99.52 cm), and Chs. 7 and 8 and located at the corners of the halves at a radius of 161.49 cm. The front of all three chambers are aligned with the reactor axial midplane. Two of the BF_3 chambers are located in the assembly immediately behind the axial reflector: BF_3-2 in matrix position 137-37 and BF_3-3 in 148-48. The third BF_3 chamber, BF_3-1, is mounted on the reactor cell wall approximately 25 ft from the core center.

[c]k_{ex} = -0.143% $\Delta k/k$ (achieved by partial removal of control rods).

Comparison of the subcriticality of Loadings 113 and 122 also provides a check of the system reactivity effect caused by the shield as determined from the critical Loadings 114 and 120. The two determinations compare within 0.002% $\Delta k/k$, which is within the accuracies of the subcritical measurements corresponding to Loadings 113 and 122.

The as-built compositions for the core, axial reflector, radial reflector, and safety and control drawers of the ZPPR FTR-2 shield configuration (Loading 1-120) are identical to those of the ZPPR FTR-2 Reference Critical Configuration. The composition of the shield and depleted

core drawers are given in Table I.A.10. Figure I.A.6 illustrates the plate arrangement in the shield drawers. The drawer loadings in the depleted core zone are identical to the normal core drawers except that depleted uranium replaces the plutonium fuel.

TABLE I.A.10. As-built Composition of Shield and Depleted Core Zones for the ZPPR FTR-2 Shield Configuration (atoms/b-cm)

Nuclide	Shield Zone	Depleted Core Zone	
		Drawer with One[a] 1/4-in.-column U-238	Drawer with Two[b] 1/4-in.-columns U-238
U-238		0.0078084	0.0108669
U-235		0.0000164	0.0000223
O		0.0150075	0.0154338
Na	0.0059617	0.0107196	0.0063408
C	0.0000264	0.0021888	
Fe	0.0371696	0.0078562	0.0143938
Ni	0.0045539	0.0010273	0.0008931
Cr	0.0102972	0.0022623	0.0019930
Mn	0.0005741	0.0001829	0.0001635
Mo	0.0000269	0.0000161	0.0000154

[a]Located in even-numbered matrix columns.
[b]Located in odd-numbered matrix columns.

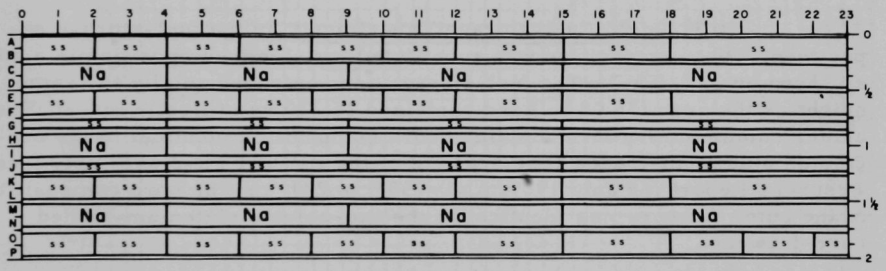

(a) Front Drawer

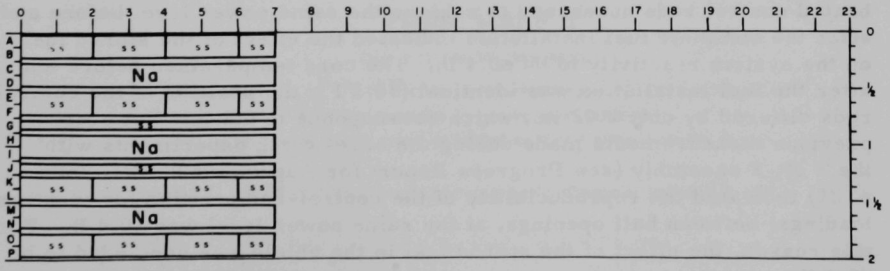

(b) Back Drawer

Fig. I.A.6. Shield Drawers for ZPPR FTR-2 Shield Configuration

(ii) Calibrations of Control and Safety Rods. Following the installation of the shield in the FTR-2 assembly, the control and safety rods, positioned as shown in Fig. I.A.5, were recalibrated using the inverse kinetics technique. First the neutron source constant of the system was determined from analysis of the power history resulting from both positive and negative reactivity changes due to control-rod motion. Then, from a stabilized power level of approximately 50 W, each rod being calibrated was individually driven from its most reactive position to its least reactive position and the neutron flux history recorded. By use of the measured source constant and the delayed-neutron fractions given in Table I.A.8, the rod worths were determined from analysis of the flux history. This method indicated the total worth of the 20 safety rods and of the 6 control rods as 2.8% $\Delta k/k$ and 0.6% $\Delta k/k$, respectively.

The reference loading for the ZPPR FTR-2 shield configuration (Loading 1-120) contained a fissile mass (Pu-239 + Pu-241 + U-235) of 498.073 kg. This loading included the fissile material contained in the fueled safety and control rods; however, two control rods (139-43 and 239-43) were completely withdrawn from the core and another (235-39) withdrawn 5.748 in. Complete insertion of all the control rods would have yielded an excess reactivity of +0.215% $\Delta k/k$.

(iii) Shield Fuel-storage Experiment. In the fuel-storage experiment, core composition was substituted for shield composition in a zone as shown in Fig. I.A.7. The fuel-storage zone extended axially the same height as the core (36.08 in.) and contained 25.320 kg of fissile mass. The center column of drawers contained core composition identical to the one-column plutonium-loaded core drawers of the ZPPR FTR-2 assembly (see Progress Report for July 1969, ANL-7595, p. 24), and the core composition of the outer drawers was identical to the two-column plutonium-loaded core drawers.

The fuel-storage zone was achieved in three substitution steps as shown in Table I.A.11. Comparison of the positions of the calibrated control rods necessary to achieve the same power level before and after the complete fuel installation indicated the effect of the stored fuel on the system reactivity to be $\leq$0.4 Ih. The core temperature before and after the fuel installation was identical (70.3°F); the position of the control rods differed by only 0.02 in., which corresponds to 0.1 Ih. However, previous measurements made during the edge-worth experiments with the FTR-2 assembly (see Progress Report for August 1969, ANL-7606, p. 26) indicated the reproducibility of the control-rod position for identical loadings, between half openings, at the same power level was $\pm$0.4 Ih. For this reason, the effect of the stored fuel in the shield was concluded to be $\leq$0.4 Ih.

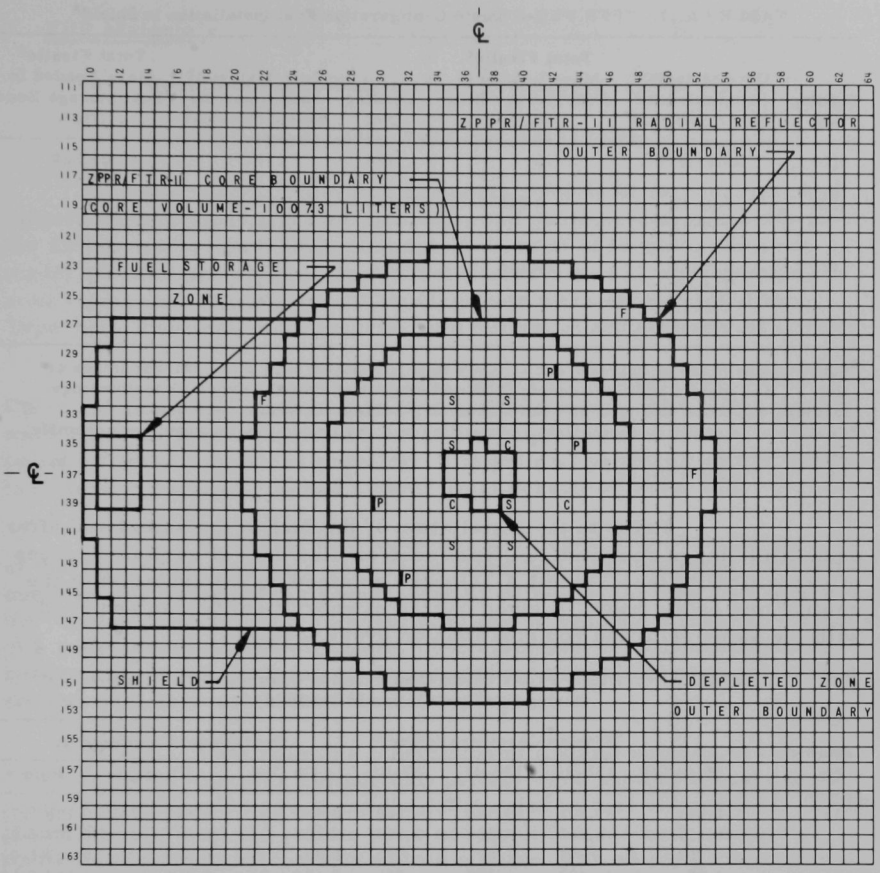

ZPPR HALF I

(HALF 2 IS A MIRROR IMAGE OF HALF 1)

S - SAFETY ROD C - CONTROL ROD P - DRAWER ADJACENT TO POISON SAFETY ROD

▌- POISON SAFETY ROD (WITHDRAWN DURING OPERATION)

F - U-235 FISSION CHAMBER (FRONT OF CHAMBER AT REACTOR MIDPLANE. NO F's IN HALF 2)

Fig. I.A.7. ZPPR FTR-2 Shield with Fuel-storage Configuration (Loading 1-130)

TABLE I.A.11. ZPPR FTR-2 Shield Configuration Fuel Installation in Shield[a]

Loading No.	Core Material[b] Substituted for Shield Material	Total Fissile[c] Mass Loaded in Fuel Storage Zone (kg)	Loading No.	Core Material[b] Substituted for Shield Material	Total Fissile[c] Mass Loaded in Fuel Storage Zone (kg)
127	Reference	0	130	137-11	25.320
				137-12	
128	135-13	4.046		137-13	
	136-13			138-11	
				138-12	
129	135-11	10.128		138-13	
	135-12			139-11	
	136-11			139-12	
	136-12			139-13	

[a]Substitutions made in Halves 1 and 2. Only Half 1 is listed; Half 2 is a mirror image of Half 1. The matrix positions ending in an odd number contain 2-column plutonium core loadings and those ending in an even number a 1-column plutonium core loading.
[b]Fuel-storage zone replaced shield composition in a region ±18.036 in. about the assembly axial midplane.
[c]Pu-239 + Pu-241 + U-235.

Prior to the installation of the fuel in the shield and after each of the three substitution steps, neutron-flux data at various degrees of subcriticality (see Table I.A.12) were obtained by manipulation of the control and safety rods. A given degree of subcriticality was achieved with the same rods and rod positions on every loading.

TABLE I.A.12. ZPPR FTR-2 Shield Configuration Chamber Data Obtained during Fuel Installation in Shield[a]

Loading No.	k_{ex} (% Δk/k)	Fission Chambers (c/sec)[b]			Operational Chambers (A)		
		132-22	126-47	137-52	Ch. 7	Ch. 8	Pico
127	-0.007	89,871	69,988	64,108	0.430 (-7)	0.572 (-7)	0.168 (-7)
	-0.110	6,262	4,286	6,187	0.268 (-8)	0.367 (-8)	0.108 (-8)
	-0.702	991	671	976	0.452 (-9)	0.570 (-9)	0.169 (-9)
	-1.68	433	289	426	0.194 (-9)	0.260 (-9)	0.753 (-10)
	-3.23	227	141	217	0.980 (-10)	0.150 (-9)	0.389 (-10)
128	-0.110	6,279	4,285	6,176	0.265 (-8)	0.360 (-8)	0.108 (-8)
129	-0.110	6,239	4,242	6,177	0.270 (-8)	0.360 (-8)	0.109 (-8)
130	-0.007	90,091	70,434	65,359	0.430 (-7)	0.573 (-7)	0.171 (-7)
	-0.110	6,184	4,242	6,168	0.267 (-8)	0.367 (-8)	0.109 (-8)
	-0.702	984	661	971	0.449 (-9)	0.570 (-9)	0.170 (-9)
	-1.68	436	287	423	0.196 (-9)	0.263 (-9)	0.747 (-10)
	-3.23	230	140	217	0.970 (-10)	0.153 (-9)	0.386 (-10)

[a]Various degrees of subcriticality for each loading achieved by manipulation of the control and safety rods. A given degree of subcriticality was achieved with identical control- and/or safety-rod positions for every loading.
[b]Counting statistics ≤0.4%.

5. ZPR Materials

a. Development of Fabrication Techniques (J. E. Ayer)

Last Reported: ANL-7527, pp. 33-34 (Dec 1968).

(i) ZPPR Oxide Rod Elements. Pilot-lot development and manufacture of oxide rod fuel elements, and gamma-scan standards for the ZPPR reactor have been completed. A total of 52 elements were made; 30 were prototype oxide rod fuel elements and 22 were gamma-scan elements. All UO_2 and $(U,Pu)O_2$ pellets were encapsulated in Type 304L stainless steel jackets, with helium at atmospheric pressure.

The UO_2 and $(U,Pu)O_2$ pellets were fabricated by the Dow Chemical Company, Rocky Flats Division, and sent to ANL. The pellets were made by a cold press and sinter technique that produced acceptable pellets without centerless grinding. The pellets, produced with a length-to-diameter ratio of 1.5, had a theoretical density of about 95%.

A loading technique was developed to protect the outside of the jacket tube and weld zone from plutonium contamination. A special end plug was designed to prevent thinning of the jacket tube wall or increase the outside diameter in the welded area and to produce a finished element of a predetermined overall length. The elements were dimensionally checked, X-rayed, leak detected, and surveyed for alpha contamination on the external surfaces before final acceptance.

Data from the fabrication of a small number of UO_2 and $(U,Pu)O_2$ (right-circular cylindrical) pellets were used as a basis for a product specification governing the fabrication of fuel elements for ZPPR. Exact diameters of the pellets were not specified; instead, weights of material that could be introduced into a jacket with an inside diameter of 0.350 in. and a nominal length of 5.7 in. were fixed. This effectively required the diameters to be between 0.340 and 0.345 in., with a theoretical density of at least 92%. The objective of this requirement was to permit sufficient latitude for fired dimensions and densities to preclude centerless grinding.

In addition to writing a product specification and obtaining statistical information, loading studies were conducted with part of the pellets produced. The loading studies were required to prove adequacy of design and to identify and solve any major problems associated with pilot-lot production of prototypic elements. At least two problems associated with fuel-element assembly were anticipated. The first was the control of plutonium contamination on the outside of the fuel-element jacket, particularly in the area of the weld. The second was maintaining minimum diametral tolerances between fuel and jacket and between jacket and the

calandrias that will contain the fuel elements during the reactor physics experiments. Minimum gap between jacket and plutonium-bearing fuel aggravates the contamination problem and loading difficulties; limited gap between clad and calandria means that weld-bead protrusion must be kept at a minimum.

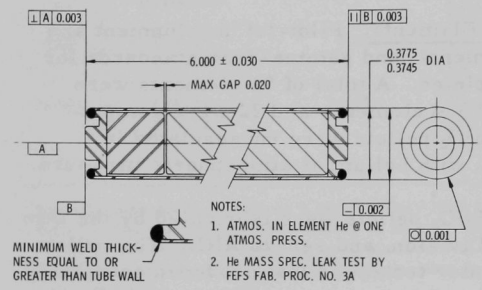

Fig. I.A.8. ZPPR Oxide Rod Element

(a) Design of the Fuel Element. Figure I.A.8 is an assembly drawing of the ZPPR oxide rod element delineating the geometric characteristics of the element. Of prime importance is the straightness tolerance designated as 0.002 in. This dimension limits the rod straightness and weld buildup to a total of 0.002 in., assuring adequate clearance between the element and the calandria tubes. The 0.020-in. maximum gap between fuel and end cap is maintained by interposing a spacer of Type 304 stainless steel between the fuel column and end cap. The length of the spacer is determined for each individual element. The fuel-element length tolerance of ±0.030 in. results from the algebraic accumulation of tolerances on the fuel tube and the two end plugs, which are ±0.005 and ±0.010 in., respectively. The design of the end plugs is predicated upon (1) controlled length of element, (2) provision of a bearing surface, apart from the weld bead, between elements, and (3) attainment of a girth weld with penetration at least equal to the tubing wall thickness with minimum protrusion beyond the element outside diameter.

Figure I.A.9 depicts the fuel pin. The fuel for loading studies was produced by the Dow Chemical Company, Rocky Flats Division, as output from a program the purpose of which was to evaluate manufacturing processes for UO_2 and $(U,Pu)O_2$ fuel-rod elements.

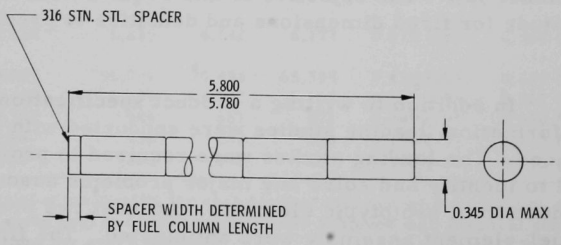

Fig. I.A.9. Fuel Pin of a ZPPR Oxide Rod Element

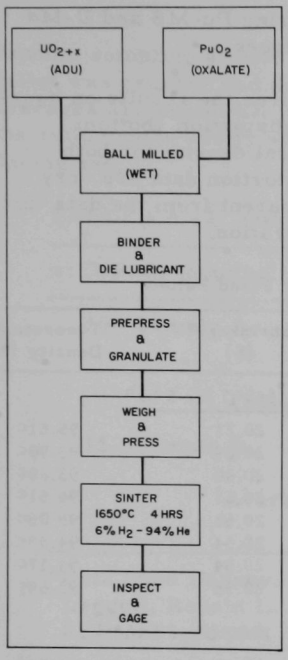

Fig. I.A.10

Schematic** of Fabrication Used for Mixed Oxides

(b) Pellet Manufacture*

(1) Experimental Procedure. Two compositions of $(U,Pu)O_2$ and five blends of UO_2 were made by mechanical mixing, and fabricated according to the schematic in Fig. I.A.10. Hyperstoichiometric UO_2 was obtained from Nuclear Fuel Services through ANL. Plutonium dioxide was made at Rocky Flats by calcining oxalate (Pu IV) at 650°C. Because of the large PuO_2 agglomerate size it was ball milled in water for 24 hr in a rubber-lined mill. An equal weight of UO_2 powder was then added and milled for 4 hr. Additional UO_2 was added to adjust to the required composition and milled for another 4 hr. After removal of the water, 1 wt % carbowax 4000 and 1 wt % stearic acid were added in a CCl_4 solution. After evaporation of the CCl_4, the mixtures were isostatically pressed at 10,000 psi and granulated through a 14-mesh screen. Powder for pellets of each composition was weighed to ±0.05 g and pressed at various pressures to establish shrinkage characteristics of the blends. The same press and dies were used for $(U,Pu)O_2$ as for UO_2. The 15 and 30 mole % pellets were pressed at 20,000 and 18,250 psi, respectively. A length-to-diameter ratio of 1.5 was used. Sintering was accomplished in a small, graphite resistance furnace fitted with a nonporous alumina muffle tube to protect the pellets from the carbon atmosphere. Ten-mesh alumina grain was used for bedding the pellets. Nominal sintering parameters were 1650°C for 5 hr in a dry 94% He-6% H_2 atmosphere. A 16-hr sintering schedule was used. As with the UO_2 the sintering rate had to be held to less than 100°C/hr above 1200°C in order to maintain good dimensional control.

The sintered pellets were visually inspected for defects and measured at the top, waist, and bottom diameters with a blade micrometer. Five pellets from each sintering run were randomly selected for density determinations. Densities were obtained using monobromobenzene as the immersion liquid. Plutonium concentrations were determined by a calorimetric method. Oxygen-to-metal ratios were determined by a standard oxidation-reduction cycle. Homogeneity was examined

*For additional details see Harvey, Malcolm R., Teter, Alton R., and Leggett, Ronald L., Fabrication of Oxide Nuclear Fuel Pellets, RFP-1255 (March 21, 1969), pp. 23-28.

**Ibid, p. 24.

with the use of an electron microanalyzer monitoring Pu-Mβ and U-Mα X-ray lines and standard X-ray diffraction techniques.

(2) Results. Table I.A.13 gives the results on hourglassing (maximum diameter--waist diameter), distortion (bottom diameter--top diameter), shrinkage, and theoretical density for both $(U,Pu)O_2$ compositions. The hourglassing and distortion data are very similar to those obtained with pure UO_2. It is apparent from the data that the densities are not affected by the PuO_2 concentration.

TABLE I.A.13. Physical Characteristics of Fired Pellets

Run No.	Hourglassing[a] (in.)	Distortion[a] (in.)	Shrinkage[a] (%)	Theoretical Density (%)
	Data from 296 $(U_{0.70}Pu_{0.30})O_2$ Pellets Fired at 1660°C for 5 hr[b]			
5/17/68	0.0026	0.0007	20.21	95.51[c]
5/20/68	0.0053	0.0010	20.29	93.90[c]
5/21/68	0.0038	0.0009	20.40	93.68[c]
5/22/68	0.0030	0.0007	20.61	94.51[c]
5/23/68	0.0031	0.0007	20.64	95.06[c]
5/24/68	0.0030	0.0006	20.54	94.59[c]
5/25/68	0.0023	0.0005	20.54	94.17[c]
5/27/68	0.0023	0.0007	20.56	93.69[c]
	Data from 260 $(U_{0.85}Pu_{0.15})O_2$ Pellets Fired at 1660°C for 5 hr			
4/23/68	0.0010	0.0004	20.50	94.04[d]
5/6/68	0.0032	0.0007	20.61	95.11[d]
5/7/68	0.0037	0.0006	20.60	94.86[d]
5/8/68	0.0056	0.0006	20.50	95.41[d]
5/9/68	0.0046	0.0007	20.67	96.11[d]
5/10/68	0.0036	0.0008	20.75	95.84[d]
5/14/68	0.0021	0.0007	20.45	94.42[d]
5/15/68	0.0025	0.0007	20.77	95.64[d]
	Data from 240 $(U_{0.85}Pu_{0.15})O_2$ Pellets Fired at 1650°C for 4 hr			
6/17/68	0.0049	0.0006	20.60	95.22[e]
6/18/68	0.0031	0.0006	20.60	95.00[e]
6/19/68	0.0024	0.0004	20.70	94.81[e]
6/20/68	0.0058	0.0005	21.06	95.60[e]
6/21/68	0.0052	0.0007	21.12	95.81[e]
6/22/68	0.0035	0.0008	21.30	95.69[e]

[a]Averaged from all pellets in run.

[b]Data from Harvey, Malcolm R., Teter, Alton R., and Leggett, Ronald L., Fabrication of Oxide Nuclear Fuel Pellets, RFP-1255 (March 21, 1969), p. 26.

[c]Average of 5 pellets randomly selected from each run. Overall average was 94.36%. Standard deviation was 1.00%.

[d]Average of 5 pellets randomly selected from each run. Overall average was 95.31%. Standard deviation was 0.81%.

[e]Average of 5 pellets randomly selected from each run. Overall average was 95.34%. Standard deviation was 0.55%.

Oxygen-to-metal ratios were determined for a random sampling of both compositions and are listed in Table I.A.14. Each pellet was crushed and divided into two or three parts, and sampled. The averages are somewhat lower than were expected from the literature, but the ratio can be easily adjusted by controlling the water vapor in the reducing gas.

TABLE I.A.14. Oxygen-to-Metal (O/M) Ratios of Mixed Oxides[a]

wt % PuO_2 (nominal)	O/M	wt % PuO_2 (nominal)	O/M
15--Sample A	1.965	30--Sample C	1.943
	1.950		1.943
	1.965		1.942
Average	1.959	Average	1.943
15--Sample B	1.921	30--Sample D	1.960
	1.967		1.950
Average	1.944		1.945
		Average	1.952

[a]Data from Harvey, Malcolm R., Teter, Alton R., and Leggett, Ronald L., Fabrication of Oxide Nuclear Fuel Pellets, RFP-1255 (March 21, 1969), p. 26.

Random, continuous electron-microprobe scans of 600 μm were run on both compositions to determine inhomogeneity. The scanning rate was 10 μm/min with a beam size of approximately 1 μm. No variations in uranium or plutonium were seen. X-ray diffraction indicated a high degree of solid solution.

(c) Characterization of Fuel Materials. The fuel pellets received from Dow Chemical Company were subjected to check analyses by ANL. Check of chemical analyses consisted of major element, minor element, and isotopic content. Each pellet was examined visually for cracks, excessive edge chipping, and hourglassing. Pellets that appeared acceptable on the basis of visual examination were weighed, passed through a 0.349-in.-dia drop-through gauge, and checked for length. These pellets became the population from which fuel columns were assembled. Choice of pellets for a particular column was based upon establishing a limited range of weight-to-length ratios. Each column was identified by assigning it to a specific tube number before loading.

The weight-to-length ratios and standard deviations obtained for 12 columns each of oxide pellets containing 13 wt % Pu, 26 wt % Pu, and depleted UO_2 were 15.69 ± 0.08, 15.90 ± 0.07, and 14.92 ± 0.06 g/in., respectively. A tabulation of column lengths and weights, column weight-to-length ratio, and element weight for both prototypic elements and [illegible] standards is shown in Tables I.A.15 and I.A.16.

TABLE I.A.15. Prototype ZPPR Oxide Rod Fuel Elements Produced

Rod Designation	Pellet Column Length (in.)	Total Pellet Weight (g)	Weight/Length (g/in.)	Element Weight (g)	ANL Batch No.
		13 wt % Pu			
F2	5.726	89.98	15.71	102.31	8-8-1989
F4	5.707	89.68	15.71	102.10	8-8-1989
F6	5.695	89.80	15.77	102.16	8-8-1989
F7	5.702	90.22	15.82	102.59	8-8-1989
F8	5.695	89.73	15.76	102.21	8-8-1989
F9	5.703	88.89	15.58	101.18	8-8-1990
F11	5.705	89.00	15.60	101.20	8-8-1990
F15	5.710	89.15	15.61	101.45	8-8-1990
F18	5.712	89.84	15.73	102.28	8-8-1989
F19	5.706	89.80	15.74	102.19	8-8-1989
F20	5.726	89.41	15.61	101.63	8-8-1990
F22	5.745	89.66	15.61	101.79	8-8-1990
		26 wt % Pu			
G12	5.676	89.89	15.85	102.07	8-8-1987
G24	5.670	89.83	15.84	101.89	8-8-1987
G27	5.679	89.77	15.80	102.01	8-8-1987
G29	5.670	90.19	15.89	102.55	8-8-1987
G31	5.676	90.19	15.89	102.61	8-8-1988 8-8-1987
G33	5.708	91.10	15.96	103.48	8-8-1987
G34	5.715	91.36	15.98	103.68	8-8-1987
G35	5.698	91.36	16.03	103.88	8-8-1987
G36	5.680	90.11	15.86	102.43	8-8-1987
G39	5.672	89.83	15.83	102.09	8-8-1987
G43	5.671	90.89	16.02	103.42	8-8-1987
G44	5.677	90.00	15.85	102.12	8-8-1987 8-8-1988
		Depleted Uranium Dioxide			
D51	5.755	86.25	14.89	98.69	6-6-686
D53	5.755	86.22	14.98	98.23	6-6-686
D54	5.755	86.26	14.98	98.47	6-6-686
D55	5.745	85.30	14.84	97.67	6-6-686
D56	5.755	85.97	14.93	98.21	6-6-686
D57	5.755	86.27	14.99	98.60	6-6-686
D60	5.755	86.24	14.98	98.50	6-6-686
D62	5.746	85.23	14.83	97.51	6-6-686
D67	5.755	85.82	14.91	98.14	6-6-686
D68	5.755	86.17	14.97	98.19	6-6-686
D70	5.747	85.34	14.85	97.72	6-6-686
D71	5.746	85.29	14.84	97.28	6-6-686

TABLE I.A.16. ZPPR Oxide Rod Gamma Standards

Rod Designation	Nominal Composition (wt %)	Pellet Column Length (in.)	Total Pellet Weight (g)	Weight/Length (g/in.)	Element Weight (g)	ANL Batch No.
101	10-Pu	5.736	89.51	15.60	101.84	8-8-2124
102	16-Pu	5.736	88.13	15.86	100.47	8-8-2128
104	16-Pu	5.737	87.22	15.20	99.33	8-8-2128
87	21-Pu	5.723	89.71	15.67	101.89	8-8-2143
88	21-Pu	5.712	89.72	15.70	101.96	8-8-2143
89	28-Pu	5.643	89.72	15.90	102.51	8-8-2151
90	28-Pu	5.646	89.75	15.89	102.45	8-8-2151
77	6-^{235}U	5.689	88.14	15.49	100.79	36-2-482
92	7-^{235}U	5.738	84.08	14.65	96.37	8-8-2138
93	7-^{235}U	5.747	84.17	14.64	96.08	8-8-2138
94	14-^{235}U	5.738	82.49	14.37	94.99	8-8-2139
95	14-^{235}U	5.738	82.87	14.39	95.09	8-8-2139
96	21-^{235}U	5.739	84.81	14.77	97.18	8-8-2140
98	21-^{235}U	5.739	84.67	14.73	97.17	8-8-2140
99	37-^{235}U	5.738	85.33	14.87	97.79	8-8-2141
100	37-^{235}U	5.738	85.41	14.88	97.99	8-8-2141

(d) Hardware Assembly and Inspection

(1) Forming. The Type 304L stainless steel hardware, consisting of two end plugs and a tube, was machined. One end of the tube was expanded over a mandrel to accommodate a loading funnel that had the same inside diameter as the jacket tubing. Each tube was identified, the end plugs and tube were washed in acetone, rinsed in ethyl alcohol, and dried in a furnace at 100°C for 1 hr before transfer to welding.

(2) Welding. The unexpanded end of the jacket tube was clamped in a split copper chill, an end cap was inserted, and the assembly placed in a lathe collet held in a vertical position. A second copper chill was placed in the recess of the end plug. This combination of chills was required to hold the weld bead in an upright position until solidification occurred, producing full tube wall thickness at the junction of the end plug and jacket tube. No increase in the outside diameter of the jacket tube in the weld area was permitted. Therefore, after welding, the jacket tubes were inspected for ovality, straightness, and weld-bead protrusion by insertion into a 0.380-in.-ID drop-through gauge to the expanded portion. Figure I.A.11 is a photomicrograph of a typical weld made against the tube and end plug design shown in Fig. I.A.8.

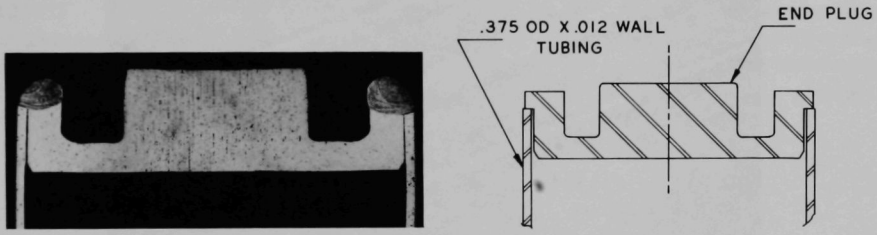

Finished Weld ~10X Before Welding

Fig. I.A.11. ZPPR Oxide Rod. Weld configuration in Type 304 stainless steel.

The bottom end cap weld was tested for integrity by means of helium mass spectrometer leak detection. An assembly showing a leak indication above background was rejected.

(e) Fuel-element Loading, Assembly, and Inspection. To prevent contamination in the final weld closure, a special loading funnel was inserted in the expanded portion of the jacket tube, the small lip on the funnel extending into the inside diameter of the jacket tube. Plastic tubing was shrunken over this assembly, trimmed to length, and secured to a loading pouch by means of compressive hose clamps. The assembled loading pouch was attached to a gloveport in the loading box. A column of pellets, previously weighed and measured for length and diameter, were loaded into each jacket. Each pellet was bottomed into the jacket with a push rod. After the last pellet was inserted the loading pouch was sealed and cut free with the

The loaded element was then transferred to an annex box of the welding hood where the loading pouch was removed from the element, and the exposed end of the loading funnel was cleaned of loose contamination with paper wipes and cotton swabs moistened with ethyl alcohol. The shrinkable tubing and loading funnel were removed, and the inside of the fuel jacket was checked for contamination and cleaned if necessary. A micrometer reading was taken from the end of the jacket tube to the top of the first pellet to determine the length of the spacer required to give the 0.000- to 0.010-in. end cap-to-spacer clearance. A spacer of the proper thickness was cut, inserted, and checked again with a micrometer before insertion of the end plug. The expanded end of the jacket tube was reduced to its original diameter with a special collet arrangement. The top edge of the jacket was then checked for loose contamination before the insertion of the end plug. The final end plug was tapped into position before transferring the assembly to the welding hood. The final end closure was made with the same welding procedure outlined previously. Exploded and cutaway views of a ZPPR oxide rod element are shown in Fig. I.A.12.

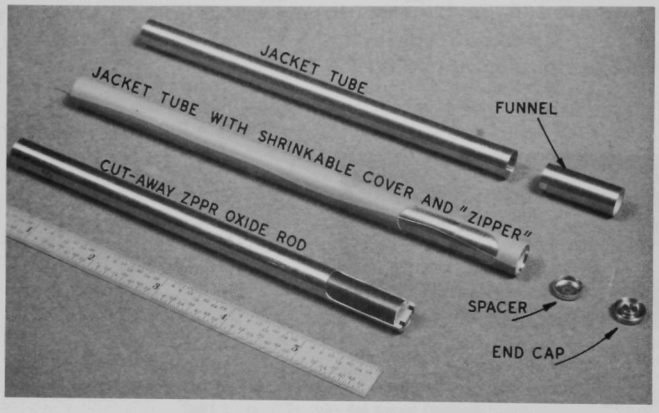

Fig. I.A.12. Exploded and Cutaway Views of ZPPR Oxide Rod Elements

The completed fuel-element assembly was checked for loose and fixed contamination before checking for leaks with a helium mass spectrometer. Acceptable contamination levels were <400 dpm fixed and <10 dpm loose alpha counts. The final end closure was made in an atmosphere that contained helium. The elements were placed one at a time in a fixture that reduced the pressure and used the entrapped helium as the leak indicator. As in the case of leak detection of the bottom end plug, any leak indication above background was cause for rejection. All elements were radiographed to check the welds, and the positions of the fuel and end spacers.

Tables I.A.15 and I.A.16 are a record of the 52 completed elements fabricated for reactor physics experiments and gamma-scan standards for evaluating ZPPR oxide rods produced by a commercial vendor.

B. Component Development--LMFBR*

1. Instrumentation and Control

a. Instrumentation Development for Instrumented Subassembly

(i) Instrumented-Subassembly Flowmeters (G. A. Forster)

Last Reported: ANL-7618, p. 18 (Sept 1969).

(a) Procurement of Mark-III (Sodium-calibratable) Flowmeters. Contract negotiations are proceeding for four flowmeters to be used in the instrumented-subassembly tests in EBR-II. Because delivery would not be in time for the instrumented subassemblies of the immediate future, the Laboratory is preparing to fabricate at least one Mark-III flowmeter.

(b) Modification of Calibration Loop for Mark-III Flowmeters. Modification work is about 80% complete. Thermocouples have been installed and connected to recording or indicating instruments. The depth probes in the flow tank are being replaced with units suitable for 1200°F. Their insulators will be supplied with extra heat to prevent sodium condensation, which shorted previous probes. The first heatup and flowtest is expected to be achieved in late November. A test section being fabricated to accommodate a Mark-III flowmeter will replace a straight piece of pipe in the existing loop.

b. FFTF Instrumentation

(i) In-Core Flowmeter (T. P. Mulcahey)

(a) Tests of Model Probe-type Eddy-current Flowsensors (J. Brewer)

Last Reported: ANL-7606, pp. 33-38 (Aug 1969).

Stability and sensitivity tests are being run in the CAMEL loop; maximum temperature and sodium flow velocity so far are 950°F and 6.5 ft/sec. As was observed with the drop tests in sodium, there is a sensitivity gap between 600 and 800°F; sensitivity decreased 40-50% above 700°F.

Impedance versus temperature tests have been run at 80-1400°F in a furnace on a single coil section whose coil was similar to each of the four coils on Probe No. 4. From ~650 to 670°F there is a 40% decrease in inductance because of the Curie temperature of the nickel

*Sodium Technology Development is reported in Sect. I.C.

cladding on the wire. A duplicate test made with a fiberglass-covered copper-wire coil section showed no change in inductance, which proved that the Inconel coil form and the Type 304 stainless steel sheath contributed nothing to the anomaly. The fact that $e \propto L\, d\phi/dt$ (where e is induced voltage, L is coil inductance, and $d\phi/dt$ is change in flux with time) explains the sensitivity gap. The nickel-clad wire exhibited small irregularities of inductance below 650°F, which probably was due to the magnetic character of the nickel cladding.

In the Curie-temperature region of a balanced coil system, a small temperature gradient can cause a large unbalanced signal. Obviously, another type of wire must be sought if the flowsensor is to operate below 700°F.

Molybdenum wire was considered for this use, but it has 3.3 times the resistance of copper at 20°C and has a high temperature coefficient of resistivity, which would lead to more power dissipation in the coils and probably poor stability. Also, molybdenum has a highly undesirable oxidation rate. Gold wire is being considered.

(b) Tests of Model Probe-type Permanent-magnet Flowsensors (F. Verber)

Last Reported: ANL-7595, pp. 29-32 (July 1969).

Major effort has been placed on the Type-A flowsensor referred to in ANL-7595. Three additional 1-in.-OD solid-configuration flowsensors have been fabricated and tested in the modified annular linear-induction sodium pump loop. The test results show that, for the magnet widths tested, the sensitivity of the flowsensor (mV per ft/sec) increases as the width W of the magnet increases.

In the following description of the Type-A flowsensors, the suffix (i.e., A-1, A-3, and A-4) indicates the width of magnet used, in inches. The 4-in. magnet is made up of one 1-in.- and two 1.5-in.-wide magnets operating in parallel. The size and shape of the Alnico-8 magnets used in the Type-A probe are shown in Fig. I.B.1. This magnet shape is necessary to allow fabrication of the probe.

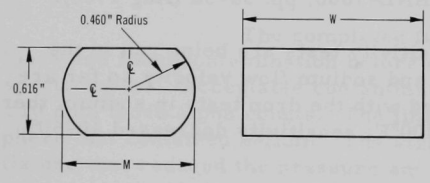

Fig. I.B.1. Flowsensor Magnets

The magnets are insulated from the Type 304 stainless steel cylindrical housing by a thin sheet of mica. Although the mica has satisfactorily maintained its physical and insulating properties at >1200°F, no

information is available yet on how the mica will be affected by the gamma fields and fast-neutron fluxes expected in the FFTF reactor.

Attempts to use ceramic flame-spraying equipment to apply a suitable thin coating of high-purity alumina to the very hard surface of an Alnico-8 magnet have been unsuccessful so far. The Metallizing Co. of America is assisting in further efforts. Coating the inside walls of the cylindrical housing of the flowsensor magnet appears to be a possible solution to the problem.

From the recorder charts obtained in the flowsensor tests, the sensitivity of each flowsensor was calculated at the maximum flow velocities used in the tests:

	Flowsensors			
	A-1	A-1¾	A-3	A-4
Sensitivity, ~mV per ft/sec	0.31	0.362	0.54	0.61

Flowsensor A-1¾ is Flowsensor A reported in ANL-7595. Flowsensor A-4 exhibits a 69% larger signal than the Flowsensor A-1¾ design. Flowsensor A-4 will be modified and then will be tested at elevated temperatures in the CAMEL loop--both before the magnet is temperature stabilized for operation at 1200°F and again after temperature stabilization.

The preparation of specifications for procurement of a similar flowsensor (with an Alnico-8 magnet of greater width for further optimization of the signal) from a commercial source has been started.

(ii) Gas Disengagement for Failed-fuel Monitoring (E. S. Sowa)

(a) Sodium Test Loop

Last Reported: ANL-7561, pp. 21-22 (March 1969).

The completion of the slow-flow tests in the Fuel Failure Detection Loop (FFDL) was followed by loop shutdown to modify it so that a prototype of the Failed Element Detection and Location (FEDAL) module can be installed.

The FEDAL module prototype to be tested was designed to simulate the functional behavior of the module design represented by drawings received from Battelle-Northwest Laboratory. However, the laboratory prototype is being constructed as a modular assembly that permits convenient disassembly and variation of individual features, if needed.

The design also allows the replacement of the gas-separation cascade assembly within the utility chamber so that different configurations can be tested and relative performance evaluations can be made.

The existing external gas-circulation and fission-gas detection chamber will be retained because it does not alter the fundamental performance of the module.

Additional modifications to the loop include enclosure of the lower portion of the loop within an airtight sheet-metal enclosure. In addition, the sample-holder O-ring was modified by the inclusion of an internal shoulder along the inner periphery so that positive seating will be obtained. The sample flange will also be enclosed by a small secondary container to localize possible sodium leakage.

2. Fuel Handling, Vessels and Internals

a. Core Component Test Loop (CCTL) (R. A. Jaross)

Last Reported: ANL-7618, p. 19 (Sept 1969).

(i) Loop Modifications to Accommodate Second FFTF Subassembly. Modifications to the CCTL to accommodate the Mark-II fuel assembly and to improve loop reliability are proceeding.

On the 2-in. pump-bypass piping, the twelve welds required to install the bypass between the pump-bearing overflow and the suction of the pump have been completed, radiographed, and accepted. A leak-detection spark-plug device has been installed on the 2-in. valve of the pump bypass loop, as have pipe preheaters for the bypass loop and valve, and a 0.004-in.-thick Type 304 stainless steel anti-stress-corrosion baffle. Twelve thermocouples have been installed on the bypass-loop piping, as has the first layer of a two-layer 1200°F insulation. A manually operated valve hand-wheel extension has been installed so that the valve can be operated from outside the CCTL enclosure.

For the 4-in. flowtube, all heaters, thermocouples, and anti-stress-corrosion baffles have been installed. Ten of the twelve welds have been completed and their radiographs have been approved; the two remaining welds are for installation of the Taylor pressure-sensor element.

One of the ten welds is being evaluated ultrasonically. This weld, which is at the inlet-discharge straight length of the flowtube where the flow changes direction (90°) from the pump inlet, is subjected to greater stresses than other welds in the 4-in. pump-to-vessel pipe. A "prooftest" 90°-to-straight-pipe section has been prepared using welding procedures

identical to those used for CCTL. It will serve as a standard to which ultrasonic evaluation of the CCTL weld area can be compared.

All shop work for modification of the CCTL test vessel has been completed. For component installation, the downcomer or subassembly inlet and the subassembly holddown framework are being completed. The in-vessel pressure transducers for the subassembly inlet have been recalibrated (at five pressure increments at each of four temperatures), installed, and their radiographs have been approved. The 36-in.-OD ceramic-filled Flexitallic gaskets for the flange between the instrument spool piece and vessel have been delivered.

The report on all metallurgical measurements, tests, and evaluations to determine the suitability of the CCTL for continued operations has been prepared. The report indicates that there is no significant degradation of surveillance samples or pipe specimens as a result of CCTL service conditions to date.

The radiographs of the original CCTL piping welds that were accessible during the loop modifications show that all 27 welds are "all clear."

After completion of radiography, the installation of the leak-detection devices on each drain valve has been completed.

All thermocouples, heaters, anti-stress-corrosion baffles, and thermal insulation also have been reinstalled.

C. Sodium Technology

1. Sodium Chemistry

The basic work on sodium chemistry is directed toward the development of a sound scientific foundation for understanding the behavior of sodium's common nonmetallic contaminants, for interpreting and evaluating existing corrosion data, and for predicting potential corrosion problems in sodium systems.

a. Studies on Carbon Transport in Sodium-Steel Systems (K. Natesan, J. Y. N. Wang, and T. F. Kassner)

Last Reported: ANL-7618, pp. 20-21 (Sept 1969).

The thermodynamic activity and solubility of carbon in Fe-Cr-Ni alloys have been calculated in the temperature range 500-800°C by extrapolation of data at higher temperatures in the ternary Fe-Cr-C and Fe-Ni-C

systems. The compositional range for the alloys included that of an 18-8 austenitic stainless steel. These results have been used with phase-equilibria information and selected published data for the solubility of carbon in sodium to obtain an equilibrium relationship between the total carbon content of the alloys (carbon in austenite + carbon in the carbide) and carbon concentrations in sodium. Such a relationship for an 18-8 stainless steel is shown in Fig. I.C.1. The calculations show that sodium, depending on its carbon content and temperature in the range from 500 to 800°C, may either carburize or decarburize the Fe-Cr-Ni alloys at typical commercial carbon levels. Figure I.C.2 shows the temperature dependence of the equilibrium between the Fe-Cr-8 wt % Ni alloy containing 12, 15, and 18 wt % Cr, carbon in sodium, and $M_{23}C_6$-type carbide. As indicated in Fig. I.C.2, the computed carbon concentrations in sodium for incipient carbide formation in an 18-8 stainless steel in equilibrium with sodium below 700°C are significantly lower (i.e., below 1 ppm) than carbon concentrations commonly reported (i.e., 15-30 ppm).

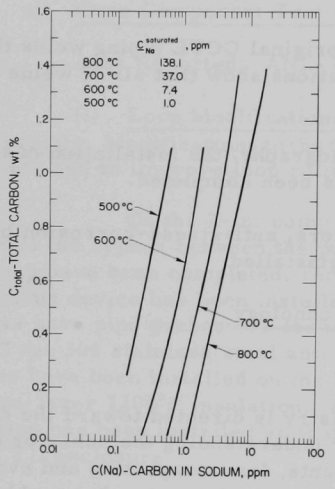

Fig. I.C.1. A Plot of Total Carbon in Fe-18 wt% Cr-8 wt % Ni Alloy vs Carbon Concentration in Sodium at Different Temperatures. The carbide contribution to the total carbon in these curves is from the $M_{23}C_6$ type.

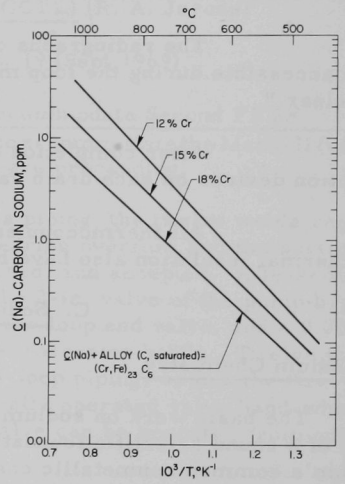

Fig. I.C.2. Temperature Dependence of Fe-Cr-8 wt % Ni Alloy (C Saturated)-C(Na)-Carbide Equilibrium

The phase-equilibria and activity data explain the observed phenomenon of transfer of carbon from austenitic stainless steel to sodium when chromium depletion, due to mass transfer, occurs.

In addition, the driving force for carbon transfer from ferritic steel to austenitic stainless steel under isothermal conditions was calculated. Carbon transfer from a Fe-2.25 wt % Cr-1 wt % Mo-0.1 wt % C steel (Croloy $2\frac{1}{4}$) to an 18-8 stainless steel under isothermal conditions is inevitable at temperatures above 525°C.

b. Characterization of Carbon-bearing Compounds in Liquid Sodium

(i) Characterization of Disodium Acetylide (F. A. Cafasso)

Last Reported: ANL-7577, p. 176 (April-May 1969).

It has been postulated* that carbon transport between steels in sodium systems involves dissolved disodium acetylide (Na_2C_2). Accordingly, information on the stability and solubility of Na_2C_2 in sodium is being obtained.

(a) Stability of Na_2C_2. The thermal stability of solid Na_2C_2 (99.5% purity) is being studied by differential thermal-thermogravimetric analysis (under 1 atm of helium pressure) and by high-temperature X-ray powder diffraction. The differential thermal analysis thermogram exhibited a reversible, endothermic peak at 275°C. This peak was shown by the X-ray study to be associated with a transition of the solid from tetragonal (low-temperature) to cubic (high-temperature) symmetry. No other significant features appeared in the thermogram up to about 700°C, whereupon vaporization and consequent loss of sodium became significant.

(b) Stability of Na_2C_2 in Sodium. The stability of Na_2C_2 in the presence of sodium is being studied. Copper capsules were loaded with about 4 g of sodium per gram of Na_2C_2 and were welded closed in an inert-atmosphere box. The capsules were heated to selected temperatures for selected periods of time, and then cooled and opened. The entire contents of the capsules were dissolved in water, and the off-gases thus generated were analyzed for acetylene by gas chromatography. Preliminary results indicate that after about 65 hr of heating, the acetylide was 44% decomposed at 400°C and >95% decomposed at 630°C. Additional experiments of this kind are now in progress.

(c) Solubility of Na_2C_2 in Sodium. An attempt is being made to measure the solubility of Na_2C_2 in liquid sodium over the temperature range in which it is stable. The method involves equilibrating reactor-grade sodium with excess Na_2C_2 at a preselected temperature, withdrawing a sample of the melt through a copper or tantalum filter into either a copper

*Luner, C., Feder, H. M., and Cafasso, F. A., "Carbon Transport in Liquid Sodium," in Proceedings of the International Conference on Sodium Technology and Large Fast Reactor Design, ANL-7520, Part I, p. 455 (1968).

or tantalum pipette, dissolving the sample in water, and assaying the resulting off-gas for acetylene by gas chromatography. Preliminary results indicate that the acetylide ($C_2^{=}$) content in sodium ranges from <1 ppm near the melting point of sodium at 98°C to about 25 ppm near 380°C.

2. Sodium Analytical Development

Not previously reported.

A sodium analytical group has been organized at ANL-Illinois with the responsibility of certifying standard methods of sodium analysis for all laboratories performing AEC-sponsored sodium technology programs.

a. Development of Reference Analytical Methods of Oxygen, Carbon, and Nitrogen (R. J. Meyer)

Prior to certification, a method will be evaluated with regard to such criteria for sodium analysis as accuracy, specificity, useful range, and sensitivity. To date, evaluations of chemical analyses for interstitial impurities in sodium at the parts-per-million level have been based on the degree of precision attainable, because standard samples are not available and no method is generally recognized as a reference method. Reference methods having sensitivites of the order of 100 ± 10 ppb are needed within the LMFBR program to certify the quality of other methods of sampling and analysis (including on-line purity monitors) and to aid in establishing acceptance standards for reactor-grade sodium. Such reference analyses would not be done on a routine basis, nor by nonskilled operators.

Activation analysis as a reference method has the following potential advantages: (1) high sensitivity and specificity, (2) freedom from the difficulties caused by outside contamination once the activation step is completed, and (3) independence of the chemical form of the activated element. The initial effort on development of reference methods is being directed toward the selection of an activation technique suitable for oxygen in sodium.

(i) Analysis for Total Oxygen in Sodium. The accuracy and sensitivity attainable by activating oxygen in sodium depends strongly on whether neutron activation, high-energy gamma activation (by bremsstrahlung radiation), or charged-particle activation is employed. Thermal-neutron activation, although by far the simplest experimental technnique, is entirely inappropriate since capture cross sections are small for light elements.* Irradiation by fast neutrons

*Stehn, J. R., Goldberg, M. D., Mogarno, B. A., and Wiener-Chasman, R., Neutron Cross Sections, BNL-325, Vol. I, Suppl. 2 (1964).

or high-energy gamma rays causes activation of the sodium itself, so that fast chemistry to separate the 2-min ^{15}O activity is necessary.* Reduction of the bremsstrahlung energy to diminish the activities of sodium and other interfering substances** results in loss of sensitivity for oxygen activation. These restrictions limit the sensitivity of the fast-neutron and gamma-activation methods to about 5 ppm oxygen in sodium, and little hope exists for extending them much below this concentration.

Activation with proton, deuteron, helium-3, or helium-4 beams has become an important, general tool† for assaying carbon, nitrogen, and oxygen in the ppb range, despite the disadvantages of short-distance penetration and considerable heat generation in the target. The first disadvantage leads to surface activation rather than volume activation; the second causes serious problems with sample vaporization unless the usable beam intensity is severely curtailed. Because sodium is readily liquefied and has good heat-transfer properties as a liquid, both disadvantages can be circumvented. By liquefying the sodium and stirring it in a thin-windowed cell, the entire sample can be activated. The stirring prevents localized heating and hence diminishes vaporization of sodium. Accordingly, activation of molten, well-stirred sodium will be investigated as a method for determining oxygen content.

Proton activation, namely, the (p,n) reaction on ^{18}O that leads to positron-emitting ^{18}F, has been chosen because it has a sensitivity of about 10^{-5} ppm for ^{18}O and, consequently, about 10^{-2} ppm for total oxygen.†† Moreover, unlike other charged particles, low-energy protons will not appreciably activate the sodium. If any interfering activities should arise from impurities (e.g., calcium) in the sodium, the sought-after 110-min ^{18}F activity is sufficiently long-lived to permit separation chemistry to be performed. Irradiation cells are being designed that will allow 100-g samples of liquid sodium to be stirred while being bombarded with the external 15-μA proton beam (11.5 MeV) of the ANL cyclotron. If preliminary experiments prove encouraging, techniques will be devised to perfect and standardize this analysis for use as a reference method.

3. On-line Monitors

a. Evaluation and Improvement of the Hydrogen-Activity Meter (J. Holmes)

Not previously reported.

ANL has recently undertaken the responsibility for developing a hydrogen meter for liquid sodium systems. Hydrogen meters have three

*Lutz, G. J., The Determination of Oxygen in Sodium by Photon Activation Analysis, presented at the 158th National ACS Meeting, New York, N. Y. (Sept 1969).

**Engelmann, C., and Louillet, M., Bull. Soc. Chim. Fr. 2, 680 (1968).

†Proceedings of the 2nd Conference on Practical Aspects of Activation Analysis with Charged Particles, EUR-3898 d-e-f Ebert. H. G. (Ed.) (1968).

Rev. Phys. Appl. 3, 365 (1968).

important applications in the LMFBR program: (1) to detect as quickly as possible water leaks in steam generators, (2) to serve as on-line monitors for hydrogen impurities in primary and secondary sodium systems, and (3) as detectors in research and development programs on basic sodium chemistry and on cold trapping, gettering, and other methods of sodium purification. The ANL studies of the hydrogen meter will be directed to all three applications, but the initial emphasis will be on its use as a leak detector for sodium-steam heat exchangers.

A review of the state of the art has indicated that the combination of a metal diffusion membrane (nickel or iron) and a high-vacuum system with a mass-spectrometer detector is the most promising form of hydrogen meter for leak detection. In an alternative and possibly simplified version, an ion-pump would be used as the detector, with the current being monitored as an indication of the hydrogen flux. Either detection system should give quantitative results if calibrated and should be satisfactory for detecting water or steam leaks into sodium. Preliminary calculations indicate that a detection system employing a 10-mil nickel membrane will respond within about 10 sec to a step change in the hydrogen concentration at 500°C. Equipment for a metal membrane/high-vacuum system is being purchased and fabricated, and will be tested on the Sodium Analytical Loop (SAL).

4. Fission Product Behavior and Control

a. Low-level Irradiation Tests (W. E. Miller)

Not previously reported.

Work on defining the problems associated with transport and deposition of fission products in flowing sodium systems is under way. Preliminary results of this continuing study indicate the importance of investigating the behavior of short-lived fission products. The design and construction of small-sized equipment (holding 1-2 gal sodium) is being considered.

Gamma spectroscopy would be used in the identification of key isotopes. Since the presence of ^{22}Na and ^{24}Na from the irradiation of sodium would further complicate the already complex gamma spectra of mixed fission products, fuel targets will be irradiated while separated from the sodium and then quickly inserted into the flowing sodium. The irradiation source (reactor or neutron generator) has not been chosen yet.

The target-transport mechanism, target-change mechanisms, gas system, fission gas traps, and sodium fill-supply system would all be permanent installations. Replacement of the tubing through which the sodium flows is necessary to avoid having the residues from one experiment interfere with the next. This portion of the equipment will be

disconnected from the irradiation tube by means of a freeze seal and then transported to a shielded cask for eventual disposal. Removal and replacement would be done with a minimum of remote operation.

b. Development of a Continuous Radioactive Contaminant Removal Process (H. M. Feder and F. A. Cafasso)

Not previously reported.

This investigation seeks methods for the continuous purification of the coolant sodium in a fast breeder reactor system. Harmful impurities may be introduced into the coolant from the atmosphere, from structural materials, or from fuel elements. Major emphasis has previously been placed on restricting the sources of contamination or on the removal of contaminants by hot or cold trapping. These approaches place severe limitations on the design and operation of the reactor; in addition, the removal procedures that have been developed are cumbersome and ineffective for certain impurities.

The removal of a wide spectrum of contaminants from sodium into a discardable waste stream is being sought. One possible method of accomplishment may be a semibatch solvent-extraction system installed in a bypass loop and operated at a temperature of ~150°C. The extracting phase must necessarily have extremely small miscibility with and reactivity toward sodium.

A literature search has been conducted to ascertain, by elimination, whether or not materials having the desired properties do exist. This process has led to the selection of several classes of high-boiling organic compounds expected on theoretical grounds to have the necessary very low reactivity toward hot sodium. Preliminary tests of representative compounds from each class for long-term inertness toward sodium at 150°C will be conducted. Appropriate equipment for these tests has been designed and ordered and will be assembled shortly.

5. Cover-gas Monitoring

a. Nature and Control of Sodium Aerosol Formation (W. E. Miller)

Not previously reported.

The objective of this work is to assess the magnitude of formation of sodium aerosol at proposed LMFBR conditions. Proposed LMFBR sodium temperatures during normal reactor operation range from 800 to 1200°F. The corresponding range of sodium vapor pressure is 0.73 to 52 Torr. In the pool-containment approach (used at EBR-II and proposed for LMFBRs), the cover gas is exposed to the full range of sodium temperatures.

The fraction of sodium vapor condensed to aerosol on cooling the sodium vapor-carrier gas mixture will depend on the ratio of thermal diffusivity to mass diffusivity in the mixture. High mass diffusivity will tend to promote direct condensation on the cooler surfaces above the sodium pool, whereas a low mass diffusivity will tend to promote aerosol formation within the cool gas-boundary layers. However, no experimental data on the diffusivity of sodium vapor has been found. For nonpolar simple gases, diffusivities may be estimated from viscosities; correlations for making such estimates for sodium are being examined.

The first experiments will be done in an inert-atmosphere glovebox. Sodium will be heated in a long tube cooled at one end, and an attempt will be made to view aerosol formation through a Pyrex window in the tube. The gas phase will be sampled and analyzed to determine the mass concentration of sodium aerosol.

6. Materials Compatibility

a. Candidacy of Vanadium-base Alloys for Cladding LMFBR Fuels (T. F. Kassner, K. Natesan, and C. A. Youngdahl)

The objective of this program is to develop enough understanding and information so that a first assessment of the adequacy of vanadium alloys as fuel cladding for LMFBR can be made.

(i) Rotating-disk Corrosion Studies

Not previously reported.

The corrosion of vanadium in liquid sodium is being investigated under the well-defined hydrodynamic conditions produced by the rotating-disk sample geometry. Data were obtained by removing the disk sample from the sodium at several time intervals and determining the weight and dimensional changes. For a number of rotational speeds, the amount of metal lost at 600°C varied directly with time. The linear time law had also been followed during earlier 80-day exposures of vanadium and vanadium-base alloys in loop experiments* under conditions of temperature and oxygen concentration in sodium where weight losses were observed.

The effect of velocity on the corrosion rate at 600°C and 16 ppm oxygen in sodium is shown in Fig. I.C.3. The region of laminar flow (i.e., $Re = 1 \times 10^3$ to 1×10^5) in these experiments corresponds to a range of rotational speeds between 5 and 500 rpm. The dependence of the corrosion rate on the half-power of the rotational speed at the higher

*Ruther, W. E., The Corrosion of Vanadium and Vanadium-Base Alloys in Liquid Sodium, ANL-7505 (May 1969).

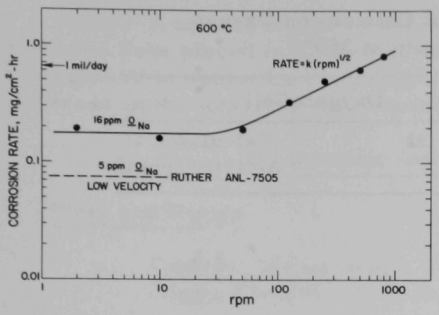

Fig. I.C.3. The Effect of Disk Velocity on the Linear Corrosion Rate of Vanadium in Sodium Containing 16 ppm Oxygen at 600°C

velocities is indicative of a liquid-diffusion-controlled corrosion process. Either oxygen diffusion to the metal surface or the diffusion of corrosion product away from the disk is limiting the reaction rate. Experiments are in progress to determine the effect of oxygen concentration in sodium on the corrosion rate at a velocity of 250 rpm. From these data it can be established which of these processes is rate-limiting.

In the rotating-disk corrosion experiments, the oxygen concentrations in sodium are determined by the vacuum distillation method. These data are correlated with oxygen concentrations from solubility data* at the cold-trap temperature and emf values obtained from United Nuclear Corp. oxygen meters. An electrode assembly that failed after one year in sodium at 337°C was replaced recently and is operating satisfactorily. The other electrode assembly that has been in operation for over 18 months developed a sensitivity to changes in ambient temperature. Thermostats have been installed on both electrode assemblies to minimize the problem.

(ii) The Effect of Calcium on the Solubility and Activity of Oxygen in Sodium

Last Reported: ANL-7606, pp. 31-33 (Aug 1969).

The addition of calcium to sodium is known to decrease the activity of dissolved oxygen to very low values. From this decrease it can be predicted that vanadium alloys in contact with such sodium will contain less oxygen. If the calcium concentration required to limit oxygen content of vanadium alloys to an acceptable level is low enough so that structural components are not adversely affected, the technical feasibility of using vanadium alloys will be greatly improved.

Studies of the effect of calcium on the activity of oxygen in solution in sodium at 350°C are in progress, using United Nuclear Corp. oxygen meters. In one series of measurements, incremental calcium additions to sodium were made. Following each addition the oxygen cell was allowed to reach a steady value, samples were distilled, and the residues were analyzed for sodium and calcium. Typically, several hours were required for cell voltage stabilization. The results are given in Table I.C.1. As the total calcium was increased, consistent reduction of oxygen activity was indicated by the oxygen cell. The results of chemical analysis are incomplete.

*Kassner, T. F., and Smith, D. L., ANL-7335 (Sept 1967).

TABLE I.C.1. Effect of Calcium on Oxygen Activity in Sodium at 350°C

Total Ca Added (ppm)	Oxygen Cell	
	Potential (V)	Calculated O Activity (ppm)
0	1.155	8.2
25	1.172	3.5
43	1.316[a]	0.05

[a]A steady potential could not be maintained.

Experiments at 350°C with a higher initial oxygen concentration (about 15 ppm) in sodium are in progress.

b. Analysis of Nonmetallic Impurities in Sodium by Equilibration of Refractory-metal Wires (D. L. Smith and R. H. Lee)

Last Reported: ANL-7577, pp. 153-155 (April-May 1969).

The equilibration technique with vanadium, niobium, and tantalum wires has been used to measure the oxygen concentration in EBR-II primary sodium. The wires were exposed in position 4C3 of the core for 517 hr with the reactor operating at the 50 MW power level. The sodium temperature at the exposure position was estimated to be 477°C.

Apparently, the vanadium wire had corroded completely since it was not found when the capsule was opened. This indicates that the oxygen concentration of the reactor coolant was above that (<0.1 ppm) required to oxidize vanadium to vanadium oxide. This result is not unexpected as the solubility of oxygen in sodium at the cold-trap temperature of ~121°C is 0.68 ppm.*

The tantalum wire was highly radioactive after exposure, and only qualitative analyses were performed. The wire was ductile and did not appear to have lost significant weight.

The niobium wire was recovered and analyzed first by internal friction and then by vacuum fusion for oxygen, nitrogen, and hydrogen. The internal-friction measurements indicated an oxygen concentration greater than 0.5 ppm oxygen in sodium. This is the maximum concentration that can be determined by equilibrating niobium wires at this low exposure temperature. The vacuum fusion results are incomplete.

*Ibid., see previous page.

A second series of wires (V, Nb, V-10 wt % Cr, and V-20 wt % Cr) have been placed in EBR-II prior to the run at 62 MW. The increase in exposure temperature resulting from the higher power level and the decrease in the exposure time should provide more quantitative results.

D. Systems and Plant Development

1. Plant and Design

a. Contract Management, Technical Review, and Evaluation (L. W. Fromm and K. A. Hub)

Last Reported: ANL-7618, p. 23 (Sept 1969).

(i) Evaluation of 1000-MWe Follow-on Study Task Reports. The ANL evaluation of the Westinghouse Task-I report has been transmitted to Westinghouse for comment. This evaluation will be included in the final ANL quarterly evaluation report that is being prepared.

The evaluation of the Task-II, -III, and -IV reports of all contractors is proceeding on schedule. Approximately 30% of the evaluation has been drafted. A draft of the evaluation report should be completed by January 16, 1970.

E. EBR-II--Research and Development

1. New Subassemblies and Experimental Support (E. Hutter)

a. Experimental Irradiation Subassemblies (O. Seim)

Last Reported: ANL-7618, pp. 24-29 (Sept 1969).

(i) Mark-L61 Irradiation Subassembly (O. Seim and W. Ware)

The preliminary design of a new subassembly for in-pile creep studies has been started. This subassembly will have the same external dimensions and configuration as previous subassemblies. Internally, however, a unique structural arrangement is necessary to provide the proper environmental conditions for the experiment.

The experiment will comprise an array of 61 sealed and pressurized tubes. Each tube will be 40 in. long and 0.230 in. in diameter. Spiral spacer wires, used in previous subassemblies, will not be used because they might interfere with the anticipated changes in tube diameters. Tube spacing will be maintained only at the ends of the tubes. During initial tests, the tube-wall temperatures will be kept at an average of approximately 750°F within the 900°F environment of the core. Therefore, a thermal shield will be provided around the entire length of the 61-element tube bundle. The shield will be similar to the one in the Mark J-19 (see ANL-7618). It will comprise a hexagonal liner tube inside of the outer hexagonal tube, with a 1/16-in. annulus between the tubes. The annulus will be sealed at the top so that primary-tank blanket gas (argon) will be trapped and held in the annulus when the subassembly is lowered into the primary tank. The argon-filled annulus will form an efficient thermal barrier.

For low-temperature experiments, the shield will reduce transfer of heat from the hotter adjacent subassemblies. A high rate of sodium flow will be used to keep the specimens at the desired temperature.

2. Instrumented Subassemblies (E. Hutter and A. Smaardyk)

a. Test One and Two

(i) Assembly of Test-2 Subassembly (C. Divona)

Previously Reported: ANL-7618, pp. 29-30 (Sept 1969).

After brazing of the bulkhead, leaktesting of the leads disclosed a leak in the 1/8-in. pressure-transducer gas tube of capsule No. 11. Further investigation showed that the leak was at the bulkhead braze elevation on the drywell side. Microscopic examination showed a

hairline crack in the tube, which extended ~120° around the tube. The crack was at the surface of the high-nickel braze material (Coast Metal 60) which had been used to braze the tube into the bulkhead.

It was decided to repair the crack by brazing with an alloy having a melting point somewhat lower than the 1182°C melting point of Coast Metal 60. Rebrazing with Coast Metal 60 or any other material with a similar or higher melting point would have remelted the bulkhead braze and jeopardized all the leads in the bulkhead.

Test brazes with two nickel alloys having a lower melting point than Coast Metal 60--Nioro (mp, 950°C) and Nicusel (mp, 795°C)--were made in reducing atmospheres. Tests of several brazed samples showed that these brazing alloys either were too active or did not flow.

One test silver braze was made with an alloy called Easyflow (mp, 650°C), using manually applied heat and a flux. This method combined the advantages of low melting point, good flow characteristics, and local application. It had, however, the disadvantage of using a rather corrosive flux. A second test braze made with this alloy and the same flux was tested at 900°F while pressurized to 100 psig. After 300 hr at these conditions, no corrosive effect was detected by leak checks. This test will be continued for several months.

The crack in the pressure-transducer gas tube was repaired by silver brazing the cracked area manually. A split sleeve was placed over the cracked region, and the sleeve and bulkhead were heated locally with a torch. Then, the silver-brazing alloy, used with a flux (Handyflux), was applied. Subsequent helium leaktesting of the braze showed no leakage greater than 2×10^{-10} cc/sec of helium.

The remaining extension-lead junctions were completed, and all extension leads and tubes were fastened to the drywell liner tube. The outer extension tube was installed over the drywell inner tube after the extension leads had been covered with an 0.002-in.-thick stainless steel sheath to protect the quartz insulation. The integrity of the extension leads was subsequently tested by electrical measurements and found to be satisfactory. The outer extension tube then was welded to the bulkhead and leaktested.

With the subassembly vertical, steel shot was poured into the shielding zone, and a silicone-rubber compound was poured over the shot to form a retaining barrier. After returning the subassembly to the horizontal position, the coupling was installed, and the coupling seals were satisfactorily leaktested. The terminal box was installed on the extension tube, and the four pressure-transducer gas fittings were connected and leaktested. A bellows was provided between the flux-monitor tube and the

sodium-shutoff valve within the terminal box to allow for differential expansion between that tube and the extension tube.

Wiring of the terminal box connectors has begun.

(ii) Shipping Container for Instrumented Subassembly Test 2

Not previously reported.

A shipping container has been constructed for transporting the test-2 instrumented subassembly, containing unirradiated fuel capsules, to the EBR-II site. The container is required to give adequate support and to prevent transmission of shock loads to the subassembly during transport. Considerable rigidity and shock-absorbing capability have been designed into the container. It consists of a large, rigid outer box, weighing approximately 7006 lb, into which a smaller box, weighing approximately 1200 lb, fits with approximately $1\frac{1}{2}$-in. clearance. The space between the inner and outer boxes is filled with urethane pads.

The outer box, 22 in. x 24 in. x 38 ft long, is constructed of steel and has shock-absorbing pads spaced at 4-ft intervals.

The inner box, 10 in. x 8 in. x 37 ft long, is constructed of steel, and has rubber-bushed clamps to support the instrumented subassembly at $5\frac{1}{2}$-ft intervals along its length. The terminal-box flange of the subassembly will be bolted to the top clamp. The inner box not only will rigidly support the subassembly during shipping, but will protect the subassembly while it is being handled at EBR-II prior to installing it in the reactor.

An engineering analysis of the container was made to see if it would meet the safety regulations imposed on containers for shipping radioactive materials in "Safety Standards for Packaging of Radioactive and Fissile Materials," AEC Appendix 0529. This analysis was principally addressed to (1) possible significant chemical, galvanic, or other reactions of the packaging components and contents; (2) closure integrity under various loadings; (3) adequacy of lifting devices; and (4) consideration of solar heating and low ambient temperatures. The results of the analysis indicate that the shipping container will meet the regulations.

3. Coolant Chemistry (D. W. Cissel)

a. Sodium Coolant Quality Monitoring and Control

Last Reported: ANL-7618, pp. 31-34 (Sept 1969).

(i) Analytical Cold Trap (O. Seim, E. Filewicz, and P. Elias)

To permit the analysis of various compounds or elements that precipitate in a cold trap throughout its range of temperatures, a small

analytical cold trap is being designed for the EBR-II radioactive sodium chemistry loop. A prototype analytical cold trap will be contructed to verify temperature distribution using nonradioactive sodium. Preliminary studies indicate that the cold trap should be 48 in. long and should include a segmented titanium central tube of approximately 1-in. diameter which is surrounded by a 2-in.-dia tube. A segmented tube was chosen for convenience in analysis.

Sodium at a temperature of 700°F will enter through the top of the trap, pass down the central tube, and leave the bottom of the tube at a temperature of 220°F. The sodium then will flow upward through the annulus between the two tubes, leaving the top of the annulus at a temperature of 660°F. Air cooling will be applied to the lower 18-in. portion of the 2-in. tube, which will be finned externally, to establish and maintain the desired temperature relationships. Proper selection of the length of the regenerative heat-transfer surface on the central tube and of the amount of air-cooling surface on the outer tube is critical in establishing the temperature distribution throughout the cold trap. Heat transfer calculations have shown the significance of variations in the areas of these heat-transfer surfaces.

4. Experimental Irradiation and Testing (R. Neidner)

a. Experimental Irradiations

Last Reported: ANL-7618, pp. 34-35 (Sept 1969).

Table I.E.1 shows the status of the experimental subassemblies in EBR-II as of October 15, 1969.

5. Systems Engineering (B. C. Cerutti)

a. Surveillance, Evaluation and Studies of Systems

Last Reported: ANL-7618, pp. 37-40 (Sept 1969).

(i) Surveillance of System Performance at 62.5 MWt. All systems operated satisfactorily during the run at 62.5 MWt. The turbine-driven feedwater pump was able to carry the fuel feedwater load up to 62.5 MWt. Although the steam consumption of the feedwater-pump turbine was higher than the manufacturer's performance curves indicate, no control problems were encountered. The main turbine generated about 18,600 kWe (throttle steam flow ~170,000 lb/hr) with the reactor at 62.5 MWt. This is in agreement with the values predicted for operation at 62.5 MWt.

During the increase of power to 62.5 MWt, acoustical measurements were obtained from each of the two superheaters. A frequency spectrum was determined from accelerometers located at three different

TABLE I.E.1. Status of EBR-II Experimental Irradiations as of October 15, 1969

Subassembly No. and (Position)	Date Charged	Capsule Content and (Number of Capsules)		Experimenter	Accumulated Exposure (MWd)	Estimated Goal Exposure (MWd)	Burnup[b]
XG03[a] (7D1)	7/16/65	UO_2-20 wt % PuO_2	(2)	GE	24,845	28,700	6.4
XG04[a] (7B1)	7/16/65	UO_2-20 wt % PuO_2	(2)	GE	26,041	45,000	6.7
XO18B[c] (4E2)	10/2/69	Structural	(3)	GE	535	10,000	0.2 + 5.8[d] = 6.0
		Structural	(2)	ANL			0.2 + 5.8[d] = 6.0
		Structural	(1)	ANL			0.2
		Structural	(1)	PNL			0.2
XO20[a] (6B5)	1/13/67	UO_2-PuO_2	(9)	GE	16,004	20,400	6.5
		UC-20 wt % PuC	(3)	UNC			7.1
		Structural	(4)	PNL			4.5
		Structural	(2)	ANL			4.5
		Graphite	(1)	PNL			4.5
XO21B (2D1)	2/23/69	Structural	(6)	PNL	16,175	23,200	3.0 + 4.1[d] = 7.1
		Structural	(1)	PNL	7,211	9,000	3.0
XO27[a] (4B3)	11/21/67	UO_2-25 wt % PuO_2	(18)	GE	13,327	16,000	7.5
		Structural	(1)	PNL			5.3
XO33[a] (5B4)[e]	12/22/67	UC-20 wt % PuC	(19)	UNC	12,474	12,200	6.2
XO34A[c] (2F1)	9/30/69	Structural	(4)	ORNL	535	3,800	0.3 + 4.8[d] = 5.1
		Structural	(3)	ORNL			0.3
XO35 (7B3)	4/13/68	Structural	(7)	ORNL	13,119	44,800	3.0
XO36[a] (7E1)	7/25/68	UO_2-25 wt % PuO_2	(19)	GE	10,725	43,300	2.8
XO38 (7C5)	5/7/68	Structural	(7)	INC	12,701	17,700	2.7
XO40A[c] (5B2)	9/30/69	UO_2-20 wt % PuO_2	(18)	ANL	535	4,800	0.3 + 3.5[d] = 3.8
		UO_2-20 wt % PuO_2	(16)	GE			0.3 + 3.6[d] = 3.9
XO41 (7A3)	7/24/68	Structural	(7)	PNL	11,161	16,700	2.4
XO43[a] (4D2)	2/20/69	UO_2-25 wt % PuO_2	(37)	GE	6,441	11,000	3.5
XO44 (7A1)	8/28/68	Oxide Insulator	(1)	LASL	9,836	12,000	1.6
XO50[a] (4C2)	2/23/69	UO_2-20 wt % PuO_2	(4)	GE	6,441	7,500	3.6 + 7.7[d] = 11.3
		UO_2-28 wt % PuO_2	(4)	GE			3.5
		UO_2-20 wt % PuO_2	(5)	ORNL			3.5
		UC-18 wt % PuC	(2)	W			3.5
		Structural	(4)	GE			2.5 + 5.3[d] = 7.8
XO51[a] (3A2)	12/16/68	UO_2-25 wt % PuO_2	(37)	PNL	6,986	16,400	1.4
XO54[a] (4E1)	3/31/69	UO_2-25 wt % PuO_2	(37)	PNL	5,841	10,000	3.1
XO55 (6A4)	2/23/69	UC-15 wt % PuC	(19)	UNC	7,211	20,000	2.3
XO56[a] (5C2)	4/2/69	UO_2-25 wt % PuO_2	(37)	GE	5,841	10,600	2.9
XO57 (2B1)	2/23/69	Structural	(7)	PNL	7,211	15,000	3.0
XO58[a] (6F1)	4/24/69	UO_2-25 wt % PuO_2	(37)	GE	5,265	16,000	1.9
XO59[a] (4A1)	4/23/69	UO_2-25 wt % PuO_2	(37)	PNL	5,265	17,500	1.8
XO61 (7A5)	4/23/69	Structural	(7)	INC	6,035	18,000	1.3
XO62[a] (6F3)	5/23/69	UO_2-25 wt % PuO_2	(37)	GE	4,033	13,400	1.8
XO63 (7F5)	6/29/69	Magnetic Materials	(7)	ANL	3,701	5,400	0.8
XO64[a] (4F2)	5/28/69	UO_2-25 wt % PuO_2	(19)	GE	4,033	10,700	2.3
XO65A[c] (7E5)	10/2/69	Structural	(23)	ANL	535	600	0.1 + 0.3[d] = 0.4
XO69[c] (4F1)	10/1/69	UO_2-25 wt % PuO_2	(37)	PNL	535	20,700	0

[a]Temporarily removed to storage basket for Run 38A.
[b]Approximate accumulated center burnup on peak rod (fuels, at. %; nonfuels, nvt x 10^{-22}).
[c]New or reconstituted subassembly charged in reactor grid for Run 38B.
[d]Previous exposure from another subassembly.
[e]XO33 was relocated to 5B4 for Run 38B.

locations on each superheater. The frequency range analyzed was 2-500 cps. There was no appreciable change in the amplitude or shape of the frequency spectrum as the power level was increased from 20 to 62.5 MWt. At power levels below 20 MWt, there were some changes in the spectrum, but these are attributed to system noise directly associated with low-power operation. This noise originates from induction heating, check valves, and cycling flow-control valves.

During operation at 62.5 MWt, performance of the steam-bypass system was tested. Bypassing of steam involves routing high-pressure steam through a pressure-reducing station and then directly (through a desuperheater) to the condenser without passing through the main turbine. Initial testing of the bypass system revealed that the large steam-bypass valve oscillated whenever the steam flow through the valve was about 140,000 lb/hr (56 MWt). Stable operation could be achieved at lower and higher steam flows. The valve manufacturer recommended that the range spring of the valve be changed. The change was made, after which additional steam-bypass tests were performed. Two transient tests were conducted with the reactor at 62.5 MWt:

(1) With the reactor at 62.5 MWt and the turbine on initial-pressure regulator, the incoming line breakers were tripped open.

(2) With the reactor at 62.5 MWt and the turbine on initial-pressure regulator, the turbine was tripped off.

The first test demonstrated satisfactory operation of the turbine autotransfer system. However, the steam-bypass valve did not open fast enough to avert high steam pressure and subsequent lifting of the Pressurmatic relief valve. The steam-bypass valve was opened manually about 15 sec after the transient was initiated.

The second test demonstrated satisfactory operation of the condenser and cooling tower under maximum heat load; however, as in the first test, the steam-bypass valve failed to respond fast enough to avoid high steam pressure. The Pressurmatic relief valve again opened. The steam-bypass valve was opened manually.

These tests showed that the large steam-bypass valve successfully handled the plant steam generated up to 61 MWt. As power was increased to 62.5 MWt, the valve started oscillating, resulting in oscillations in steam-plant pressure. The small steam-bypass valve was closed, thereby increasing the flow through the large valve. The increased flow loaded the valve sufficiently to damp the oscillations.

After the 62.5-MWt run, the original range spring was reinstalled because the range of the new spring was too narrow for satisfactory

control operation. Because of the unsatisfactory performance of the steam-bypass system, operation of the system is being evaluated and will be corrected.

6. Reactor Analysis, Testing and Methods Development

Last Reported: ANL-7618, pp. 44-55 (Sept 1969).

a. Transient Response of Core-subassembly Outlet Thermocouples during Power Decreases (J. R. Karvinen)

Measurements of the transient responses of specific core-subassembly outlet thermocouples were made during routine rod-drop studies at 62.5 MWt. The twelve thermocouples used in the studies were those modified for the experiments with the shielded twisted-pair leads. In effect, the time elapsing between the reactivity drop and the time required for the thermocouple output to register 90% of the final equilibrium output defines a transfer function between reactivity and thermocouple response.

Figure I.E.1 shows the actual response data for five of the twelve thermocouples during a typical rod drop. Figure I.E.2 shows similar data for an inadvertent reactor trip from 62.5 MWt. In all cases the responses are characterized by a transport lag of approximately 0.5 sec and a typical temperature transient governed by the time constants of the individual thermocouples. If the total response time for a given thermocouple is defined as the time required for the response to achieve 90% of its final value, the typical total response time of the outlet thermocouples is approximately 2 sec. Of the 2 sec, approximately 0.5 sec consists of a transport lag. The remaining portion, 1.5 sec, is attributed to the time required for the response to reach 90% of the equilibrium value (essentially a time lapse equivalent to three thermal time constants). Estimates of transport lags and the basic time constants for eight thermocouples are summarized for both rod-drop and scram transients in Table I.E.2.

The results shown in Figs. I.E.1 and I.E.2 and in Table I.E.2 are significant. The relatively noise-free signals shown in the figures illustrate the high quality of thermocouple signals obtainable by the shielded twisted-pair modifications. (The 17.5-Hz noise apparent in the signals was directly caused by the measuring apparatus and has since been eliminated.)

b. The Effect of Phase Transformation in EBR-II Driver Fuel on Power Coefficient (J. K. Long)

As the power level of the reactor has been increased from 45 to 50 MWt in August 1968, and from 50 to 62.5 MWt in September 1969, the temperature of more and more of the fuel has been raised above the level (550°C) at which metallurgical transition to the gamma phase is initiated.

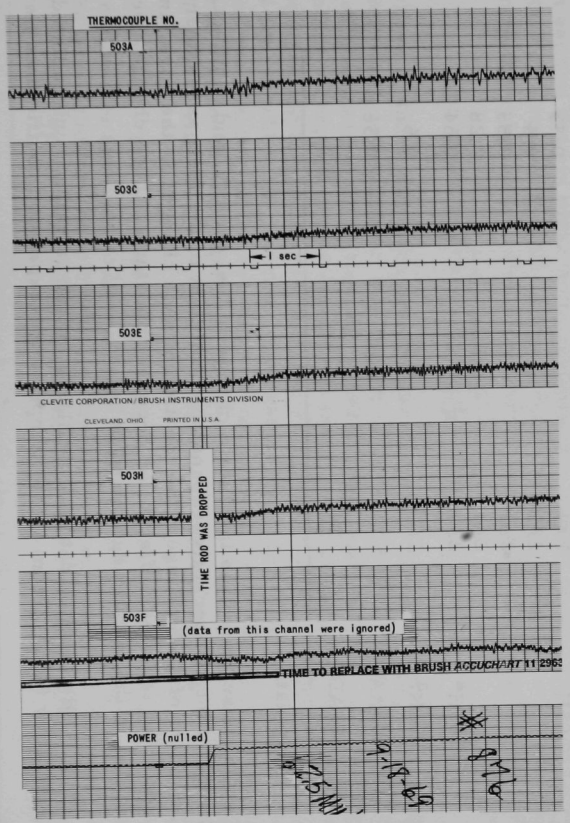

Fig. I.E.1. Responses of Core-subassembly Outlet Thermocouples during a Rod Drop from 62.5 MWt

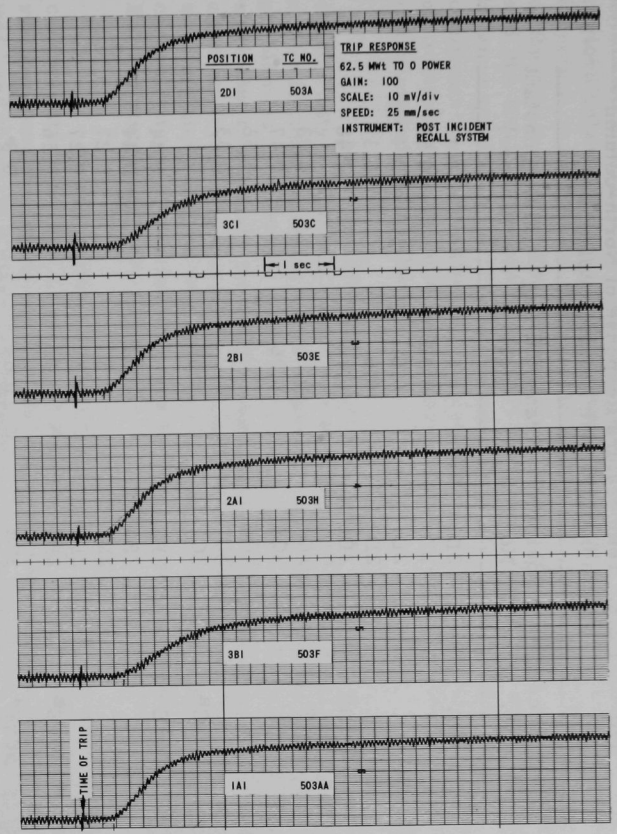

Fig. I.E.2. Responses of Core-subassembly Outlet Thermocouples Following a Reactor Trip from 62.5 MWt

TABLE I.E.2. Temperature Response of North-column Subassembly Outlet Thermocouples

Thermocouple No.	Position No.	Transport Lag (sec)	Time Constant (sec)
503A	2D1	0.6	0.47
	2D1	0.58	0.53
	2D1	0.6	0.4
	2D1	0.6	0.37
503A[a]	2D1	0.46	0.48
503C	3C1	0.6	0.93
	3C1	0.96	0.47
	3C1	0.82	0.56
	3C1	1.0	0.33
503C[a]	3C1	0.64	0.6
503E	2B1	0.68	0.44
	2B1	0.62	0.44
	2B1	0.6	0.27
	2B1	0.7	0.27
503E[a]	2B1	0.42	0.56
503F[a]	3B1	0.64	0.8
503H	2A1	0.4	0.33
	2A1	0.57	0.4
	2A1	0.6	0.33
	2A1	0.8	0.28
503H[a]	2A1	0.46	0.64
503K[a]	2F1	0.5	0.6
503AA[a]	1A1	0.46	0.56
503AD[a]	7D4	2.25	≈ 5

[a]Trip data.

Since the phase transition involves a change in fuel density, and in effect, a change in the temperature-expansion coefficient of the fuel, assessment of the extent of such changes, the location of such changes in the core, and the resulting reactivity effects has become important. These changes were calculated in the manner described below.

Dilatometer data are available for unrestrained, unirradiated fissium-alloy fuel.* From these, temperature-expansion coefficients were

* Zegler, S. T., and Nevitt, M. V., Structures and Properties of Uranium-Fissium Alloys, ANL-6116 (1961).

estimated to be 23 x 10^{-6} and 56 x 10^{-6} $\Delta L/L$ per °C, respectively, for the regions below and above 550°C. Fuel temperatures were estimated for 21 points on each of six fuel elements, one fuel pin representing each row of the reactor core. The temperatures of fuel-pin surfaces were calculated with the HECTIC program, which is based essentially on a multiregion heat balance applied to the flowing sodium, using appropriate heat-transfer coefficients. Computation of the temperatures within the fuel pin required estimation of the thermal conductivity, which in turn is a function of the radiation-induced swelling.

Since the internal fuel temperatures depend on the thermal conductivity, which is a function of swelling, and since swelling depends on the irradiation temperature, a precise solution of the temperature problem is an iterative process. For simplicity, it was regarded as sufficient to estimate the irradiation temperature from the nominal thermal conductivity, and to use this to estimate the swelling at each point. The swelling thus obtained was used to estimate a more appropriate thermal conductivity at each point, and thus to recalculate the temperature once. Further iterations were neglected.

An approximate temperature computed with the nominal thermal conductivity (0.3425 W/cm-°C) was applied to O'Boyle's data* to obtain the swelling, and then di Novi's correlation of swelling and thermal conductivity** was used to obtain a more appropriate thermal conductivity at the 21 points in each of the six pins. Uniform burnup of 0.0065 at. %, representing the start of a run, was used. Internal temperatures at each point were calculated from the relation (see Progress Report for April 1968, ANL-7445, pp. 47-48)

$$t(r) = \left(-a + \sqrt{a^2 + 1/2\, q'''(r_p^2 - r^2)\, b} \right) \Big/ b,$$

where a and b are parameters describing the linear variation of conductivity with temperature; $k = a + bt$; r_p is the outside radius of the pin; r is the variable radius; q''' is the heat generation per unit volume, assumed to follow a chopped cosine function in the axial direction; t(r) is the difference between the temperatures at r and at r_p. With t(r) computed, the radius, if any, at which the internal temperature exceeded 550°C was determined, and the fraction of the cross-sectional area in the region of high expansion then was found. As expected, the isothermal surface at 550°C was found to be shaped roughly like a cone with its apex oriented downward.

The effective temperature-expansion coefficient at each cross section was assumed to be the larger expansion coefficient multiplied by the area fraction above 550°C plus the smaller expansion coefficient multiplied by the remaining area fraction. The result multiplied by the

*Internal communication, D. R. O'Boyle to R. J. Dunworth (April 6, 1967).

**Internal communication, Roberta di Novi to J. H. Kittel (Feb. 12, 1968).

average temperature change at that cross section resulting from a 1-MWt power change yields the fuel component of the power coefficient.

The worth (W) of the expansion per MWt for all the intervals in a pin was computed from

$$W = \sum_j V_j \phi_j^* \phi_j - \phi_E^* \phi_E \sum_j V_j,$$

where V_j, ϕ, and ϕ_j^* are, respectively, the expansion, flux, and adjoint at the j'th interval, and ϕ_E and ϕ_E^* are the flux and adjoint at the edge of the core. This relation is equivalent to the assumption that fuel expansion removes material from positions along the length of the pin and replaces an equal amount at the end. Changes in the diffusion coefficient of the fuel were neglected. The fluxes and adjoints for the central plane were taken from a 22-group MACH-1 calculation collapsed to one group weighted by the group fission cross sections, and were given a chopped cosine shape in the axial direction. The W's thus obtained are relative rather than absolute values, so the calculation was made in two ways: with the normal low-temperature expansion coefficient throughout, and with the two-phase thermal-expansion coefficients. The normal value has been independently calculated to be about 0.7 Ih/MWt, and this normalization was used to obtain the worth of the fuel expansion in the two-phase case by comparison of the W's. Of this 0.7 Ih/MWt, about 0.58 is due to the change in length of the fuel and to the corresponding reduction in density of the fuel, and about 0.12 is due to replacement of sodium resulting from radial expansion of the pins.

The calculated results indicate that at 62.5 MWt the fuel component of the power coefficient may be 70% larger under the conditions of the problem than if the same temperatures were reached with the lower expansion coefficient in effect. Almost half of the fuel is predicted to be above 550°C at 62.5 MWt.

Since the fuel component amounts to about 40% of the total power coefficient, one would expect the slope of the PRD curve at 62.5 MWt to be about 28% greater than at 45 MWt. Actually, the Run-38 data indicate that it is only about 19% greater. Inaccuracies in estimating the expansion coefficient in the different ranges may account for some of this discrepancy. It also is possible, however, that the cone-shaped γ-phase region in each pin is somewhat constrained by the shell of α phase surrounding it, and thus the expansion is not as extensive as the unconstrained dilatometer results indicate. It is further possible that bowing effects could make a contribution which obscures the predicted increased expansion effect.

c. Rod-drop Studies (I. A. Engen)

To evaluate the effects of fuel burnup on reactivity feedback, rod-drop experiments were conducted at the beginning and end of Run 37

(total run length, 1200 MWd). All measurements were made with the modified drop rod described in the June 1969 Progress Report, ANL-7581, pp. 36-38.

Rod-calibration studies conducted at 500 kW at the beginning and the end of Run 37 established respective values of $0.02151 and $0.02149 for the worth of the drop rod. The results substantiate those derived from similar studies conducted during Runs 35 and 36; for these runs, too, no significant change in the worth of the drop rod was noted during the run.

Using the calibrated values for rod worth, the feedback functions established from data taken during the rod-drop experiments were fitted to a time-dependent feedback model in the manner described by Hyndman and Nicholson.* Figure I.E.3 shows the fit of data taken at the beginning of Run 37 to the model, along with values established for time constants, feedback amplitudes, and the transport delay time. In the model, positive terms correspond to negative feedback, and negative terms correspond to positive feedback.

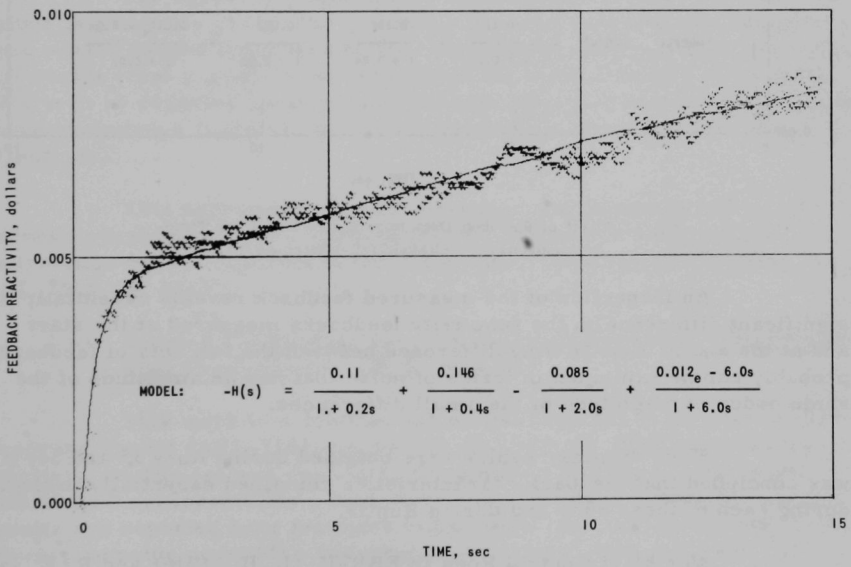

Fig. I.E.3. Fit of Rod-drop Data from Beginning of Run 37 to Time-dependent Feedback Model (50-MWt power; 100% flow)

*Hyndman, R. W., and Nicholson, R. B., The EBR-II Feedback Function, ANL-7476 (July 1968).

The mathematical model established at the beginning of Run 37 was shown to be in essential agreement with data taken at the end of the run. A slight improvement in fit, however, was obtained by reducing the amplitude of the 0.4-sec prompt term by about 4%. Figure I.E.4 shows the fit of the experimental data for the end of Run 37 to the revised model.

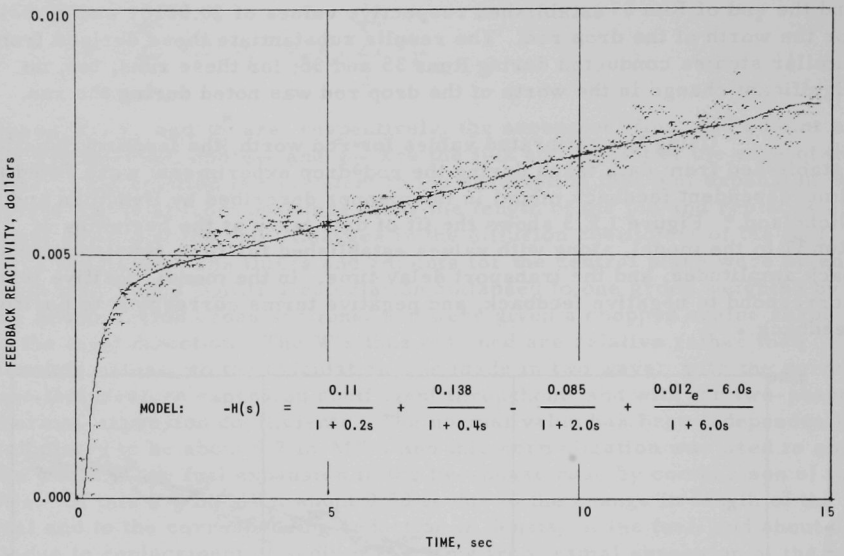

Fig. I.E.4. Fit of Rod-drop Data from End of Run 37 to Time-dependent Feedback Model (50-MWt power; 100% flow)

An inspection of the measured feedback reveals essentially no significant difference in the reactivity feedbacks measured at the start and at the end of Run 37. Any difference between the two sets of feedback probably can be explained in terms of noise that has an amplitude of the same order of magnitude of the small differences.

Since similar results were obtained during Runs 35 and 36, it was concluded that feedback characteristics remained essentially unchanged during each of these runs and during Run 37.

d. Worths of Control Rods in EBR-II (L. B. Miller and R. E. Jarka)

DSN (S_2) calculations of the control-rod worths in Run 32B have been completed. The worths were determined by successive k calculations in (x,y) geometry using the DOT5 code. Cross-section set 23806 was used with the usual 42 x 42 mesh, providing four mesh points per subassembly in the first ten rows of the core and blanket.

The computed and measured values are given in Table I.E.3. The computed values in %δk were converted to Ih using 1%δk = 430 Ih. A correction factor of 0.88 was applied to the computed numbers to account for the fact that the control rods are withdrawn into the axial blanket and are not totally removed from the system as is required for the (x,y) calculations.

TABLE I.E.3. Control-rod Worths in Run 32B

Control-rod Position	k_{ex} (Ih)		Control-rod Position	k_{ex} (Ih)	
	Theoretical	Experimental		Theoretical	Experimental
5A1	142	142	5D3	167	167
5A3	167	167	5E1	143	139
5B1	156	159	5E3	153	155
5B3	159	165	6E1	148	141
5C1	137	136	6E3	166	169
5C3	145	150			

The agreement between the theoretical and experimental values is generally good. The difference between the computed and measured worths ranges from zero to 5%. In all cases except one, the theoretical rod worths show a smaller deviation from the mean than was measured. This is to be expected because local perturbations are underestimated in any calculation with a finite number of discrete space points and discrete directions.

This agreement between measured and computed rod worths serves to corroborate the computed flux tilt and asymmetric power-distribution curves reported in the September 1969 Progress Report, ANL-7618, pp. 54-55.

e. Doppler Coefficients for EBR-II Configurations in Which Oxide Fuel Predominates (B. R. Sehgal)

This work is a continuation of that reported in the March 1969 Progress Report (ANL-7561, pp. 46-48), in which the Doppler shutdown reactivity coefficient was calculated for a proposed EBR-II oxide core with 47 BeO subassemblies. This study has since been continued, and results are reported here for three more oxide-core configurations: (1) a one-region oxide core; (2) a two-region oxide core* with different ^{235}U enrichments in the two regions optimized to give a minimum value for the radial maximum-to-average power ratio; and (3) a one-region oxide core with 24 BeO subassemblies. Table I.E.4 gives the specifications for these

*Golden, G. H., and Sehgal, B. R., Thermal-Hydraulic and Doppler Characteristics of Some Oxide Cores for EBR-II (to be presented at the 1969 Winter Meeting of Am. Nucl. Soc.).

three cores and for one on which the earlier calibration was based. Each of these cores is assumed to be contained in a radial reflector and a radial blanket. The geometry of the calculations is a one-dimensional cylinder with an extrapolated height of 64.4 cm.

TABLE I.E.4. Results of Calculations of Doppler Coefficients

Fuel: 20 wt % mixed PuO_2-UO_2 with 20 wt % ^{240}Pu in Pu
Radial Reflector: 27 cm thick; 13 vol % stainless steel; 23 vol % sodium, and 58 vol % nickel
Radial Blanket: 22 cm thick; 18 vol % stainless steel; 13 vol % sodium, and 59 vol % nickel
Geometry: Cylinder
Extrapolated Height: 64.4 cm

Core Configuration	Core Volume Fractions (%)				Equivalent Core Radius (cm)	Critical ^{235}U Enrichment (%)	Core Median Flux Energy (keV)	Doppler Coefficient ($T\partial k/\partial T$) at 700 to 1500°K
	Fuel	SS	Na	BeO				
1-region oxide	32.44	40.04	22.06	0.0	29.73	54.4	395	-0.00029
2-region oxide, with minimum ratio of max to avg power	31.58	40.55	21.97	0.0	29.70	45.4/68.1	397	-0.00023
1-region oxide with 24 BeO subassemblies	25.64	28.38	18.23	16.69	33.42	43.9	239	-0.00164
1-region oxide with 47 BeO subassemblies	22.39	25.71	18.73	29.60	35.12	33.1	155	-0.00491

Two sets of broad-group cross sections for each of these cores were derived with the MC^2 code* in homogeneous geometry at critical B^2, using the ENDF/B data** and the resonance isotopes at 700 and at 1500°K. Cross sections for the nickel-sodium reflector and for the depleted-uranium blanket were similarly calculated, but at 300°K and $B^2 = 0.0\ cm^{-2}$.

The SNARG-1D code† was used to calculate the critical ^{235}U enrichment at 700°K and subsequently the k_{eff} at 1500°K by changing to the 1500°K cross sections. The Doppler coefficients ($T\partial k/\partial T$) were calculated from the Δk's obtained, using the assumption that the Doppler coefficient was constant over the range from 700 to 1500°K.††

The results of the calculations are shown in Table I.E.4, along with the values of the core median flux energies to indicate the relative hardness of the spectra. In comparison, the core median flux energy for the present loadings of EBR-II is ≈ 406 keV.‡

*Toppel, B. J., Rago, A. L., and O'Shea, D. M., MC^2, A Code to Calculate Multigroup Cross Sections, ANL-7318 (1967).

**Honeck, H. C., ENDF/B, Specifications for an Evaluated Nuclear Data File for Reactor Applications, BNL-50066 (1966).

†Duffy, G. J., et al., SNARG-1D, A One-dimensional Discrete-ordinate Transport-theory Program for the CDC-3600, ANL-7221 (1966).

††Froelich, R., and Ott, K., "Results of Doppler Coefficient Calculations for Fast Reactors and Comparison of Different Methods," in Proceedings of the Conference on Safety Fuels, and Core Design in Large Fast Power Reactors, October 11-14, 1965, ANL-7120, p. 440.

‡Madell, J. T., and Jarka, R. E., Preliminary Investigation of the Neutronic Characteristics of a Mixed-oxide Fuel Loading of EBR-II, Trans. Am. Nucl. Soc. 12(1), 184 (1969).

The present calculations neglect cell heterogeneity in calculating the broad-group cross sections. However, recent results* indicate that for the 0.188-in. rods in these cores, this neglect may be a reasonable approximation. There may be errors in the ENDF/B ^{238}U cross sections between 1 and 10 keV because recent studies** have shown substantial differences between ENDF/B calculated and measured Doppler coefficients.

Table I.E.4 shows that cores with no BeO give a very small Doppler coefficient, and that a very substantial spectral softening and increase of Doppler coefficient occurs as BeO is added. Potentially, it is possible to get a relatively large Doppler shutdown reactivity; this may not be desirable, however, for the role of EBR-II as a test reactor. The core with 24 BeO subassemblies, which gives a Doppler coefficient of ~-0.0016, may be a compromise between spectral requirements and possible safety requirements.†

f. Structural-subassembly Spectral Calculations Using Spatially Independent Averaging for Group Constants (D. Meneghetti and K. E. Phillips)

Fine-group fluxes and currents in the energy range of resonance scattering at various positions in a steel-rich and in a nickel-rich structural subassembly in an EBR-II-type core were given in the Progress Reports for August 1969 (ANL-7606, p. 60) and for September 1969 (ANL-7618, pp. 49-51).

The fine spatially dependent solutions have been used to collapse the fine cross sections to obtain a separate cross-section set for each 63-mesh interval, 15 of which are in the structural region.

For comparison, the analogous cases were calculated using spatially independent collapsed cross sections. Two approaches were used. In the first, the structural-region coarse-group cross sections were obtained by weighting with the fine-group flux spectrum corresponding to the fundamental-mode solution for the EBR-II core composition. In the second approach, the structural-region coarse-group cross sections were obtained by weighting the fine-group flux spectrum corresponding to an infinite region (i.e., zero buckling) of structural composition in which a uniform fine-group fission-spectrum source is applied.

---

*Adkins, C. R., Murley, T. E., and Dyos, M. W., A Detailed Method for Calculating the Low Energy Multigroup Cross Sections and the Doppler Coefficient in a Fast Reactor, Nucl. Sci. Eng. 36, 336 (1969).

**Pond, R. B., and Till, C. E., Doppler Effect Studies as a Function of Reactor Spectra, Trans. Am. Nucl. Soc. 12(1), 272 (1969).

†Campise, A. V., Transient Analysis of EBR-II with a Predominantly Oxide-fueled Loading (to be presented at the 1969 Winter Meeting of Am. Nucl. Soc.).

The calculated central fluxes in the steel-rich and the nickel-rich subassemblies are shown in Tables I.E.5 and I.E.6, respectively. The simpler, spatially independent methods of cross-section weighting result in sizable errors, especially at the lower energies.

TABLE I.E.5. Flux in Steel-rich Central Subassembly[a]

Energy Group	Lethargy at Group Bottom	Fine-group Sum	Ratio of Results of Coarse-group to Fine-group Calculations		
			63 Sets[b]	F.M.[c]	$B^2 = 0$[d]
4	2.5	0.00249	1.00	1.00	0.98
5	3.0	0.00371	1.00	0.99	0.99
6	3.5	0.00379	1.00	1.02	0.98
7	4.0	0.00260	0.99	0.98	1.05
8	4.5	0.00189	0.98	1.05	1.01
9	5.0	0.00110	0.97	1.03	1.03
10	5.5	0.000613	0.99	0.97	1.04
11	6.0	0.000240	0.99	1.11	1.08
12	6.5	0.000148	0.99	0.90	1.14
13	7.0	0.000043	0.99	1.11	1.19
14	7.5	0.000012	0.99	1.17	1.50
15	8.5	0.000011	0.99	0.74	1.32

[a]Normalized to applied source of unity per centimeter of system height.
[b]Fifteen cross-section sets used in central-subassembly region; remaining sets used in core and blanket regions.
[c]Core fundamental-mode weighting of cross sections for central subassembly.
[d]Zero-buckling weighting of cross sections for central-subassembly region.

TABLE I.E.6. Flux in Nickel-rich Central Subassembly[a]

Energy Group	Lethargy at Group Bottom	Fine-group Sum	Ratio of Results of Coarse-group to Fine-group Calculations		
			63 Sets[b]	F.M.[c]	$B^2 = 0$[d]
4	2.5	0.00254	1.00	1.01	0.95
5	3.0	0.00360	1.00	0.98	1.02
6	3.5	0.00365	1.03	0.99	1.01
7	4.0	0.00277	1.01	1.02	0.97
8	4.5	0.00195	0.98	0.99	1.03
9	5.0	0.00111	0.97	0.91	1.10
10	5.5	0.000683	0.94	1.34	1.06
11	6.0	0.000284	0.95	1.08	1.02
12	6.5	0.000115	0.96	1.23	1.12
13	7.0	0.000133	0.96	2.92	0.96
14	7.5	0.000090	0.96	0.93	1.09
15	8.5	0.000048	0.97	1.17	1.25

[a]Normalized to applied source of unity per centimeter of system height.
[b]Fifteen cross-section sets used in central-subassembly region; remaining sets used in core and blanket regions.
[c]Core fundamental-mode weighting of cross sections for central subassembly.
[d]Zero-buckling weighting of cross sections for central-subassembly region.

g. Bowing Calculations (D. Mohr)

A check of the BOW-V calculations was made for EBR-II Run 25. The following quantities and/or relationships were calculated by hand and compared with BOW-V printed output for each row of subassemblies: (a) unrestrained thermal deflection, (b) relationship between bending loads and centerline deflection; and (c) relationship between compression loads and button compression.

Excellent agreement was noted in (a) and (b). However, a few apparent unbalances in loads (for a given compression) were found in (c), the highest percentage deviation from equilibrium being about 13% (or 3.3 lb/button).

Two new cases have been run with BOW-V, using the following reflector-blanket configurations: (a) a blanket consisting entirely of depleted uranium (corresponding approximately to Run 33); and (b) nickel reflector in Rows 7-10, and depleted uranium in Rows 11-15.

Bowing deflections were calculated for 20 power levels in the range from 0 to 125 MWt. For the first configuration, the results show some inward bowing (31.3 mils for Row 6 at 62.5 MWt and 82.1 mils at 125 MWt). For the other configuration, however, the results show essentially no inward bowing (0 mil for Row 6 at 62.5 MWt and <1 mil at 125 MWt).

The lack of inward bowing for the nickel reflector is caused primarily by the low temperature differentials in the hexagonal cans in Row 7 (e.g., maximum of 11°F ΔT at 62.5 MWt). The effects of reflector-subassembly stiffness and button stiffness are not important if the predicted hexagonal-can temperature differentials for Row 7 are valid. Thus, the above preliminary results should be equally valid for other potential nickel-stainless steel reflector configurations being considered.

h. Mechanical Analysis of IHX Nozzle (Lu Kang Chang)

An analysis of stress and buckling of the nozzle of the EBR-II intermediate heat exchanger (IHX) was made, in which the nozzle was assumed to be an infinitely long cylinder that is unrestrained longitudinally and restrained laterally at the welding edge. Donnell's nonlinear elastic theory of shells was used to derive the equations of equilibrium and natural boundary conditions. The deformations in the prebuckling state were considered to be axisymmetrical. The prebuckling stresses and deformation were obtained by solving the coupled equations of equilibrium and compatibility. Both simply supported and clamped boundary conditions were considered in the study. The possibility of buckling due to thermal loading also was considered.

The analysis indicates that the nozzle retains its mechanical stability within the range of thermal loadings to which it was subjected in this study.

i. Flow Calculations for High-temperature Reactor Experiments.

Calculations were made to determine the feasibility of raising the temperature of flowing sodium by using gamma heating within a stainless steel susceptor. The susceptor would be placed in Row 7 of EBR-II, and the hot sodium would be used in a study of resistance of various reactor materials to the flow of high-temperature sodium. The sodium inlet temperature was assumed to be 700°F, and the mass flowrate was set to provide a temperature of 1250° for the sodium within the susceptor.

The results of the calculations indicate that the sodium outlet temperature will be at a maximum of about 1256°F when the sodium flowrate is 147 lb/hr (0.36 gpm). For reasons explained below, the maximum temperature will not be at the sodium outlet; rather, it will be approximately 13 in. from the outlet, or 7 in. above the core.

The "Guide for Irradiation Experiments in EBR-II" was used to determine the rate of energy deposition within the susceptor: approximately 26,500 Btu/hr (7.76 kW). A portion of this energy is lost, however, by radiant heat transfer from the outer wall of the susceptor and by conduction across the inert-gas insulator. Initial calculations, in fact, showed that the heat losses due to these two mechanisms in the upper portion of the susceptor would be considerably greater than the heat deposited because of gamma interactions. These losses would be great enough to prevent the system from reaching and maintaining temperatures near the desired maximum under reasonable sodium flows. It appears, therefore, that the outer surface of the upper portion of the susceptor should be plated with gold to reduce these heat losses. It has been calculated that gold plating would decrease the rate of heat loss to about 2500 Btu/hr (0.73 kW), which represents a decrease of approximately 50%. The remaining 24,000 Btu/hr would be available to heat the sodium. Even after gold plating, however, the heat losses are still greater than the heat gains over approximately the upper 13 in. of the susceptor, which leads to the aforementioned conclusion that the sodium temperature will decrease along this portion of the susceptor to an outlet temperature of about 1244°F.

It is worthwhile to compare these results to those of a similar experiment done in mid-1968. This experiment, in which a nickel susceptor and a sodium flowrate of 1.2 gpm (509 lb/hr) were used, yielded a temperature rise of 240°F. The rate of heat transmission into the sodium was thus about 36,600 Btu/hr. Making estimates of the heat losses at the surface of that nickel susceptor and comparing the two systems under the same assumptions lead to the conclusion that the power deposition is about 0.431 W/g in nickel and about 0.433 W/g in stainless steel. Thus, the power

depositions appear to agree within about 3%. This agreement should be taken only as an indication that the results presented above are reasonably comparable with those obtained in the previous experiment and should by no means be interpreted as an estimate of the accuracy of the calculations.

7. Driver Fuel Development (C. M. Walter)

a. Fuel and Cladding Surveillance

Last Reported: ANL-7618, pp. 57-61 (Sept 1969).

(i) Preliminary BEMOD Calculations for a Row-7 Blanket Fuel Pin (J. F. Koenig, C. C. Ford, and C. M. Walter)

The BEMOD computer program was used to help determine the characteristics of a blanket element in Row 7 during irradiation to a burnup of 0.27 at. % (max).

Table I.E.7 gives the characteristics of the unirradiated blanket fuel pin. Since the gas volume is less than the sodium volume, there is a possibility of obtaining a high plenum pressure if there is sufficient fuel swelling. The 55-in. length of the fuel pin was divided into 35 axial nodes to obtain a satisfactory representation of the behavior of the elements. The expansion coefficient and thermal conductivity of the blanket fuel were assumed equal to those of the pure uranium metal. The thermal conductivity was reduced as fuel swelling occurred. It also was assumed that no fission gas was released from the fuel.

TABLE I.E.7. Characteristics of Unirradiated Blanket Fuel Pin

Fuel	
Diameter, in.	0.433
Length, in.	55
Volume, in.^{3}	8.09
Cladding	
Outside diameter, in.	0.493
Inside diameter, in.	0.457
Wall thickness, in.	0.016
Length, in.	$61\frac{31}{64}$
Net volume, in.^{3}	9.99
Bond Sodium	
Volume in annulus between fuel and cladding, in.^{3}	0.922
Volume above fuel (1.2-in. level), in.^{3}	0.145
Gas	
Volume, in.^{3}	0.579

The fuel-swelling characteristics of the blanket fuel are not known; however, swelling studies have been made at PNL* on fuel of similar composition. The PNL data for unrestrained swelling from these studies were used for the blanket-fuel swelling model. It was then assumed that a pressure of 1000 psi would reduce the swelling to 1/5 of its unrestrained value at the temperature at which fuel swelling is maximum (995°F). At a temperature of ±100°F from the maximum, the swelling was assumed to be reduced to half of the unrestrained value for a pressure of 1000 psi. The following equation was used to represent the fraction volume swelling of the fuel ($\Delta V/V$):

$$\Delta V/V = \%\ \text{burnup}\ [1.2\ \exp(-1.21 \times 10^{-4}\ \Delta T^2)]/[1 + (P/250)(1\ 0.75\Delta T^2/10^4)], \quad (1)$$

where P is the applied pressure in psi and ΔT is the difference between 995°F and the average fuel temperature in °F.

The calculations were made for the hottest element, next to the core, in a subassembly in position 7N4. Based on fission-rate distribution, the average heat rating was estimated as 5700 Btu/hr-ft, and the maximum heat rating was 3.2 times this value. For a subassembly flow-rate of 22 gpm, the rise in coolant temperature in the hot element was 191°F.

The blanket heat generation can vary significantly with the nature of the adjacent subassemblies. For example, Miller** at ANL has calculated that the heat generation may be increased by 50% if the blanket subassembly is adjacent to an oxide subassembly in Row 7. Therefore, the BEMOD calculations also were made at a heat rating of 8700 Btu/hr-ft.

BEMOD calculates the creep deformation of the cladding based on gas pressure or fuel-cladding contact pressure. It also calculates cladding swelling due to neutron fluence. Cladding swelling is described by†

$$\%\ \Delta V/V = 4.9 \times 10^{-49}\ (\text{nvt})^{1.71}\ \left(10^{1.55 \times 10^4/T - 5.99 \times 10^6/T^2}\right), \quad (2)$$

where T is the temperature in °K and $\%\ \Delta V/V$ is the percent volume increase.

The buildup of gas pressure in the blanket element was found to be negligible. The change in cladding diameter ($\Delta D/D$) was found to be due entirely to neutron-fluence swelling and fuel-cladding contact pressure. The calculations indicate that fuel-cladding contact would occur at ~0.25 at. % burnup. The calculated fuel swelling and cladding strain at

*Leggett, R. D., et al., Basic Swelling Studies, BNWL-SA-154 (Sept 1965).

**Miller, L. B., private communication.

†Claudson, T., PNL, private communication.

0.27 at. % maximum burnup qualitatively agreed with measurements made of blanket elements having the same burnup. Increasing the power rating increased the length of the fuel-cladding contact area. Calculations were continued to the point where the increase in cladding diameter ($\Delta D/D$) was 2%. This occurred at 0.57 at. % burnup for a heat rating of 5700 Btu/hr-ft and at 0.51 at. % burnup for a heat rating of 8700 Btu/hr-ft. For 2% $\Delta D/D$, 80% of the $\Delta D/D$ is due to neutron fluence. The maximum $\Delta D/D$ for both heat ratings is shown as a function of burnup in Fig. I.E.5.

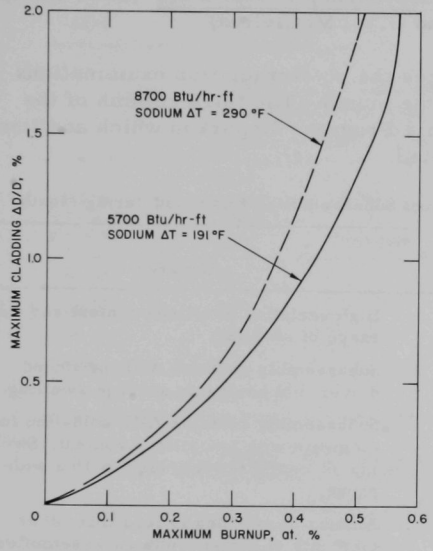

Fig. I.E.5. Calculated $\Delta D/D$ for EBR-II Row-7 Blanket Element

The gas pressure built up to 200 psi for the elements taken to 2% $\Delta D/D$, and the maximum fuel-cladding contact pressure was 1400 psi. The length of the gas plenum decreased from 2.3 in. initially to 0.6 in. at 2% $\Delta D/D$.

In summary, the magnitude of the calculated fuel swelling agrees well with the measured swelling. The location and length of the fuel-cladding contact area, however, are somewhat different. The maximum measured swelling occurs lower in the fuel element and over a greater length of fuel than calculated. These discrepancies are minor and may be due to the uncertainty in the heat rating and/or the maximum fuel swelling occurring at a lower temperature than the 995°F used in the model. The measured fuel swelling tended to be elliptical rather than circular, which may have been due to the external restraints or coolant-flow distribution on the fuel pins. Additional calculations will be carried out with a modified fuel-swelling model to obtain better agreement between the measured and calculated fuel swelling.

(ii) 70%-enriched Fuel Experiment (J. P. Bacca, A. K. Chakraborty, and G. C. McClellan)

Seventy-percent-enriched Subassembly C-2213S (reconstituted from previously irradiated Subassembly C-2193S at 1.55 at. % burnup) was irradiated during Run 38B and attained a calculated burnup peak of 1.78 at. %. Postirradiation examinations will be conducted after the shutdowns of EBR-II and the FCF air cell have been completed.

(iii) Controlled-flow Experiment (J. P. Bacca, A. K. Chakraborty, and G. C. McClellan)

Controlled-flow Subassembly C-2188S was installed in the core at the start of Run 38B and attained a calculated burnup peak of 1.77 at. %. Postirradiation examinations will be initiated after the shutdowns of the reactor and the FCF air cell have been completed.

(iv) Surveillance of Extended-burnup Driver Fuel (J. P. Bacca, A. K. Chakraborty, and G. C. McClellan)

Table I.E.8 summarizes the postirradiation examinations conducted under this program during the month. The third column of the table lists those additional tables of this Progress Report in which additional data for each subassembly are presented.

TABLE I.E.8. Extended-burnup Driver-fuel Subassemblies Examined during Month

Subassembly	Burnup (at. % max)	Table Providing More Data	Remarks
C-2073	1.74	I.E.9	High variation of silicon content and wide range of swelling.
C-2170	1.50	I.E.10	Subassembly contains ANL-produced driver fuel having an average swelling.
B-3036	1.52	I.E.11	Subassembly contains ANL cold-line fuel elements with low silicon content. Swelling is comparatively high, with a wide range.
B-3038	1.95	I.E.12	Amount of swelling is less than other elements of high-burnup subassemblies. Average value is only 8.1%; range is 5.9-10.5%.
B-3042	1.71	I.E.13	Consists of cold-line fuel elements. Batches with higher silicon content show less swelling than batches with lower silicon contents.
B-3046	1.75	I.E.14	Wide range of swelling, from 6.5 to 16.9%, could probably be attributed to the wide difference in silicon concentration.
B-3047	1.73	I.E.15	Low-swelling data were obtained.
B-3048	1.73	I.E.16	Average swelling comparable with other extended-burnup subassemblies.
B-387	1.73	I.E.17	Swelling data were slightly lower than the expected value.

TABLE I.E.9. Fabrication and Irradiation Data for Extended-burnup Driver-fuel Subassembly C-2073

(Calculated burnup: 1.75 at. % max; 1.46 at. % avg)

Injection-casting Batch No.	Silicon Content of Fuel (ppm)	Number of Elements	Element Burnup Range (at. %)	Total Volume Swelling of Fuel (ΔV/V) (%)	
				Average	Range
4212	260	14	1.66-1.73	12.09	9.1-15.0
4213	430	65	1.59-1.73	7.04	4.8-8.8
4214	340	12	1.59-1.69	6.77	5.7-8.1

TABLE I.E.10. Fabrication and Irradiation Data for Extended-burnup Driver-fuel Subassembly C-2170

(Calculated burnup: 1.501 at. % max; 1.340 at. % avg)

Injection-casting Batch No.	Silicon Content of Fuel (ppm)	Number of Elements	Element Burnup Range (at. %)	Total Volume Swelling of Fuel (ΔV/V) (%)	
				Average	Range
63 IH	369	1	1.387	7.31	-
64 IH	333	3	1.39-1.45	10.0	8.7-11.86
64 II	302	1	1.1	8.78	-
65 II	313	26	1.12-1.38	8.77	7.1-10.00
			Average for all elements	8.85	

TABLE I.E.11. Fabrication and Irradiation Data for Extended-burnup Driver-fuel Subassembly B-3036

(Calculated burnup: 1.522 at. % max; 1.21 at. % avg)

Injection-casting Batch No.	Silicon Content of Fuel (ppm)	Number of Elements	Element Burnup Range (at. %)	Total Volume Swelling of Fuel (ΔV/V) (%)	
				Average	Range
32 IH	90	2	1.30-1.46	16.0	15.0-17.0
33 IH	102	24	1.28-1.52	13.80	8.93-15.9
79 IH	251	5	1.22-1.365	5.71	4.45-7.44
			Average for all elements	12.64	

TABLE I.E.12. Fabrication and Irradiation Data for Extended-burnup Driver-fuel Subassembly B-3038

(Calculated burnup: 1.95 at. % max; 1.55 at. % avg)

Injection-casting Batch No.	Silicon Content of Fuel (ppm)	Number of Elements	Element Burnup Range (at. %)	Total Volume Swelling of Fuel (ΔV/V) (%)	
				Average	Range
074 IH	390	91	1.58-1.92	8.1	5.9-10.5

TABLE I.E.13. Fabrication and Irradiation Data for Extended-burnup Driver-fuel Subassembly B-3042

(Calculated burnup: 1.71 at. % max; 1.36 at. % avg)

Injection-casting Batch No.	Silicon Content of Fuel (ppm)	Number of Elements	Element Burnup Range (at. %)	Total Volume Swelling of Fuel (ΔV/V) (%)	
				Average	Range
88 II	320	12	1.47-1.72	11.05	8.0-15.75
89 IH	515	19	1.43-1.66	5.70	4.63-7.27
			Average for all elements	7.77	

TABLE I.E.14. Fabrication and Irradiation Data for Extended-burnup Driver-fuel Subassembly B-3046

(Calculated burnup: 1.75 at. % max; 1.39 at. % avg)

Injection-casting Batch No.	Silicon Content of Fuel (ppm)	Number of Elements	Element Burnup Range (at. %)	Total Volume Swelling of Fuel (ΔV/V) (%)	
				Average	Range
085 II	289	13	1.48-1.61	13.4	9.6-16.7
086 II	340	74	1.48-1.66	11.4	6.5-16.9
092 IH	429	2	1.64-1.66	8.1	8.0-8.2
			Average for all elements	11.6	

TABLE I.E.15. Fabrication and Irradiation Data for Extended-burnup Driver-fuel Subassembly B-3047

(Calculated burnup: 1.73 at. % max; 1.37 at. % avg)

Injection-casting Batch No.	Silicon Content of Fuel (ppm)	Number of Elements	Element Burnup Range (at. %)	Total Volume Swelling of Fuel (ΔV/V) (%)	
				Average	Range
086 II	414	11	1.59-1.70	8.43	7.44-9.42
087 II	341	20	1.41-1.60	8.69	6.1-13.8
			Average for all elements	8.6	

TABLE I.E.16. Fabrication and Irradiation Data for Extended-burnup Driver-fuel Subassembly B-3048

(Calculated burnup: 1.73 at. % max; 1.38 at. % avg)

Injection-casting Batch No.	Silicon Content of Fuel (ppm)	Number of Elements	Element Burnup Range (at. %)	Total Volume Swelling of Fuel (Δ V/V) (%)	
				Average	Range
087 II	341	13	1.46-1.69	12.82	8.98-16.30
088 II	320	16	1.40-1.72	11.68	6.16-15.34
092 IH	429	1	1.43	5.53	-
			Average for all elements	11.97	

TABLE I.E.17. Fabrication and Irradiation Data for Extended-burnup Driver-fuel Subassembly B-387

(Calculated burnup: 1.73 at. % max; 1.39 at. % avg)

Injection-casting Batch No.	Silicon Content of Fuel (ppm)	Number of Elements	Element Burnup Range (at. %)	Total Volume Swelling of Fuel (ΔV/V) (%)	
				Average	Range
9 IH	390	12	1.52-1.64	9.13	6.83-13.47
10 IH	390	15	1.50-1.60	8.40	6.48-10.87
11 IH	300	3	1.46-1.47	7.3	6.0-8.2
			Average for all elements	8.58	

8. Operation with Failed Fuel (R. R. Smith)

Last Reported: ANL-7618, pp. 62-69 (Sept 1969).

a. Defective Claddings on EBR-II Driver Fuel Elements (G. S. Brunson)

(i) Defect above Sodium Level. The fuel element selected for this experiment was pin No. 3, Batch 115 IH, which in the course of routine top-weld tests was found to have a defect equivalent to a cylindrical hole approximately 1/2 mil in diameter. During the bonding operation, the hole apparently became plugged with sodium or sodium oxide. The test specimen was assembled into a standard fuel subassembly and inserted in the core. At the end of Run 38B, the specimen had undergone the following irradiation history:

Run	Reactor Position	Dates (1969)	Exposure (MWd)	Peak Accumulated Burnup (at. %)
34B	3C1 Basket	May 14 May 28	310	0.10
37A	3F2 Basket	Aug. 2 Sept. 1	1196	0.49
38B	3B1 Basket	Oct. 1 Oct. 17	600	0.70

At the end of Run 38B, there was some evidence which suggested that release of fission products from the test specimen might have taken place. However, the evidence also could have arisen from one or more inadvertent defects in driver elements. Therefore, consideration is now being given to repeating the experiment with a fuel element that has a larger drilled defect in the region of the upper weld.

(ii) Defect below Sodium Bond and Fuel Level. A technique has been developed for producing a defective fuel element to serve as a test specimen for this experiment. The steps are as follows:

1. A slot 40 mils wide and 40 mils deep is machined across the top of a standard spade.

2. A 30-mil hole is drilled axially upward through the spade until a pimple becomes visible in the bottom of the slot.

3. A laser penetration of 1-3 mils in diameter is made at the center of the pimple.

4. The spade is then welded in the usual fashion to a standard jacket, and a leaktest is made to establish that the hole is still open.

5. The hole is then covered with a weld, and the jacket is retested to ensure that the leak has been sealed.

6. The experimental jacket is then loaded, welded, leak-tested, bonded, and bond-tested by the normal cold-line procedure.

7. As a last step before incorporating the test element in a fuel subassembly, the cover weld is drilled through.

This procedure has been followed with four elements to establish its feasibility. The results were entirely satisfactory in that leaks were produced and all elements survived bonding operations despite the fact that the 2000 impacts delivered resulted in substantial peening of the upper end of the spade. The 40-mil slot served to prevent closure of the leak from this cause.

b. Studies with Reactor Cover-gas Monitor (G. S. Brunson)

Information relating to recent tests with the reactor cover-gas monitor (RCGM) was presented in the Progress Report for August 1969, ANL-7606, pp. 63-66. Illustrations for much of the material presented in that report are given in the following.

Figure I.E.6 illustrates the equilibrium gamma spectrum "seen" by the RCGM. In one experiment, the gas sample volume was isolated and the activity allowed to decay. The spectra observed as a function of time are also shown. It is interesting to note that a peak identified as ^{23}Ne (not identified in Fig. I.E.6) disappears in a very few minutes.

Figure I.E.7 is the spectrum obtained from an 8-hr-old gas sample with a GeLi solid-state spectrometer. Because of the age of the sample, shorter-lived activities are missing. A comparable on-line spectrum would show lines for ^{23}Ne and for as many as six short-lived Xe and Kr isotopes.

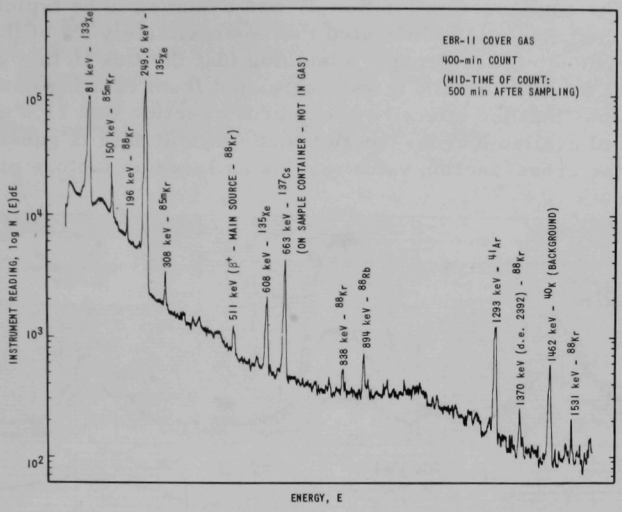

Fig. I.E.6. Equilibrium Gamma Spectrum "Seen" by Reactor Cover-gas Monitor

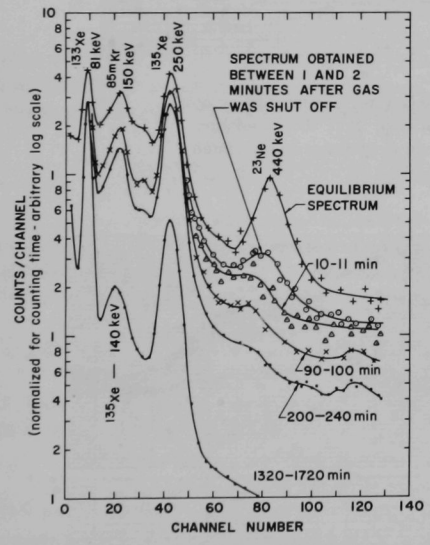

Fig. I.E.7. Spectrum of 8-hr-old Cover-gas Sample Measured with a GeLi Solid-state Detector

Figure I.E.8 illustrates the erratic nature of the RCGM response during a reactor startup. The plot represents reactor power at a ΔT of 28°F, which corresponds to approximately 10 MWt. At that point in the startup, the fission-product component in the cover-gas system is small, and the inventory of the relatively short-lived ^{23}Ne isotope is near saturation. Figure I.E.9 shows the results during stable 50-MWt operation. By varying the flowrate of the secondary sodium, the bulk sodium temperature was driven upward a few degrees on a mild ramp. Here again, the change in temperature apparently affects the release rate of ^{23}Ne, the effects of which are sensed in the ^{133}Xe and ^{135}Xe channels through a change in the Compton background.

Calculations have been performed in an effort to correlate the expected generation rate of ^{23}Ne with experimental results. ^{23}Ne is generated in the reaction $^{23}Na(n,p)^{23}Ne$ for neutrons having energies in excess of

≈4 MeV. The configuration for Run 27 was assumed to be typical. The results of the calculations indicated that approximately 3% of the flux fell in the uppermost energy group. Assuming that the flux in this group has the shape of the fission tail, it was calculated from existing data for neutron cross sections that the effective group cross section was 11.5 mb. Since the quality of available cross-section and spectral data is questionable, errors in the cross-section value may be as large as factors of 2-3.

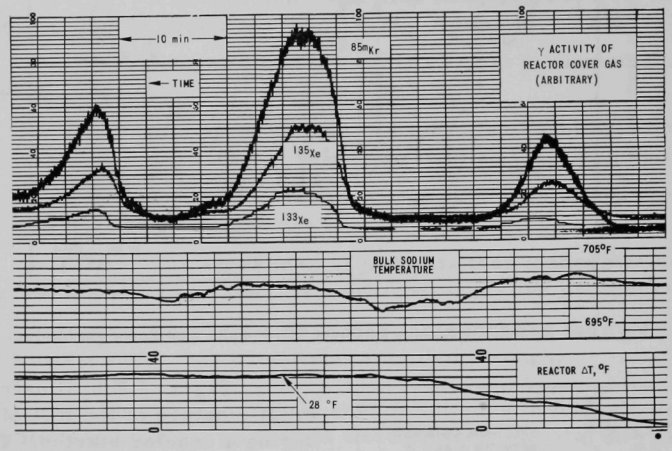

Fig. I.E.8. Response of Reactor Cover-gas Monitor during a Typical Reactor Startup. Note the correlation between bulk sodium temperature and indicated activity levels.

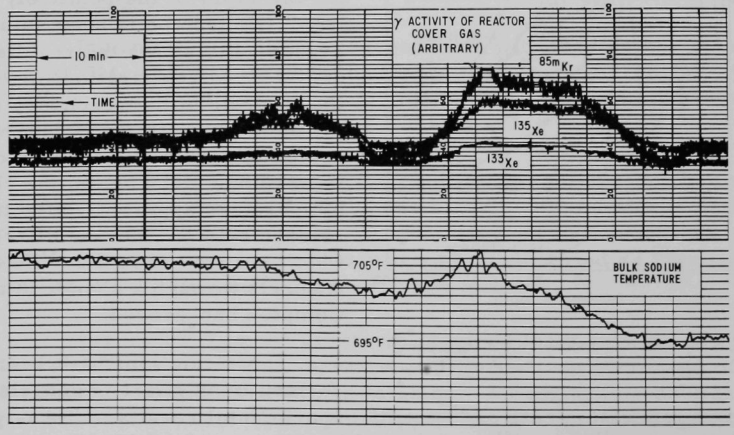

Fig. I.E.9. Response of Reactor Cover-gas Monitor at 50 MWt. Note the reduced sensitivities of cover-gas activities to variations in bulk sodi...

An effective core volume corresponding to 91 subassemblies was assumed. Such a core contains ≈45 liters of sodium weighing ≈38 kg at operating temperature. An average core flux of 2×10^{15} n/cm^2-sec (at 50 MWt) and a high energy flux of 6×10^{13} n/cm^2-sec also were assumed. The overall production rate of ^{23}Ne is thus

$$\underbrace{6 \times 10^{13}}_{\text{Flux } (\phi)} \times \underbrace{\frac{3.8 \times 10^{4}}{23} \times 6 \times 10^{23}}_{^{23}\text{Na Atoms (N)}} \times \underbrace{11.5 \times 10^{-27}}_{\text{Cross Section } (\sigma)} = 7 \times 10^{14} \ ^{23}\text{Na atoms/sec}$$

For comparison, the production rate of ^{135}Xe from tramp uranium is as follows, assuming 7 mg of ^{235}U as the effective tramp quantity and using 6% as the yield. At 50 MWt, there are $\approx 1.5 \times 10^{18}$ fissions/sec, of which

$$\frac{7 \times 10^{-3}}{2.3 \times 10^{5}} \times 1.5 \times 10^{18} = 4.5 \times 10^{10} \text{ fissions/sec}$$

occur in the tramp uranium, yielding

$$6 \times 10^{-2} \times 4.5 \times 10^{10} = 2.6 \times 10^{9} \text{ atoms/sec of } ^{135}\text{Xe}.$$

Since the ^{23}Ne production exceeds that of ^{135}Xe from tramp uranium by more than five orders of magnitude, it is not surprising that ^{23}Ne does interfere with monitoring ^{135}Xe and other noble gas fission products.

c. Studies with the Fuel Element Rupture Detector (G. S. Brunson)

The foregoing calculations suggest that other high-energy reactions, uncommon elsewhere, may be of importance in EBR-II. The calculated cross section for the reaction ^{23}Na(n,α)^{20}F is 5.4 mb. The production rate of ^{20}F per liter of sodium in the core is calculated as

$$6 \times 10^{13} \times (8.5 \times 10^{2}/23) \times 6 \times 10^{23} \times 5.4 \times 10^{-27} = 7.2 \times 10^{12} \text{ atoms/liter-sec.}$$

^{20}F has an 11-sec half-life, or $\lambda = 6 \times 10^{-2}$, and yields a 1.63-MeV gamma in 100% of its disintegrations.

Assuming that the transit time of sodium through the core is 1/10 sec and that two half-lives are required to reach the EBR-II fuel element rupture detector (FERD) system, the gamma-emission rate for ^{20}F in the FERD geometry would be

$$(1/10) \times 7.2 \times 10^{12} \times (1/4) \times 6 \times 10^{-2} = 1.1 \times 10^{10} \text{ dis/liter-sec.}$$

For comparison, the measured ^{24}Na 50-MWt equilibrium activity is 0.54 Ci/liter or

$$0.54 \times 3.7 \times 10^{10} = 2 \times 10^{10} \text{ dis/liter-sec},$$

and the yield is 100% for both 1.37- and 2.76-MeV gammas.

On the basis of energy and disintegration rate, the above estimates suggest that ^{20}F might contribute as much as 15% of the gamma activity in the FERD.

During Run 38B, a gamma chamber was located in place of one of the neutron counters in the FERD. Although analysis is not complete, there has been no sudden change in gamma intensity during startup and shutdown (or reactor trip) as would occur if the 11-sec ^{20}F were a substantial contributor. The inference is that the estimate for ^{20}F is in error, possibly through an error in the cross section. This does not rule out the possibility of other short-lived gamma emitters being in the sodium, which, however, may be of too low an energy to compete with the hard ^{24}Na gammas in penetrating the 2 in. of lead between the sodium pipe and the detector.

F. EBR-II Operations

1. Reactor Plant (G. E. Deegan)

Last Reported: ANL-7618, pp. 70-71 (Sept 1969).

Run 38A, the initial reactor run at 62.5 MWt, was completed on September 28 after 517 MWd at that power level. The reactor then was operated at 50 MWt for 600 MWd in Run 38B. The reactor was shut down on October 16 for an extended period of maintenance and for installation of the instrumented subassembly. The cumulative total of EBR-II operation is 30,040 MWd.

Operation at 62.5 MWt was satisfactory; however, a problem with the steam-bypass system was encountered while testing the system with full bypass flow. Improper response of the bypass valve caused oscillation of the steam-system flow. A review of the valve and its controller will be made, and remedial action will be taken.

At the beginning of Run 38B, rod-drop experiments with the stainless steel rod were performed at 500 kW, 50 MWt, and again at 500 kW. The results of the two 500-kW rod drops are being compared. Run 38B, which was concluded on October 16, was interrupted by two scrams.

Cooldown of the plant began on October 18, and the secondary system was dumped the following day. Shutdown activities have begun while cooldown to ambient is being completed.

The loading changes for Run 38B included the reinstallation or relocation of experimental and surveillance subassemblies which were removed or relocated for the 62.5-MWt operation during Run 38A. Five new or reconstituted experimental subassemblies also were loaded. The following additional changes were made for Run 38B:

Seven spent driver subassemblies and one depleted-uranium inner-blanket surveillance subassembly were replaced. The three previously irradiated Mark-II-fuel subassemblies were reinstalled in the grid, and three new Mark-II-fuel subassemblies also were installed. One reconstituted 70%-enriched subassembly was installed, and one controlled-flow subassembly and the upper-leaky-weld-test subassembly were reinstalled.

After Run 38B, experimental Subassembly XO65A was removed from the grid for transfer to the Fuel Cycle Facility. Three spent driver subassemblies were replaced by dummies to give increased shutdown margin during the long shutdown. Control rod No. 6 was removed from position 5F3, and the position was left vacant for installation of the instrumented subassembly.

2. Fuel Cycle Facility (M. J. Feldman)

Last Reported: ANL-7618, pp. 71-78 (Sept 1969).

a. Fuel

(i) Cold-line Production and Assembly. Operation of the cold line for the production of Mark-IA fuel elements continued. Table I.F.1 summarizes the production activities for September 16 through October 15, 1969, and for the year to date. Two Mark-IA subassemblies were fabricated in the cold line during the month.

(ii) Outside Fuel Procurement

(a) Impact Bonding of Unbonded Vendor Elements. ANL has impact bonded all the 2179 unbonded elements received from Aerojet-General Corp. (AGC). A total of 10,000 such elements will be so processed. Of the 2179 elements bonded, 1979 were accepted. The primary causes of rejection were voids (112 elements) and low sodium level (67 elements).

(b) Inspection of Vendor Fuel. An additional 225 AGC-fabricated elements were received this month, but were not inspected. The current number (as of October 15, 1969) of AGC elements available after verification inspection is 22,394. This figure does not include unbonded AGC elements that were impact bonded by ANL.

b. Surveillance (M. J. Feldman, J. P. Bacca, and E. R. Ebersole)

(i) Postirradiation Analysis of EBR-II Fuel (J. P. Bacca)

(a) Surveillance of Vendor-produced Fuel

(1) Fuel-characterization Studies. Listed below, together with the results of their postirradiation examination, are driver subassemblies that were irradiated as part of the program effort to characterize the performance of AGC fuel.

(A) Subassembly C-2211S (calculated burnup maximum, 0.39 at. %). This subassembly contained AGC centrifugally bonded elements which had been given a "corrective" heat treatment by ANL to remove preferred orientation (texture) in the fuel pins. The heat treatment consisted of a $1\frac{1}{2}$-hr holding period at 660°C, cooling to room temperature in air, then a 2-hr heat treatment at 500°C. One thousand impacts were administered to the fuel elements in the cold-line bonders of the Fuel Cycle Facility during the 500°C treatment. Postirradiation-examination results for elements from Subassembly C-2211S are summarized in Tables I.F.2 and I.F.3. As can be seen in Table I.F.2, the "corrective" heat treatment

TABLE I.F.1. Production Summary for FCF Cold Line

	9/16/69 through 10/15/69		Total This Year	
	Mark IA	Mark II	Mark IA	Mark II
Alloy-preparation runs				
New fuel	1	0	11	8
Remelts	3	0	15	3
Total	4	0	26	11
Injection-casting runs	8	0	36	10
Pins processed				
Accepted	728	0	3,496	941
Rejected	27	0	116	53
Elements welded	569	0	3,712	884
Elements rewelded	0	0	0	69[a]
Elements leaktested				
Accepted	809	0	3,534	804
Rejected	37	0	88	21
Elements bondtested				
Accepted	354	0	3,247	934
Rejected	17	0	336	9
Subassemblies fabricated (cold-line fuel)	2	0	31	6
Bonded elements received from vendor	225		24,313[b]	
Inspected and accepted	0		23,407[b,c]	
Inspected and rejected	0		1,240[b]	
Unbonded elements received from vendor	0		2,179[d]	
Impact-bonded, inspected, and accepted by ANL	1,111		1,979	
Impact-bonded, inspected, and rejected by ANL	117		190	
Subassemblies fabricated (vendor fuel)	4[e]		16[f]	
Total elements available for subassembly fabrication as of 10/15/69				
Cold-line fuel				
Mark IA	1,068			
Mark II	234			
Vendor fuel (Mark IA)	22,394[g]			

[a]Includes 64 elements in which visual examination of welds indicated that they were not acceptable for potentially high-burnup experiments.
[b]Total includes figures for 1968.
[c]Includes fuel elements returned to vendor for rework to correct voids in sodium bond and after rework sent back to ANL for reinspection.
[d]Ten unbonded vendor elements were set aside for historical samples.
[e]Each subassembly is made up of a mixture of nonbonded vendor elements that were subsequently impact bonded by ANL and of cold-line fuel elements.
[f]Includes subassemblies made up of a mixture of vendor and cold-line fuel elements.
[g]This figure does not include vendor elements that were impact bonded by ANL.

TABLE I.F.2. Postirradiation Lengths of Fuel Pins from Subassembly C-2211S

(Calculated burnup: 0.39 at. % max; 0.34 at. % avg)

AGC Fuel Pins

The following as-fabricated AGC fuel elements were subjected to an ANL remedial heat treatment consisting of holding at 660°C for 1-1/2 hr, cooling in air to room temperature, then heat treating at 500°C for 2 hr in the cold-line bonders, at which time the elements received 1000 impacts.

AGC Batch 200		AGC Batch 295		AGC Batch 399		AGC Batch 500		AGC Batch 575	
Element No.	Length (in.)	Element No.	Length (in.)	Element No.	Length (in.)	Element No.	Length (in.)	Element No.	Length (in.)
2	13.5	7	13.5	5	13.5	3	13.5	6	13.5
13	13.5	20	13.5	8	13.5	10	13.5	9	13.5
30	13.5	23	13.5	24	13.5	14	13.5	12	13.5
33	13.5	27	13.5	29	13.5	26	13.5	21	13.5
35	13.5	56	13.5	36	13.5	43	13.5	22	13.5
38	13.5	59	13.5	42	13.5	57	13.5	39	13.5
41	13.5	70	13.5	50	13.5	61	13.5	44	13.5
54	13.5	79	13.5	52	13.5	69	13.5	47	13.5
60	13.5	83	13.5	55	13.5	75	13.5	53	13.5
72	13.5	87	13.5	63	13.5	81	13.5	65	13.5
90	13.5			68	13.5	85	13.5	73	13.5
				74	13.5	91	13.5	84	13.5
				89	13.5			86	13.5

The following AGC as-fabricated elements received no postbonding remedial heat treatment.

AGC Batch 200		AGC Batch 295		AGC Batch 399		AGC Batch 500		AGC Batch 575	
Element No.	Length (in.)	Element No.	Length (in.)	Element No.	Length (in.)	Element No.	Length (in.)	Element No.	Length (in.)
17	13.2	15	13.0	16	13.1	4	13.1	11	13.1
40	13.1	28	13.1	37	12.9	25	13.2	31	13.1
46	13.2	45	13.0	62	13.0	58	13.1	48	13.0
80	13.0	78	13.0	76	13.4	82	13.0	66	13.1

ANL Cold-line Pins

The postirradiation length of each of the fuel pins in the 12 cold-line as-fabricated elements included in this subassembly was 13.5 in.

TABLE I.F.3. Fabrication and Irradiation Data for Subassembly C-2211S

(Calculated burnup: 0.39 at. % max; 0.34 at. % avg)

Injection-casting Batch No.	Silicon Content of Fuel (ppm)	Number of Elements	Element Burnup Range (at. %)	Total Volume Swelling of Fuel (ΔV/V, %)	
				Average	Range
AGC Fuel					
AG 200	450	15	0.36-0.39	1.3	0.1-2.0
AG 295	421	14	0.36-0.39	1.2	0.6-2.4
AG 399	400	17	0.36-0.39	1.2	0.8-1.9
AG 500	420	16	0.36-0.39	1.2	0.8-2.2
AG 575	500	17	0.36-0.39	1.1	0.2-2.3
ANL Cold-line Fuel					
147 I	475	12	0.36-0.39	1.8	1.3-3.5

apparently was effective in eliminating texture in the fuel. This was evidenced by the absence of pin shortening and radial growth during irradiation, at least to this burnup level. Irradiation swelling of the fuel, shown in Table I.F.3, is reasonably consistent with that observed for ANL-produced fuel.

(B) Subassembly C-2210 (calculated burnup maximum, 0.37 at. %). This subassembly contained fuel elements utilizing

ANL-cast pins which had been either impact bonded by ANL or centrifugally bonded by AGC. Postirradiation data for these elements are summarized in Tables I.F.4 and I.F.5. It can be observed in Table I.F.4 that the centrifugal bonding (as conducted by AGC) did introduce texture in the ANL fuel, such as is evidenced by the shortening of the centrifugally bonded elements during irradiation. This experiment essentially completes the proof for the hypothesis that centrifugal bonding during fabrication is the cause of dimensional instability of the AGC driver fuel during irradiation. Irradiation swelling of the fuel in Subassembly C-2210, as shown in Table I.F.5, was as expected.

TABLE I.F.4. Postirradiation Lengths of Fuel Pins from Subassembly C-2210
(Calculated burnup: 0.37 at. % max; 0.31 at. % avg)

ANL Batch 145 I				ANL Batch 146 I				ANL Batch 147 I	
AGC Centrifugal Bonding		ANL Impact Bonding		AGC Centrifugal Bonding		ANL Impact Bonding		ANL Impact Bonding	
Element No.	Length (in.)	Element No.	Length (in.)	Element No.	Length (in.)	Element No.	Length (in.)	Element No.	Length (in.)
1	13.3	3	13.5	4	12.8	2	13.5	6	13.5
5	13.0	7	13.6	11	13.0	9	13.5	8	13.5
10	13.2	13	13.5	17	12.9	12	13.5	18	13.5
14	13.0	16	13.5	21	13.0	15	13.5	32	13.5
20	13.2	23	13.5	24	12.9	19	13.5	38	13.5
26	13.0	28	13.6	27	13.0	22	13.5	40	13.5
30	13.0	34	13.5	31	12.9	25	13.5	45	13.5
33	13.1	36	13.6	37	12.9	29	13.5	62	13.5
41	13.0	39	13.5	44	12.9	35	13.6	68	13.6
46	13.2	43	13.5	49	12.9	42	13.5	81	13.5
51	13.0	48	13.5	52	12.9	47	13.5	91	13.4
55	13.4	53	13.5	56	12.9	50	13.5		
58	13.0	60	13.5	59	13.0	54	13.5		
66	13.1	64	13.5	63	12.9	57	13.5		
70	13.0	67	13.6	69	13.0	61	13.5		
71	13.0	72	13.5	73	12.9	65	13.5		
77	13.0	74	13.5	76	12.8	75	13.5		
80	13.2	85	13.6	79	12.9	78	13.5		
83	13.1	86	13.5	84	12.9	82	13.5		
88	13.0	90	13.5	89	12.9	87	13.5		
Average	13.09		13.53		12.92		13.50		13.50

TABLE I.F.5. Fabrication and Irradiation Data for Driver-fuel Subassembly C-2210
(Calculated burnup: 0.37 at. % max; 0.31 at. % avg)

Injection-casting Batch No.	Silicon Content of Fuel (ppm)	Number of Elements	Element Burnup Range (at. %)	Total Volume Swelling of Fuel (ΔV/V, %)	
				Average	Range
145 I	480	40	0.34-0.37	1.9	0.7-5.3
146 I	330	40	0.34-0.37	1.6	0.9-3.7
147 I[a]	475	11	0.34-0.37	1.7	1.2-2.4

[a]Impact-bonded cold-line fuel.

(C) Subassembly C-2182 (calculated burnup maximum, 0.88 at. %). This subassembly contained only AGC centrifugally bonded elements and represents the highest burnup achieved to date for elements "as-provided" by AGC. Tables I.F.6 and I.F.7 show postirradiation data obtained for the elements. It can be observed in Table I.F.6 that fuel-pin shortening has continued beyond that observed earlier for similar

fuel irradiated in Subassembly C-2178 to a peak burnup of 0.6 at. %. As shown in Table I.F.6, maximum shortening of 1.1 in. has resulted in one pin (AGC Batch 119, Element No. 14). Preliminary analysis of measurements of element (pin plus cladding) diameter does not indicate that diametral straining of the cladding has occurred as a result of the shortening and accompanying diametral growth of the fuel pins and as a result of the inherent irradiation swelling of the fuel at this burnup level. Irradiation swelling of the fuel, shown in Table I.F.7, appears to be much as expected.

TABLE I.F.6. Postirradiation Lengths of Fuel Pins in Subassembly C-2182[a]

(Calculated burnup: 0.88 at. % max; 0.74 at. % avg)

AGC Batch 100		AGC Batch 107		AGC Batch 112		AGC Batch 114	
Element No.	Length (in.)	Element No.	Length (in.)	Element No.	Length (in.)	Element No.	Length (in.)
6	12.6	2	12.5	13	12.5	1	12.6
16	12.6	11	12.6	19	12.5	10	12.6
18	12.6	15	12.6	23	12.5	20	12.7
38	13.5	21	12.6	35	12.5	31	12.6
55	12.7	26	12.6	43	12.6	51	12.5
76	12.6	44	12.8	47	12.5	54	12.9
80	12.8	49	12.6	62	12.6	57	12.7
		52	12.5	65	12.6	59	12.9
		74	12.6	68	12.5	88	12.8
		78	12.7				
		84	12.5				
		87	12.6				
Average	12.77		12.60		12.53		12.70
AGC Batch 119		AGC Batch 150		AGC Batch 153		AGC Batch 154	
Element No.	Length (in.)	Element No.	Length (in.)	Element No.	Length (in.)	Element No.	Length (in.)
5	12.5	4	12.6	3	12.6	7	12.5
10	12.7	8	12.9	12	12.8	17	12.5
14	12.4	24	12.6	22	12.8	27	12.6
30	12.6	29	12.9	25	12.6	28	12.6
33	12.6	32	12.9	48	12.8	39	12.5
37	12.7	36	12.6	50	12.7	46	12.5
45	12.5	40	12.9	63	12.8	61	12.5
53	12.7	41	12.7	66	12.6	64	12.5
67	12.5	56	12.6	85	12.5	69	12.5
70	12.5	58	12.7	86	12.7	71	12.5
73	12.5	60	12.7			75	12.6
79	12.5	72	12.8			81	12.5
89	12.7	77	12.9			83	12.5
		82	12.9			91	12.5
		90	12.6				
Average	12.57		12.75		12.69		12.52

[a]Average postirradiation length for all fuel pins in subassembly: 12.6 in. (range, 12.4-13.5 in.).

TABLE I.F.7. Fabrication and Irradiation Data for Driver-fuel Subassembly C-2182

(Calculated burnup: 0.88 at. % max; 0.74 at. % avg)

Injection-casting Batch No. (AGC No.)	Silicon Content of Fuel (ppm)	Number of Elements	Element Burnup Range (at. %)	Total Volume Swelling of Fuel (ΔV/V, %)	
				Average	Range
100	334	7	0.82-0.86	3.4	2.8-4.4
107	350	12	0.81-0.87	3.3	1.4-4.2
112	297	9	0.82-0.87	3.7	2.9-5.0
114	325	10	0.81-0.88	3.3	1.2-4.3
119	330	13	0.81-0.87	3.5	2.2-4.9
150	300	15	0.81-0.87	3.8	2.8-4.4
153	470	10	0.80-0.87	3.3	1.7-4.2
154	370	15	0.80-0.88	3.4	1.9-4.6

(D) Subassembly C-2195 (calculated burnup maximum, 0.35 at. %). Like several subassemblies previously reported, this subassembly contained AGC centrifugally bonded fuel. Of significance is the fact that the AGC casting batches represented were produced at a considerably later date than those present in the previously examined (and reported) subassemblies (C-2178, C-2181, C-2182, C-2183, and C-2189). Postirradiation results for Subassembly C-2195 are presented in Tables I.F.8 and I.F.9. As shown in Table I.F.8, shortening of the centrifugally bonded elements was similar to that observed for the earlier batches of AGC fuel in the subassemblies mentioned above. Irradiation swelling, as shown in Table I.F.9, also was similar and as expected.

TABLE I.F.8. Postirradiation Lengths of Fuel Pins in Subassembly C-2195

(Calculated burnup: 0.35 at. % max; 0.29 at. % avg)

AGC Batch 395		AGC Batch 477		AGC Batch 397		AGC Batch 456	
Element No.	Length (in.)	Element No.	Length (in.)	Element No.	Length (in.)	Element No.	Length (in.)
1	13.0	10	13.3	16	13.1	18	13.0
45	13.2	14	13.0	28	13.1	23	12.9
76	13.3	77	13.0	63	13.2	54	13.0
86	13.0					70	13.1
Average	13.12		13.10		13.13		13.00

AGC Batch 486		AGC Batch 415		ANL Batch 128 II	
Element No.	Length (in.)	Element No.	Length (in.)	Element No.	Length (in.)
21	13.3	73	13.2	4	13.4
24	13.1	91	13.2	6	13.5
43	13.5			19	13.6
62	13.3			29	13.4
				36	13.4
				41	13.4
				46	13.5
				49	13.4
				51	13.5
				59	13.5
				89	13.5
Average	13.30		13.20		13.50

TABLE I.F.9. Fabrication and Irradiation Data for Driver-fuel Subassembly C-2195

(Calculated burnup: 0.35 at. % max; 0.29 at. % avg)

Injection-casting Batch No.	Silicon Content of Fuel (ppm)	Number of Elements	Element Burnup Range (at. %)	Total Volume Swelling of Fuel (ΔV/V, %)	
				Average	Range
AG 395	475	4	0.32-0.34	0.81	0.45-1.0
128 II	332	11	0.31-0.35	1.78	1.16-2.84
AG 477	377	3	0.32-0.34	1.40	1.16-1.6
AG 397	438	3	0.32-0.34	0.89	1.67-1.89
AG 456	327	4	0.31-0.34	1.61	1.35-1.74
AG 486	408	4	0.32-0.35	1.54	1.27-1.84
AG 415	299	2	0.32-0.34	1.24	1.22-1.26
			For Subassembly	1.45	0.45-2.84

(E) Subassembly C-2208 (calculated burnup maximum, 0.38 at. %). This subassembly contained AGC elements from the same two AGC casting batches which were either AGC centrifugally bonded

or ANL impact bonded. The elements were characterized as to the positions of the respective fuel pins in the casting-mold array during injection casting and as to the orientation of the tops or bottom ends of the castings in their respective jacket assemblies. Since the experiment was designed during the time period when the anomalous irradiation performance of the fuel was thought to be possibly associated with procedures used in the injection-casting operation, the intent of the experiment was to investigate the effects of cooling rates of the cast pins and the pin-to-jacket loading orientation on the dimensional instability of the fuel pins during irradiation. Analysis of the postirradiation results for this subassembly did not show any observable correlation between the casting and jacket-loading parameters mentioned above and dimensional instability of the fuel pins during irradiation. Postirradiation length and volume-swelling results, summarized in Tables I.F.10 and I.F.11, are as expected.

TABLE I.F.10. Postirradiation Lengths of Fuel Pins in Subassembly C-2208

(Calculated burnup: 0.38 at. % max; 0.32 at. % avg)

AGC Batch 633				AGC Batch 628				Cold-line Fuel Batch 119 IH; Impact Bonding	
Centrifugal Bonding		Impact Bonding		Centrifugal Bonding		Impact Bonding			
Element No.	Length (in.)	Element No.	Length (in.)	Element No.	Length (in.)	Element No.	Length (in.)	Element No.	Length (in.)
1	13.0	6	13.5	19	13.2	10	13.5	23	13.5
4	13.2	24	13.5	29	13.3	14	13.5	51	13.5
16	13.0	36	13.5	41	13.1	28	13.5	86	13.5
18	13.0	46	13.5	45	13.1				
21	13.1	62	13.5	54	13.1				
43	13.2	73	13.6	59	13.1				
49	13.0	91	13.5	76	13.1				
63	13.0			89	13.3				
70	13.1								
75	13.2								
Average	13.08		13.50		13.16		13.50		13.50

TABLE I.F.11. Fabrication and Irradiation Data for Driver-fuel Subassembly C-2208

(Calculated burnup: 0.38 at. % max; 0.32 at. % avg)

Injection-casting Batch No.	Silicon Content of Fuel (ppm)	Number of Elements	Element Burnup Range (at. %)	Total Volume Swelling of Fuel (ΔV/V, %)	
				Average	Range
AG 633	428	17	0.32-0.37	1.3	0.62-1.84
AG 628	390	11	0.32-0.38	1.1	0.81-1.87
119 IH	486	3	0.20-0.37	2.1	1.99-2.18
			For Subassembly	1.28	

(2) Out-of-pile Support Studies (C. M. Walter)

A number of mechanisms have been postulated as being responsible for the shortening of AGC-produced fuel during irradiation. This behavior has never been seen in ANL-produced fuel. Preferred orientation, or texture induced during AGC fabrication of the fuel elements, has been confirmed as the cause of the shortening, and the AGC centrifugal bonding has been found to be specifically responsible for the anomalous irradiation behavior of the fuel.

X-ray diffraction is a prime tool in characterizing the texture of materials. It has been used along with irradiation experiments to predict and verify the performance of EBR-II driver fuel. The X-ray studies also have furnished some information on the nature of the phases present in this fuel.

Electrical resistivity also has been used for studying texture; however, the data produced are much less descriptive as to the type and degree of preferred orientation than those obtained by X-ray techniques. Although measurements of electrical resistivity are hard to interpret, they can be made quickly and easily.

Before it had been confirmed that texture was responsible for fuel shortening, fuel slumping due to overheating was considered as a possible cause. Therefore, data on the slumping of U-5 wt % Fs alloy were developed.

Because texture has been identified as being responsible for the shortening of AGC fuel and because X-ray diffraction was found to be invaluable in investigating this texture, the X-ray studies are strongly emphasized in the following discussion.

(A) X-ray Studies of Texture in AGC and ANL Fuel
(M. H. Mueller, H. W. Knott, S. Matras, and C. M. Walter)

Uranium-5 wt % fissium alloy is used for both the AGC and ANL fuel. In this alloy,* single-phase γ (body-centered cubic) is stable down to 725°C, at which point precipitation of U_2Ru (monoclinic) begins. The beta (tetragonal) phase apparently does not occur in this alloy. Precipitation of U_2Ru continues down to 642°C, at which point γ begins to reject α (orthorhombic) phase. The formation of δ (tetragonal) phase occurs at 552°C. The phase transformations are fairly sluggish in this alloy, so that as-cast material contains essentially all retained γ. The bonding treatment performed at 500°C for about 1 hr transforms the retained γ to the equilibrium phase of $\alpha + \delta + U_2Ru$, with the matrix being α. The difference between the ANL and AGC processes lies in this bonding step. ANL bonds by impact and AGC bonds by a centrifugal method which applies a stress on the fuel during the $\gamma \rightarrow \alpha$ transformation. It is this stress during the transformation that apparently produces the undesirable texture in the transformed orthorhombic α phase.

For an α-uranium sample having a small grain size that is entirely randomly oriented, the diffraction pattern has been well-established, and the relative intensities of the diffraction peaks have been

*Zegler, S. T., and Nevitt, M. V., Structures and Properties of Uranium Fissium Alloys, ANL-6116 (July 1961).

recorded. A sample possessing some degree of preferred orientation will exhibit diffraction peaks that have different relative intensities because of deviations from randomness. A measure of nonrandomness of a sample can be determined by observing the relative intensities of some number of these diffraction peaks, or reflections.

The so-called triplet reflections [(110), (021), and (002)] often have been used to describe the texture in α-uranium qualitatively. These reflections have been chosen because they have high intensities, appear in the front reflection region (i.e., they can be looked at in a bulk sample by using a diffractometer), and are at least qualitatively representative of the three crystallographic directions in α-uranium [i.e., (110) with the "a" direction, (021) with the "b" direction, and (002) with the "c" direction]. During irradiation, α-uranium has been found to grow in the "b" direction, to shrink in the "a" direction, and to be dimensionally stable in the "c" direction. Therefore, an abundance of "b"-direction orientation along the axis of a fuel pin would tend to show up as a greater-than-random relative intensity for the (021) reflection in a transverse section of the fuel pin and would result in an axial-growth texture. Conversely, an abundance of "a"-direction orientation along the axis of a fuel pin would tend to show up as a greater-than-random relative intensity for the (110) reflection in a transverse section of the fuel pin and would result in radial-growth or axial-shortening texture. This shortening is the problem with AGC fuel.

Because the "c" direction [associated with the (002) reflection] neither shrinks nor grows during irradiation, it can be essentially ignored for discussion purposes here. Only the relationship between the (110) and (021) reflections will be utilized in this qualitative analysis of texture.

Table I.F.12 lists the relative intensities of triplet reflections for cast and bonded pins. In this table, "tops" and "bottoms" refer to the top and bottom of the pin with respect to the fuel element, not with respect to the casting. This is an important point because it has been postulated that preferred orientation is due to the stress produced on the pin during transformation from γ to α during centrifugal (AGC) bonding. If this reasoning is valid, the stress during centrifugal bonding should be greatest near the bottom of the pin, and, accordingly, the preferred orientation should be greatest near the bottom of a pin that has been bonded centrifugally. This rationale is substantiated by the results of examinations of three AGC-cast and -bonded pins (traces 6, 7, 8, 9, 10, and 11 in Table I.F.12). According to the (110) and (021) reflections, these pins tend to show more random orientation in the tops than in the bottoms. The bottoms have a definite excess of (110) or "a"-type orientation, which indicates a radial-growth texture. This finding is consistent with irradiation results with this fuel, which show that radial growth is

greatest near the bottom of the fuel, thereby giving the overall net effect of axial shortening. On the other hand, the relative intensities for ANL-cast and -bonded fuel (traces 2, 3, 4, and 5) show near-random orientation for tops and bottoms, according to the (110) and (021) reflections, and are consistent with the fact that this type of fuel has never shown preferred radial growth (axial shortening).

TABLE I.F.12. Relative Intensities of Triplet Reflections for Cast and Bonded Pins

X-ray Trace No.	Description	Pin No.	Batch No.	Relative Intensities (110)	(021)	(002)
1	Random α uranium	-	-	0.7	1.0	0.5
2	ANL-cast and -bonded (top)	6	ANL-047 IH	0.8	1.0	0.6
3	ANL-cast and -bonded (bottom)	6	ANL-047 IH	0.8	1.0	0.7
4	ANL-cast and -bonded (top)	72	ANL-0457 EUF	0.8	1.0	1.5
5	ANL-cast and -bonded (bottom)	72	ANL-0457 EUF	0.8	1.0	0.5
6	AGC-cast and -bonded (top)	02301	AGC-107	0.7	1.0	0.9
7	AGC-cast and -bonded (bottom)	02301	AGC-107	1.1	1.0	0.7
8	AGC-cast and -bonded (top)	40332	AGC-546	0.9	1.0	0.9
9	AGC-cast and -bonded (bottom)	40332	AGC-546	1.0	1.0	1.1
10	AGC-cast and -bonded (top)	01888	AGC-107	0.8	1.0	0.7
11	AGC-cast and -bonded (bottom)	01888	AGC-107	1.0	1.0	0.5
12	AGC-cast and ANL-bonded (top)	17684	AGC-577	0.8	1.0	0.6
13	AGC-cast and ANL-bonded (bottom)	17684	AGC-577	0.8	1.0	1.0
14	AGC-cast, heat treated 1 hr @ 500°C, and AGC-bonded (top)	44870	AGC-620	0.8	1.0	0.8
15	AGC-cast, heat treated 1 hr @ 500°C, and AGC-bonded (center)	44870	AGC-620	0.8	1.0	0.7
16	AGC-cast, heat treated 1 hr @ 500°C, and AGC-bonded (bottom)	44870	AGC-620	0.7	1.0	0.7
17	AGC-cast and -bonded, heat treated 1 hr @ 675°C and second heat treatment 2 hr @ 500°C (top)	02301	AGC-107	0.7	1.0	0.7
18	AGC-cast and -bonded, heat treated 1 hr @ 675°C and second heat treatment 2 hr @ 500°C (bottom)	02301	AGC-107	0.8	1.0	0.5
19	ANL-cast and -bonded, heat treated 1 hr @ 675°C and second heat treatment 2 hr @ 500°C (top)	72	ANL-0457 EUF	0.8	1.0	0.7
20	ANL-cast and -bonded, heat treated 1 hr @ 675°C and second heat treatment 2 hr @ 500°C (bottom)	72	ANL-0457 EUF	0.8	1.0	0.6
21	AGC-cast and -bonded, heat treated 1.5 hr @ 660°C and second heat treatment 2 hr @ 500°C (top)	14131	AGC-295	0.8	1.0	0.6
22	AGC-cast and -bonded, heat treated 1.5 hr @ 660°C and second heat treatment 2 hr @ 500°C (bottom)	14131	AGC-295	0.8	1.0	0.6

These results indicate that the AGC process for fabricating fuel elements should be changed to prevent the introduction of undesirable textures. Two approaches are possible. Impact bonding could be used instead of centrifugal bonding. The X-ray results (traces 12 and 13) show that fuel cast by AGC and impact bonded by ANL has nearly random orientation. Irradiation results show that this fuel does not shorten during irradiation, thereby confirming the predictions based on the X-ray diffraction studies. The second approach is heat treatment of the as-cast fuel to transform retained γ to α before centrifugal bonding, thus eliminating stress during transformation. The X-ray results (traces 14, 15, and 16) show that fuel cast by AGC, heat treated for 1 hr at 500°C, and centrifugally bonded by AGC has nearly random orientation. Irradiation results show that this type of fuel also does not shorten during irradiation, again confirming the predictions based on X-ray diffraction studies. It can be concluded that either change in the process would produce fuel devoid of undesirable texture.

Finally, means for reclaiming the fuel that already has been fabricated by AGC casting immediately followed by AGC centrifugal bonding were investigated. Fuel fabricated by this process already contains an undesirable texture in the transformed α phase. The logical

heat treatment required to remove this texture involves transforming all the α-uranium back to γ phase by heating above 642°C and then retransforming the new γ back to α by heat treatment at 500°C. The X-ray results after performing such a double heat treatment are given in traces 17, 18, 19, and 20; these traces should be compared to traces 4, 5, 6, and 7, which were taken before the heat treatments. Data for an ANL-cast and -bonded pin (traces 4, 5, 19, and 20) have been included as a reference point. The (110) and (021) reflections show that the randomization results from the double heat treatment. X-ray traces 21 and 22, for an AGC-cast and -bonded element given a similar double heat treatment, show results similar to those in traces 17 and 18, thereby indicating that this element along with others receiving the same heat treatments should perform satisfactorily under irradiation. About 60 elements given this double heat treatment were irradiated during EBR-II Run 37; no pin shortening occurred.

X-ray texture studies also were made of ANL and AGC as-cast fuel pins. Tops and bottoms of randomly selected pins and of pins from the inner and outer portions of the casting bundle were investigated; no important differences could be detected. This finding is further evidence that the undesirable textures obtained during element fabrication are related to the AGC centrifugal-bonding technique and not to the pin-casting process.

All the ANL texture studies have been only qualitative. The intensities were obtained by measuring peak intensities above background rather than by measuring integrated intensities. The peaks are not fully resolved (sharp); therefore, overlapping is almost certainly present, which results in some contribution of intensity to a given peak from adjacent peaks. Because all phases and their associated peaks have not been positively identified, there exists the possibility that unresolved additional peaks lie below the (110), (021), and (002) α-uranium peaks on which this texture analysis is based. Finally, the three reflections on which the texture determination is based by no means describe the complete texture of a sample; many more reflections must be included to arrive at even a semiquantitative description of texture. A more quantitative study is under way at Savannah River Laboratory. Small differences in the intensity ratio of (110)/(021) from random are rather meaningless, but larger deviations do appear to be significant. Without the results of irradiation behavior, however, it would have been quite difficult to differentiate between meaningful and meaningless X-ray intensity ratios.

The following conclusions can be drawn from the X-ray studies and the irradiation results:

1. AGC should be able to produce fuel pins, either by impact bonding or by heat treating the as-cast pins before centrifugal bonding, that will not shorten during irradiation.

2. The AGC-cast and -bonded elements already fabricated probably can be reclaimed by first heat treating at 660°C and then heat treating again at 500°C.

3. The [(110), (021), (002)] triplet probably can be used, with some reservations, as a process check to predict irradiation-shortening behavior of EBR-II fuel pins.

4. More quantitative X-ray studies are required before the triplet can be used with absolute confidence as a process check.

(B) Electrical-resistivity Measurements of AGC and ANL Fuel (W. N. Beck)

Electrical-resistivity measurements were made of AGC as well as ANL pins as a support effort in identifying differences in structure of the two sources of fuel.

Electrical resistivity in metals is the impedance to electron flow and is a function of temperature, dislocations, orientation, impurities, density, lattice distortion, etc. The U-5 wt % Fs in a predominant α phase (the stable phase at room temperature) possesses the typical metallic positive temperature coefficient of electrical resistivity. The alloy in the predominantly γ phase, on the other hand, will have a higher value of resistivity and a negative temperature coefficient.

The resistivity measurements were comparative in that prior resistance data for the ANL production alloy that was known to be dimensionally stable during irradiation were used as a reference to which the AGC fuel was compared.

The measurements were performed with nonirradiated fuel pins which were characterized by either manufacturing process, source, and/or heat treatment. The characterization factors were:

1. AGC as-cast material;

2. ANL cast and ANL bonded;

3. AGC cast and AGC bonded;

4. AGC cast and AGC bonded, followed by one-step heat treatment: heat treated at 660°C for 1.75 hr and then air cooled;

5. AGC cast and AGC bonded, followed by two-step heat treatment: (1) heat treated at 660°C for 1.75 hr and then air cooled; (2) heat treated at 500°C for 2 hr and then air cooled;

6. AGC cast and ANL bonded;

7. AGC cast, then heat treated at 500°C for 1 hr prior to centrifugal bonding.

The resistivities were measured over 3.2-in.-long portions near the top, middle, and bottom of a 13.5-in.-long fuel pin using a double Kelvin bridge and knife-edge contacts. Resistivity values were obtained at -200 and +25°C. The results, which are listed in Table I.F.13 are summarized as follows:

1. The principal difference between the ANL-cast and ANL-bonded pin and the AGC-cast and AGC-bonded pin was that, although both were essentially in the α phase, the resistivity of the ANL pin was higher and was more uniform from top to bottom. The AGC pin showed the top to have a resistivity of 24.5 microhm-cm at -200°C but the middle and bottom had a low resistivity (~18 microhm-cm at -200°C). The particular AGC casting batches examined were those which had a tendency to shorten during irradiation. X-ray diffraction studies of this fuel indicated preferred orientation at the middle and bottom of these castings.

TABLE I.F.13. Electrical-resistivity Measurements of Nonirradiated AGC and ANL Fuel Pins

Pin Condition		Resistivity (microhm-cm)		Slope [microhm-cm (100)/°C]
		-200°C	+25°C	
AGC as-cast	Top	74	69	-2.2
	Middle	75	69	-2.6
	Bottom	74.5	69	-2.4
ANL cast and ANL bonded	Top	30	48.9	8.4
	Middle	27.2	47.0	8.8
	Bottom	27.3	47.8	9.1
AGC cast and AGC bonded	Top	24.5	46.5	9.7
	Middle	17.5	42.0	10.8
	Bottom	18.2	42.0	10.5
AGC cast and AGC bonded; heat treated at 660°C for 1.75 hr and air cooled	Top	70.0	68.5	-0.6
	Middle	70.0	68.5	-0.6
	Bottom	70.0	68.5	-0.6
AGC cast and AGC bonded; heat treated at 660°C for 1.75 hr, air cooled, heat treated again at 500°C for 2 hr, and then air cooled	Top	24.0	46.8	10.1
	Middle	22.5	45.5	10.2
	Bottom	20.5	46.0	11.3
AGC cast and ANL bonded	Top	24.0	46.7	10.0
	Middle	23.8	45.5	9.6
	Bottom	23.8	46.0	9.8
AGC cast; heat treated at 500°C for 1 hr prior to centrifugal bonding	Top	33.8	50.5	7.4
	Middle	32	46.5	6.4
	Bottom	32.3	50.8	8.2

2. The AGC as-cast pin was in the γ phase and had a uniform resistivity from end to end.

3. The AGC-cast and ANL-bonded pin differed from the AGC-centrifugally bonded pins in that values for slope of resistivity versus temperature and resistivity of the middle and bottom sections of the former pin were essentially the same as those for the top section. These pins did not shorten during irradiation.

4. Heat treating the AGC-cast and AGC-bonded fuel at a temperature of 660°C for time intervals ranging from 0.25 to 1.75 hr brought about a uniform and rapid transformation to the two-phase region. A subsequent heat treatment at a temperature of 500°C for periods up to 2 hr stabilized the fuel in the α phase and eliminated the previously observed preferred orientation in the middle and bottom of the pin. The irradiation results showed that these pins did not shorten.

5. An AGC pin which had been heat treated at 500°C for 1 hr prior to centrifugal bonding had higher measured values of resistivity (~33 microhm-cm at -200°C). The top and bottom of the casting had the same resistivity, but the middle of the pin was shown by X-ray reflections to have a degree of preferred orientation. Similar pins did not shorten during irradiation.

The slope of resistivity versus temperature does not appear to be a reliable indicator of preferred orientation. The absolute value of the resistivity does, however, indicate that pins having resistivities below 20 microhm-cm at -200°C do contain undesirable textures. Further verification of this would be necessary before the technique could be adopted as a process check.

(C) Dilatometric Determination of Slumping Rates for AGC Fuel (S. Matras and C. M. Walter)

Dilatometric measurements were made primarily to determine the temperature at which the fuel pins would begin to slump under their own weight. Data for thermal expansion that were also obtained are incidental to the purpose of the investigation. Accordingly, all measurements and calibration runs were performed with specimens loaded to approximately the weight of an average fuel pin.

In the tests, a combined weight of 64.35 g (quartz pushrod + brass weight + linear-variable-differential-transformer core) applied a stress of 6.12 g/mm^2 at the base of a 0.144-in.-dia fuel pin. The length of the pin specimens varied from 0.995 to 0.998 in. A programmed heating rate of 3°C/min was adopted to allow for a convenient

heat-up time and a time-at-temperature during a normal working day. Dilatometric samples were taken from two AGC batches (107 and 112), both of which had shown shortening during irradiation.

The first evidence of slumping was observed at about 950°C for a sample from AGC Batch 112. This observation was confirmed on a sample from AGC Batch 107, and slumping rates were obtained at 954, 970, and 990°C for this sample:

Slumping Rate $\left(\frac{\text{in./in.}}{\text{min}}\right)$	Temperature (°C)
1.1×10^{-5}	954
5.0×10^{-5}	970
3.5×10^{-4}*	990

Figure I.F.1 shows the slumping curves obtained for this sample.

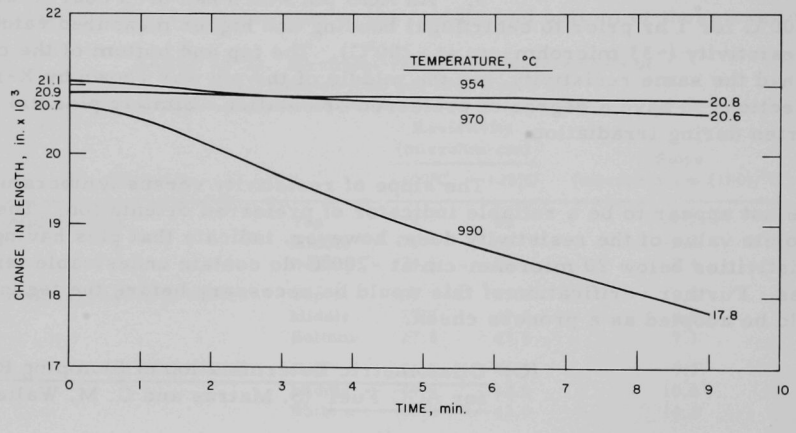

Fig. I.F.1. Slumping Rate for AGC Fuel Pin under Its Own Weight Stress of 6.12 g/mm^2

The very high temperature at which slumping occurs in this fuel is reassuring. The U-5 wt % Fs solidus occurs at 1002°C.**

(b) Influence of Composition on Irradiation-induced Swelling of U-5 Fs Driver-fuel Alloy. A study was initiated to determine more rigorously the influence of compositional variations in U-5 wt % Fs alloy driver fuel on irradiation-induced swelling. Postirradiation data are being analyzed, and a survey report will be prepared.

*A slight reaction with the quartz pushrod may have influenced this slumping rate.

**Saller, H. A., et al., Properties of a Fissium-Type Alloy, BMI-1123 (Aug 1956).

c. Fuel Handling and Transfer (N. R. Grant and P. Fineman)

A summary of fuel handling operations is included in Table I.F.14.

TABLE I.F.14. Summary of FCF Fuel Handling

	9/16/69 through 10/15/69	Total This Year
Subassembly Handling		
Subassemblies received from reactor		
Driver fuel (all types)	18	119
Experimental	2	20
Other (blanket)	1	5
Subassemblies dismantled for surveillance, examination, or shipment to experimenter		
Driver fuel	14	113
Experimental	1	19
Other (blanket)	1	3
Driver-fuel elements to surveillance	535	5472
Number from subassemblies	14	113
Subassemblies transferred to reactor		
Driver fuel	1	57
Experimental	2	9
Fuel-alloy and Waste Shipments		
Cans to burial ground	5	27
Skull oxide and glass scrap to ICPP	0	2
Recoverable fuel alloy to ICPP		
Fuel elements	2 (34.91 kg of alloy)	32 (539.70 kg of alloy)
Subassemblies	10 (50.75 kg of alloy)	17 (88.75 kg of alloy)
Nonspecification material	0	5 (84.3 kg of alloy)

d. Experimental Support (V. G. Eschen, N. R. Grant, R. V. Strain, J. W. Rizzie, and C. L. Meyers)

Subassembly XO69, a Mark-H37 irradiation subassembly containing mixed-oxide fuel elements from the PNL-7 series, was fabricated.

Subassembly XO40A, reconstituted from Subassembly XO40, was returned to the reactor for further irradiation.

An additional Mark-B7 capsule (from Subassembly XO42A) containing tantalum was returned to the experimenter. The balance of the capsules (five) from this subassembly are being stored in the argon cell.

Subassembly XO12, a Mark-A subassembly containing 19 NUMEC mixed-oxide capsules, was dismantled. All the capsules were neutron

radiographed, weighed, and visually examined, and diameter measurements were obtained for two capsules. The same 19 capsules were reassembled into Subassembly XO12A, and the subassembly was returned to the reactor.

Subassembly XO34A, a Mark-B7 irradiation subassembly, was reassembled using four structural elements from Subassembly XO34 and three new structural elements (all ORNL). The subassembly was transferred to the reactor.

Subassembly XO18B, a Mark-B7 subassembly, was reassembled in the air cell with seven structural elements (three GE, three ANL, and one PNL), and the subassembly was transferred to the reactor.

Subassembly XO32, a Mark-A subassembly containing 19 PNL mixed-oxide capsules, was dismantled. All the capsules were weighed, visually examined, neutron radiographed, and returned to the experimenter.

One flat of the irradiated subassembly hexagonal tubing (average midplane fluence, 8.5×10^{22} nvt) from high-burnup Subassembly XA08 was shipped to GE for their examination. Specimens obtained along the length of two other flats of this tubing were shipped to ANL-Illinois. Additional specimens from locations near where the latter samples were selected have been retained in ANL-Idaho by the FCF investigators. Tests to be conducted at the FCF include density, metallography, wall-thickness determination, and fluence determinations.

PUBLICATIONS

^{252}Cf Half-Life by Neutron Counting: Revision
A. DeVolpi and K. G. Porges
Inorg. Nucl. Chem. Letters 5, 699 (1969)

The Dissolution Kinetics of Fe_3C in Ferrite
F. V. Nolfi, P. G. Shewmon, and J. S. Foster*
Abstract Bull. Met. Soc. AIME Fall Mtg., Philadelphia, Pa., Oct. 13-16, 1969, p. 49

Application of Thermodynamic and Kinetic Parameters of theV-O-Na System to the Sodium Corrosion of Vanadium-Base Alloys
D. L. Smith and T. F. Kassner
Abstract Bull. Met. Soc. AIME Fall Mtg., Philadelphis, Pa., Oct. 13-15, 1969, p. 65

*Carnegie-Mellon University.

II. OTHER FAST REACTORS--OTHER FAST BREEDER REACTORS--FUEL DEVELOPMENT

A. Irradiation Effects, Mechanical Properties and Fabrication

1. Electron Microscopy of Irradiated Tensile Specimens (S. D. Harkness)

Last Reported: ANL-7561, pp. 71-72 (March 1969).

Irradiated tensile specimens are being studied by transmission electron microscopy. The original tensile specimens were taken from a flat of a safety-rod guide thimble irradiated in EBR-II position 3D1 to a peak fluence of 9×10^{22} n/cm^2. The guide thimble was fabricated from Type 304 stainless steel and irradiated in the solution-annealed condition. The tensile results from this study have been reported (see Progress Report for August 1969, ANL-7606, p. 84).

The study was initiated to establish to what extent microstructural annealing was occurring during tensile testing at elevated temperatures and whether dislocation channeling was occurring during testing.

a. Annealing Results

Since knowledge of the microstructure is important to the interpretation of the tensile results, it is essential to know whether substantial microstructural annealing is occurring during the time (~35 min) spent at elevated temperature. The initial results from the 450°C test temperature indicate little annealing is occurring. Three specimens were examined, corresponding to irradiation below, middle, and above the reactor core. None showed any evidence of annealing, and both number densities and average sizes remained constant.

A study of one sample tested at 750°C has indicated annealing during testing. This particular sample was irradiated at 371°C to a fluence of 1×10^{22} n/cm^2. As a result of the low irradiation temperature and fluence, the initial void size was small (75 Å). No voids were observed in the specimen after tensile testing. The microstructure was completely free of any type of radiation damage. The testing at the elevated temperature did result in a plate-like precipitate. The structure of the precipitate is now under analysis.

The results of this study indicate the importance of considering the possibility of microstructural change during testing.

b. Dislocation Channeling

Dislocation channeling was observed in one sample tested at 450°C. This sample was irradiated at 375°C to a fluence of 2×10^{22} n/cm^2.

As shown in Fig. II.A.1, channels of loop free area were formed by the slip dislocations. Voids within the channel are observed to be elongated in the apparent direction of slip. It is speculated that this void elongation is the result of shearing the void in half.

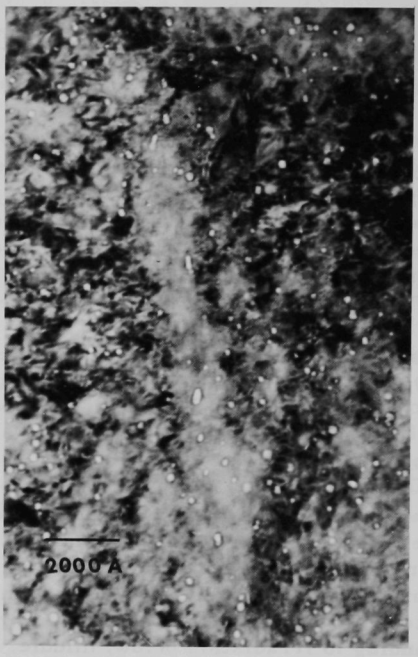

Fig. II.A.1. Dislocation Channeling in an Irradiated Type 304 Stainless Steel Tensile Specimen Tested at 450°C. Note elongation of voids within the channel.

III. GENERAL REACTOR TECHNOLOGY

A. Applied and Reactor Physics Development

1. Theoretical Reactor Physics--Research and Development

a. Theoretical Reactor Physics

(i) Reactor Computation and Code Development (B. J. Toppel)

(a) Argonne Reactor Computation (ARC) System

Last Reported: ANL-7618, pp. 83-84 (Sept 1969).

Problems were run with standard path STP007 to test the two-dimensional perturbation module with respect to region-dependent buckling changes for finite x-y geometry, i.e., the reactor is a parallelepiped. A reactor with the standard four compositions was considered (see Progress Report for February 1969, ANL-7553, pp. 77-80). In the z-direction the unperturbed reactor was taken as uniform with a half-height $h_{1/2}$ of 102 cm and an extrapolation distance ℓ of 14 cm. In the problems the extrapolation distance was included by imposition of the logarithmic boundary condition. A buckling search was made to attain the critical system; it converged to an extrapolated half-height of 116.882 cm for the transverse, z, direction.

The configuration is described in Table III.A.1, and the comparison of results of perturbation with diffusion calculations is given in Table III.A.2. The diffusion calculations were run with very tight convergence criteria so that the values of k were given to eight significant figures. From Table III.A.2 it is seen that there is excellent agreement between the diffusion and the perturbation calculations, since the discrepancies are less than 0.1%.

TABLE III.A.1. Reactor Configuration for Two-dimensional Region-dependent Buckling and Isotopic Cross-section Perturbations

Region	Composition[a]	X_L (cm)	X_U (cm)	Mesh Pts.
1	C1	0	9.2	4
2	C2	9.2	54.0	12
3	C3	54.0	94.0	12
4	C4	94.0	148.0	8

[a]See Progress Report for February 1969, ANL-7553, pp. 77-80.

TABLE III.A.2. Comparison of Perturbation and Diffusion Calculations for Two-dimensional Region-dependent Buckling Perturbations

Problem	Region	$h_{1/2}$ (cm)	ℓ (cm)	$\Delta k/k^2$ (10^{-4})	
				Diffusion	Pert
1	1	102.5	16.0	1.006	1.0053
2	2	100.882	15.75	-1.203	-1.2024
3	3	96.0	16.0	-1.093	-1.095

Recently, the versatility of the ARC system has been increased by permitting run-time modification of individual isotopic (microscopic) cross sections. The two-dimensional perturbation module was tested for isotopic cross-section changes for the same configuration as was used in studying the region-dependent buckling perturbation. Individual cross sections were multiplied by factors that yield perturbations of the order of 10^{-4} $\Delta k/k^2$. In Table III.A.3 the perturbations are described and the comparison of the results of diffusion and perturbation computations is given. For ^{239}Pu the capture, fission, and nu x fission cross sections are perturbed while for sodium the transport and elastic scattering cross sections are perturbed. Since leakage is affected only by a change in the transport cross section, it was only for that cross section that the perturbation computations used both options for δD in the leakage term.

TABLE III.A.3. Comparison of Two-dimensional Perturbation and Diffusion Calculations for Isotope Cross-section Changes

Isotope	σ_x	Groups		Factor	$\Delta k/k^2$ (10^{-4})		
		From	To		Diffusion	Pert (δD_1)	Pert (δD_2)
^{239}Pu	σ_c	1	22	1.004	-1.845	-	-1.8457
	σ_c	4	6	1.04	-1.172	-	-1.1726
	σ_f	1	22	1.005	-1.007	-	-1.0067
	σ_f	4	6	1.003	-1.443	-	-1.4437
	$\nu\sigma_f$	1	22	1.0003	2.115	-	2.1152
	$\nu\sigma_f$	4	6	1.002	3.273	-	3.2727
Na	σ_{tr}	1	22	1.01	1.868	1.3580	1.3598
	σ_{tr}	4	6	1.03	2.387	1.79171	1.8005
	$\sigma_{i\rightarrow j}$	3-5	4-7	1.02	-1.771	-	-1.7747

From Table III.A.3, we see that for changes in all cross sections except transport the agreement between diffusion and transport calculations is excellent. However, for changes in the transport cross section, there are serious discrepancies between the diffusion and the perturbation computations. These discrepancies are being investigated further.

(b) MC² Capability in the ARC System

Last Reported: ANL-7618, pp. 84-85 (Sept 1969).

The maximum code dimensions available for the calculations of an MC² problem in ARC is dictated by the available space in the main core of the computer. At present, the maximum dimensions of pertinent quantities are 20 materials, 4 isotopes for each material, 70 broad energy groups, 70 fine energy groups, 2100 ultrafine energy groups, 2000 resolved resonances, and 100 energy points in the unresolved resonance region.

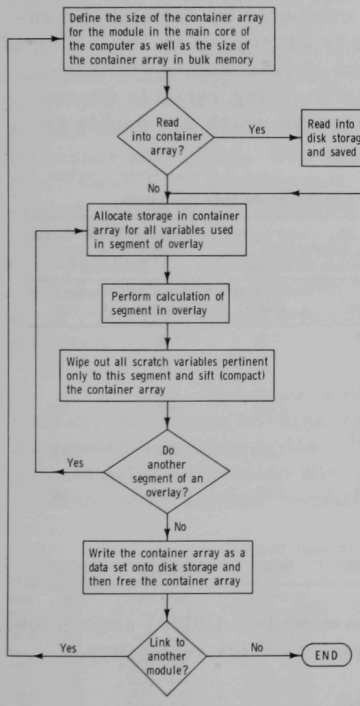

Fig. III.A.1. Flow Diagram for Incorporating BPØINTER into the Modules CSI001, CSC001, CSC002, and CSC003 of the ARC System

The effort presently underway in the refinement of MC² in ARC on the IBM System/360 computer is to variably dimension the arrays in modules CSI001, CSC001, CSC002, and CSC003* by the use of BPØINTR.** With this refinement, the user can utilize bulk memory (128 K double words) as well as the main core memory (100 K double words) to expand the code dimensions. Another option available to the user is to expand some of the code dimensions at the expense of other dimensions by utilizing only the main core available in the computer.

Figure III.A.1 displays the flow diagram for incorporating BPØINTR into the structure of modules CSI001, CSC001, CSC002, and CSC003. The container array is initially empty when module CSI001 is called. Only the arrays needed in subsequent modules are

*Toppel, B. J., Tabulation of Current ARC Modules, Standard Paths, and Catalogued Procedures, September 8, 1969 (Internal Memorandum).

**Kennedy, A. S., A Dynamic Storage Allocation Program, Applied Mathematics Division ANL Technical Memorandum No. 98 (February 28, 1967); Corrections to PØINTR for LCS, Applied Mathematics Division, ANL Internal Technical Memorandum (January 29, 1969); Henryson, H., and Toppel, B. J., Modifications to BPØINTR--A Dynamic Storage Allocation Program Utilizing Bulk Memory, October 6, 1969 (Internal

saved in the container array. Before control of module CSI001 is released, it writes the container array onto disk storage. The next module called then allocates space for the container array (this space may vary from module to module) and then reads into core the arrays saved from the previous module. Before this module is released, it saves only pertinent arrays which subsequent modules will use. In addition to the arrays contained in the container array, each module still writes pertinent data sets on disk storage so that they may be used as input by modules other than those related to an MC^2 calculation. Therefore after incorporating BPØINTR into these four modules they will still retain the modular concept of ARC.

The space saved in the computer by variably dimensioning quantities versus fixed dimensioning is illustrated by the listing of some of the variables used in an MC^2 problem in ARC and is given in Table III.A.4. The spaced saved in the computer using variable dimensioned arrays is substantial, especially for arrays which are doubly or triply subscripted.

TABLE III.A.4. View of Some Sample Variables Used in an MC^2 Calculation and the Space They Require

Description of Array	Definition of the Subscripts in the Array	Space Required Using Current Fixed Dimensions		Space Required for Typical Problem Using Variable Dimensions	
		Array Dimensions	Double Words Used	Array Dimensions	Double Words Used
Nuclide temperature	Materials	20	20	12	12
Broad-group energy boundaries	Broad energy groups	70	70	27	27
Abundance of each isotope in unresolved calculation	Resolved resonances	2000	2,000	592	592
Homogenized resonance capture cross section	Ultrafine energy groups	2100	2,100	1560	1,560
Energy at which unresolved calculation is to be done	Energy points, materials in problem x isotopes per material	100,20X4	8,000	16,12X1	192
Average reduced neutron width	Energy points, channel spins x angular momentum states, materials in problem x isotopes per material	100,4X2,20X4	64,000	16,4X2,12X1	1,536

At the present time, two modules, CSI001 and CSC001, have been variably dimensioned are are being tested for reliability.

2. Nuclear Data--Research and Development

a. Cross Section Measurements (N. D. Dudey)

(i) Spectrum-averaged Measurements

Last Reported: ANL-7618, p. 88 (Sept 1969).

Experimental work has been completed on the determination of the number of captures, the number of fissions, and the capture-to-fission

ratios (alpha) for samples of ^{239}Pu irradiated in various positions in the core and blankets of EBR-II. Preliminary values of capture-to-fission ratios for ^{233}U were reported previously in ANL-7618.

The ^{239}Pu was irradiated in the form of a dry nitrate salt. The sample containers were of Type 304L stainless steel and were doubly canned to prevent contamination. The special subassemblies containing the samples were designed to reduce perturbations in the neutron spectrum, that is, they were identical to driver or blanket subassemblies except for the small displacement due to the sample capsules. As an additional precaution in preserving an unperturbed neutron spectrum, one sector of the reactor was reserved for this experiment.

Upon removal from the subassembly, the stainless steel capsules containing the samples were cleaned and then dissolved in $HCl-HNO_3$ to which cesium carrier had been added. The cesium was separated as the perchlorate, and the plutonium was separated and purified by hexone extraction. The number of fissions was determined by counting the $^{137}Cs-^{137m}Ba$ activity with a high-resolution Ge(Li) detector. The cesium values were corrected for in-pile decay, for fluctuations in the power level of the reactor, and for burnup of the target and product nuclides during irradiation. The number of fissions was calculated using a ^{137}Cs fission yield of 6.58%.* The capture values were determined by mass analysis with a 12-in.-radius, 60° sector, surface-ionization mass spectrometer.**

The results are shown in Table III.A.5 for 14 positions in EBR-II. All known uncertainties are included in the table except (1) the experimental errors in the ^{137}Cs fission-yield determination and (2) the uncertainties associated with the applicability of this particular fission yield to the irradiation conditions.

TABLE III.A.5. Capture-to-Fission Ratio (Alpha) for ^{239}Pu as a Function of Position in EBR-II

Sample Position					Sample Position				
Axial (cm)	Radial (cm)	Captures per 10^4 Atoms of ^{239}Pu	Fissions per 10^3 Atoms of ^{239}Pu	Alpha (Captures/Fissions)	Axial (cm)	Radial (cm)	Captures per 10^4 Atoms of ^{239}Pu	Fissions per 10^3 Atoms of ^{239}Pu	Alpha (Captures/Fissions)
+72.9	2.50	6.30 ± 0.06	1.31 ± 0.04	0.480 ± 0.016	+0.32	10.21	24.65 ± 0.25	29.93 ± 0.97	0.082 ± 0.003
+30.2	2.86	22.40 ± 0.22	10.41 ± 0.34	0.215 ± 0.007	+0.32	21.25	27.90 ± 0.28	28.26 ± 0.92	0.099 ± 0.003
+17.0	2.86	22.05 ± 0.22	17.89 ± 0.58	0.123 ± 0.004	+0.42	30.62	10.25 ± 0.10	7.44 ± 0.24	0.138 ± 0.005
+8.5	2.86	24.30 ± 0.24	23.48 ± 0.76	0.104 ± 0.004	+0.42	40.83	21.15 ± 0.21	14.76 ± 0.48	0.143 ± 0.005
0.0	2.86	26.40 ± 0.26	30.93 ± 0.10	0.085 ± 0.003	+0.42	51.03	10.00 ± 0.10	5.30 ± 0.17	0.189 ± 0.006
-8.5	2.86	24.80 ± 0.25	26.53 ± 0.86	0.093 ± 0.003	+0.42	61.24	6.02 ± 0.06	2.38 ± 0.77	0.253 ± 0.009
-17.0	2.86	24.35 ± 0.24	18.01 ± 0.58	0.135 ± 0.005	+0.42	71.45	3.51 ± 0.04	0.91 ± 0.30	0.385 ± 0.013

*Lisman, F. L., et al., Burnup Determination of Nuclear Fuels, IN-1277 (1969).

**Mass analyses performed by M. Laug, Idaho Division.

The uncertainties related to the effect of neutron energy on the ^{137}Cs yield from fission of ^{239}Pu are well-known. The value of 6.58% reported by Lisman et al.** was determined from fuel irradiated in EBR-I (median neutron energy, ~700 keV); their value for the ^{137}Cs thermal-fission yield is 6.74%. If the data of Kafalas and Crouthamel** are corrected to the presently accepted half-life of ^{137}Cs (30.0 yr), a value of 6.27% is obtained for the fission yield of ^{137}Cs in a fission spectrum (median neutron energy, 1.5 MeV). If we interpolate these values linearly, assuming that the median neutron energy in EBR-II is ~450 keV in the core and ~100 keV in the outer blanket, we obtain values of the ^{137}Cs fission yield for EBR-II varying from 6.63% at core center to ~6.72% in the outer blanket.

A more complete discussion of the ^{137}Cs yield values and the implications of the measured alpha values will be presented when reactor physics calculations of the neutron spectra have been completed for the reactor runs in which the measurements were made.

b. Reactor Code Center (M. Butler)

Last Reported: ANL-7618, pp. 93-94 (Sept 1969).

In October, four computer programs were incorporated into the Code Center library. GAKIT (ACC Abstract 370), developed by Gulf General Atomic, is a one-dimensional multigroup diffusion-theory kinetics code that allows temperature feedback from a coupled two-dimensional heat-transfer calculation. GAKIT is written for the UNIVAC 1108. RAPFU (ACC Abstract 372), contributed by the General Electric Advanced Products Operation, was designed to calculate equilibrium concentrations of fuel cycle isotopes in fast breeder reactors utilizing various recycle schemes. The version submitted was written for the GE635 machine, SCORE2, the Atomics International system developed from the AI-IBM prototype SCORE project, applies computer graphics techniques to assist the cross-section evaluator in analyzing SCISRS and ENDF/B data. This program is written for the IBM 360 computer Model 50 or higher with attached IBM 2250 graphic display unit; it is ACC Abstract 375. The Westinghouse Bettis Atomic Power Laboratory program MO266 was added as ACC Abstract 383. This CDC 6600 program computes the undamped natural frequencies and the mode shapes of lumped-mass linear elastic systems.

During the third quarter of this calendar year a total of 238 computer "program packages" have been distributed--78 in July, 98 in August, and 62 during September.

A third supplement to ANL-7411, the Center's Compilation of Computer Program Abstracts, is being readied for publication. It will

*Lisman, F. L., et al., Burnup Determination of Nuclear Fuels, IN-1277 (1969).

**Kafalas, P., and Crouthamel, C. E., J. Inorg. Nucl. Chem. 4, 239; 5, 92 (1957); reported data are based on a half-life for ^{137}Cs of 32.6 yr.

contain our abstracts numbers 358 through 376. The abstracts for this supplement are being prepared by a computer program developed as a part of the ACCESS programming effort.

B. Reactor Fuels and Materials Development

1. Fuels and Claddings--Research and Development

a. Behavior of Reactor Materials

(i) Fuel Behavior

(a) Fuel-element Modeling Studies (R. W. Weeks and V. Z. Jankus)

Last Reported: ANL-7581, p. 90 (June 1969).

The LIFE fuel-element code is in the final stages of development. The code is written in Fortran IV for the ANL IBM-360 Model 50-75 system. A brief outline of the code model follows.

(1) Fuel-element Geometry

1. The LIFE code treats the fuel element as a right-circular cylinder, loaded externally by coolant pressure and/or end load.

2. Axial symmetry is assumed with a generalized plane-strain treatment.

3. In the mechanical calculations, the fuel is divided into three concentric cylindrical regions (see Temperature Distribution below) representing a central void, the "columnar," "equiaxed," and "undisturbed" regions. A fuel-clad gap is allowed, and the clad is represented by an additional concentric cylinder.

4. The axial elongation of each fuel cylinder is required to be the same, but the axial elongation of the fuel is not necessarily equal to that of the clad. A simple friction coefficient is allowed between the fuel and clad.

5. The initial fuel form is accounted for presently by variations in the initial density, the fuel-clad gap, and the initial central void.

6. Up to ten axial sections are allowed. The plenum is always a single section, regardless of length, whereas each of the fuel sections is of equal length.

7. The central void connects directly with the plenum.

(2) Power Distribution

1. Axial power-distribution factors are included so that the average linear power may vary from section to section.

2. Radial power-distribution factors are included, which may vary with time, to follow the migration of fuel constituents (see Progress Report for April-May 1969, ANL-7577, p. 140).

(3) Temperature Distribution

1. The quasi-static temperature distribution is computed at the beginning of each time step (neglecting specific heat) and is then held constant during the time step.

2. For thermal calculations, the fuel and clad are divided into arbitrary numbers of radial sections (e.g., 40 for the fuel and 6 for the clad).

3. The local coolant temperature is computed from both inlet and outlet coolant temperatures. Heat-transfer coefficients are used at the clad-coolant interface and at the fuel-clad gap. The latter coefficient is a function of pressure.

4. The thermal conductivity of the fuel is considered as a function of temperature and porosity. Clad conductivity is considered a function of temperature only.

5. Linear thermal expansion coefficients are considered as functions of temperature, and average thermal expansions of the clad and each of the three fuel regions are computed by integration.

6. The three fuel-region sizes are determined by the time interval, by an equation representing the velocity of bubble migration via the evaporation-condensation mechanism, by an equation representing the sintering rate of the fuel, and by a mass balance. The net mass transfer between fuel regions is computed. The rate equations are functions of temperature and temperature gradient.

7. No fuel melting is allowed at present.

8. Effects of fuel cracks are not considered at present.

(4) Fission-product Distribution

1. Fission products are generated according to the plutonium-uranium distribution.

2. Presently, complete gas release is assumed in the columnar region, and finite rates of gas release are specified for the equiaxed and undisturbed regions.

3. Solid fission-product migration (though not the rate of migration) is accounted for in the fuel-swelling calculations.

(5) Fuel Swelling

1. The average thermal expansion of each fuel section is computed.

2. The net swelling rate ($\Delta V/V$) of any region due to accumulation of solid fission products is a function of the fission rate, the fuel constituents in the region, and the region size.

3. The net swelling rate of each fuel region due to gaseous fission products is presently taken as

$$\frac{\Delta V}{V_0} = \frac{nR\bar{T}}{(P+PG)\,V_0},$$

where

ΔV = the change in volume of the region,

V_0 = the original volume of the region,

n = the number of moles of gas remaining in the region,

$\bar{T}$ = the average temperature of the gas--assumed equal to the average temperature of the region,

P = $-(\sigma_r+\sigma_\theta+\sigma_z)/3$ where σ_r, σ_θ, and σ_z are the average stresses acting in the region,

$PG \approx 2\gamma/R_{AV}$ where γ is surface tension, and R_{AV} is the radius of the average bubble size in the region,

R = universal gas constant.

4. Simple anisotropy factors are included, but probably will not be used.

(6) Clad Swelling

1. The average thermal expansion of the clad is computed.

2. Clad swelling due to void formation is included in a subroutine based on the theory by Harkness and Li.*

(7) Fuel-clad Interactions

1. An initial fuel-clad gap is specified. This may open or close depending on subsequent operating conditions.

2. A simple coefficient of friction is allowed. When the fuel touches the clad, stick or slip is checked for on each time step and the boundary conditions adjusted accordingly.

3. Fuel-clad incompatibility and coolant-clad corrosion are presently handled only by using an "effective clad thickness."

(8) Failure Criteria. The stress-strain clad-swelling history of the element is traced, but no specific failure criteria have been incorporated. The development of such criteria is in progress.

(9) Code Predictions. Code predictions that can be checked experimentally include:

1. clad inside and outside diameters as functions of irradiation history and axial position;

2. clad length;

3. fuel length;

4. central void and fuel zone sizes as functions of the irradiation history and axial position;

5. gas release to the plenum;

6. radial and axial temperature distribution;

7. plutonium-uranium distribution.

(10) Additional Comments

1. A major feature of the code is that the irradiation, coolant-temperature history of a given fuel element can be traced in a step-wise manner.

*Harkness, S. D., and Li, Che-Yu, "A Model for Void Formation in Metals Irradiated in a Fast Neutron Environment," Proceedings IAEA Symposium on Radiation Damage in Reactor Materials, Vienna, Austria, June 1969.

2. The code formulation includes thermoelastic and creep deformations, and is sufficiently general to include almost any form of creep law and/or stress relaxation behavior.

3. In spite of the crudeness of the models currently incorporated in the LIFE code, an attempt has been made to relate all the model parameters to materials properties that can be measured in independent tests not involving the integral fuel element. (Until values of the required materials properties are established, however, parameter adjustment by code calibration against integral fuel-element behavior will, of course, be necessary.)

4. The code formulation can, and will, be revised to include more sophisticated models as they become available.

5. As might be expected, some serious convergence problems have been encountered in the numerical calculations, and present LIFE code development efforts are focused on improving the convergence of the iterative scheme employed.

b. Chemistry of Irradiated Fuel Materials (C. E. Crouthamel)

(i) Development of Techniques of Fuel Analysis

Last Reported: ANL-7595, p. 94 (July 1969).

Work is in progress to develop a technique for microsampling and analysis of noble fission-product gases retained in irradiated ceramic fuels. Microsampling is accomplished by laser-beam vaporization of selected areas of a fuel sample held in a vacuum chamber; the released fission gases are identified and measured by means of a quadrupole mass spectrometer.

Preliminary measurements have been made of the radial distribution of fission gases in a transverse section of an irradiated UO_2 fuel pin clad with Type 304 stainless steel. The fuel material, which had an overall enrichment of 13%, was produced by blending fully enriched and depleted UO_2 powders. The fuel pin had been irradiated to 6.0 at. % burnup in MTR. The calculated surface and centerline temperatures at the start of the steady-state irradiation were 1350 and 2400°C, respectively. Post-test calculations, based on the behavior of fission gases in other irradiated UO_2 fuels, indicated that the amount of fission xenon and krypton remaining in the fuel was about 0.5 mmol/cm^3 UO_2.

Laser samples of the transverse section were taken in the columnar grain regions and the unrestructured regions of the fuel; the craters produced were 60 to 70 μm in diameter. Fission gas was readily

detectable in both locations. There were indications that the fission-gas concentration was higher, by a factor of two or three, in the outer, unrestructured regions than in the columnar grains. The average concentration of fission gas in samples taken from the columnar grains was about 0.1 mmol/cm^3 UO_2.

Since these results were obtained in a preliminary test of the analytical technique, assessment of their reliability is difficult. However, the test pointed out that several factors need further consideration before the method can be fully evaluated. First, it should be noted that the columnar-grain region of this fuel specimen shows progressively less complete isotopic exchange of ^{235}U and ^{238}U from the central void to the equiaxed-grain region and little or no isotopic exchange in the unrestructured region. These local variations in isotopic composition could lead to local variations in fission-gas concentration that would tend to obscure any systematic trends across the radius of the fuel pin. Additionally, the test revealed inadequacies in the detection system, which may have caused significant systematic errors. In future experiments, the fission gases will be determined by isotope-dilution analysis, a method that is expected to provide increased accuracy and precision. The detection system is presently being modified to accommodate this change.

c. Thermodynamics of Fuel Materials

(i) Vapor Species Partial Pressures in the Ternary U-Pu-C System (P. E. Blackburn and R. K. Edwards)

Last Reported: ANL-7595, p. 95 (July 1969).

Mass-spectrometric studies of the volatilization behavior of the U-Pu-C system are being conducted to determine (1) the composition of the vapor phase in equilibrium with the condensed phase(s), (2) the partial pressures of the vapor species as a function of temperature, and (3) the thermodynamic properties of the vapor species and condensed phases.

The investigation of the binary Pu-C system, which had been undertaken first, was completed and the final results were summarized in ANL-7595. The Pu-C study was carried out with a Bendix time-of-flight mass spectrometer that had been converted to plutonium capability. However, the projected work in the ternary U-Pu-C system, which involves obtaining the relative activities of U/Pu, is to be carried out with the quadrupole mass spectrometer. The higher sensitivity of this instrument is needed to measure with sufficient accuracy the partial vapor pressure of uranium at the same time as that of plutonium (the partial vapor pressure of uranium is anticipated to be much smaller than that of plutonium).

An effusion apparatus, previously used to determine the congruently vaporizing compositions of urania, has been modified in order

that studies may be carried out on the Pu-X and U-Pu-X systems, where X is either carbon or oxygen. As previously used, the apparatus consisted of an ultrahigh-vacuum system in which an induction coil could be used to heat the effusion cell to high temperatures. The principal external modification required was coupling to a glovebox to protect personnel from contamination because of the anticipated radiation hazard. To optimize the information output from the study while also minimizing the time required for experimentation, two internal modifications were designed into the apparatus: (1) a quadrupole-mass-spectrometer sensing probe that can be moved at will during an effusion run, so that it either continuously or periodically intercepts the effusing gas beam; (2) a quartz-crystal sensing head of a microbalance that can also, either continuously or periodically, intercept the effusing gas beam and yield high-sensitivity measurements of the total effusive loss in terms of the effusate condensed. Theoretical analyses as well were directed toward increasing the efficiency of the experiments. It has been established that compositions of the condensed phase can be determined from a mathematical analysis of the mass-spectrometric ion-current data more accurately than from time-consuming chemical analyses.

The mass-spectrometer installation has been completed, and initial testing and calibration runs (with urania materials) are under way. The preliminary performance appears excellent, in particular the temperature constancy of the effusion cell as deduced from the constancy of the species ion currents during congruent effusion. The quartz-crystal microbalance performs satisfactorily in tests external to the effusion apparatus; it will be installed at the appropriate time during the continuation of the testing. Effusion experiments with nonplutonium-bearing materials will begin following critical alignment and calibration of the mass spectrometer and microbalance. Plutonium studies will begin after full plutonium capability for the glovebox has been achieved.

d. Oxide Fuel Studies (L. A. Neimark, F. L. Brown, W. F. Murphy, and E. J. Petkus)

(i) Examination of Group O-2

Last Reported: ANL-7618, p. 95 (Sept 1969).

Dimensional inspection completed the nondestructive phase of the examination of Element SOV-1. This element had received a total burnup in EBR-II of about 4.8 at. % in two increments (3.6 at. % in Subassembly XO11, and 1.2 at. % in Subassembly XO39). The maximum cladding diametral increase of 0.61% (0.0018 in.) occurred slightly below the midplane of the fuel column, and, hence, the midplane of the core. The magnitude of the increase was comparable to that found in companion elements irradiated to 3.6 at. % burnup at a maximum power rating 7% higher (see Progress Report for September 1968, ANL-7500, pp. 2-4). The axial position of the maximum diametral increase in SOV-1 was the same as that for a maximum

diametral increase of 0.53% (0.002 in.) in the irradiation capsule. Fuel Element SOV-1 elongated 0.16% (0.040 in.) and increased in total volume by 0.82%. The fission gas in the element plenum has been analyzed, but the results have not been evaluated.

The metallographic structure of the fuel along the length of the element indicated that the fuel operated in the solid state during its second period in the reactor. Previous examination of the companion elements of SOV-1 in Subassembly XO11 indicated these elements (including SOV-1) had operated with molten centers at linear power ratings upward from 19.6 kW/ft; SOV-1 had operated at 20.1 kW/ft. During the second period of irradiation, SOV-1 operated at an estimated peak of 19.5 kW/ft. The resulting fuel structure showed only little evidence of its once-molten history. At the cold, bottom end of the fuel column the migration of small fission-product inclusions to the center of the element was incomplete, and what is probably the boundary of melting could be distinguished. Higher in the fuel column, the fission products were more dispersed in the columnar-grain region. About 1 in. from the bottom of the column the central void was bridged in three small areas by a material that had a dendritic structure. These areas were evident in the neutron radiographs after 4.8 at. % burnup, but, unfortunately, it could not be determined from the neutron radiograph obtained at 3.6 at. % burnup whether this structure also existed at the time. Presumably this material is a remnant of the first irradiation period when the fuel was molten. Microprobe analysis will be used to determine its nature.

(ii) Preparation of Group O-3

Last Reported: ANL-7618, pp. 95-96 (Sept 1969).

Eight of the 18 pellet and vibratorily compacted mixed-oxide fuel elements have been encapsulated. Eddy-current examination for sodium-bond integrity and X-radiography of the top end-plug weld are under way on the eight capsules.

The Experiment Description and Safety Evaluation has been prepared and sent to the EBR-II Project. An addendum to this document, which will be provided later, will describe the encapsulation and sodium-bonding procedures, and will provide the quality assurance records for the capsules.

2. Radiation Damage on Structural Materials--Research and Development

Last Reported: ANL-7561, pp. 58-60 (March 1969).

a. Effect of Flowing Sodium on the Creep of Vanadium Alloys (F. L. Yaggee)

The low fracture strain (about 0.8% in 495 hr) previously reported for two V-15 wt % Cr-5 wt % Ti alloys

sodium at 650°C is believed to be the result of cracks occurring in the specimen material prior to creep testing.

The specimens possessed an unusual thermomechanical history. The alloy was initially supplied as 0.060-in.-thick sheet-bar in the 50% cold-worked condition. After a 1-hr, 1250°C property-optimizing heat treatment in vacuo, the sheet-bar was subsequently annealed for 1 hr at 900°C in vacuo and rolled to a final thickness of 0.020 in. The material was then subjected to a second property-optimizing heat treatment for 1 hr at 1250°C. An unusual amount of edge cracking was observed during the rolling operation following the first heat treatment. Likewise, the material appeared quite brittle during the machining operation following the second heat treatment.

Metallographic examination of the two V-15 wt % Cr-5 wt % Ti specimens revealed a random distribution of cracks throughout the specimens, oriented perpendicular to the direction of the applied tensile load. A similar distribution and orientation of cracks, though somewhat smaller in size, were also observed in specimens that had not been creep tested. In short-term tensile tests at 25, 200, 400, and 600°C, these specimens exhibited a much lower total elongation and reduction in area than might be expected of this alloy when given a single property-optimizing heat treatment following the final reduction pass. The ultimate tensile strength was lowered only slightly by the double heat treatment.

The V-15 wt % Cr-5 wt % Ti and V-15 wt % Ti-7.5 wt % Cr alloys both exhibited atomic ordering after a property-optimizing heat treatment of 1 hr at 1250°C. Apparently this ordering cannot be erased by a 1-hr anneal at 900°C, and, therefore, further mechanical working after a property-optimizing heat treatment is detrimental. It is concluded that all mechanical working of these alloys must be completed before heat treatment to optimize the mechanical properties.

b. Irradiation Studies of Cladding Alloys (R. Carlander)

Not previously reported.

ANL Capsule A61 was loaded into EBR-II Subassembly XO18B for irradiation to an estimated fluence of 3.5×10^{22} n/cm^2 (total). The capsule contained tensile and creep specimens of V-15 wt % Cr-5 wt % Ti alloy. The effects of fluence, temperature, grain size, and uniaxial versus biaxial stress rupture on the postirradiation mechanical properties of V-15 wt % Cr-5 wt % Ti alloy will be studied. The specimen identifications and test conditions are presented in Table III.B.1.

TABLE III.B.1. Specimen Identification and Environmental Conditions of V-15 wt % Cr-5 wt % Ti Alloy in ANL Capsule A61

Specimen No.	Type of Specimen	Average Grain Diameter (μ)	No. of Specimens	Irradiation Temperature (°C)	Fluence Range n/cm^2 (Total)
01-06	Uniaxial	10	6	410	0.5-2
07-011	Uniaxial	10	5	650	2-4
012-018	Uniaxial	10	7	371	0.5-2
R1-R5	Uniaxial	20	5	410	0.5-2
R6-R9	Uniaxial	20	4	650	2-4
R10-R16	Uniaxial	20	7	371	0.5-2
P1-P5	Uniaxial	35	5	410	0.5-2
P6-P10	Uniaxial	35	5	650	2-4
P11-P17	Uniaxial	35	7	371	0.5-2
AO, AR, AP	Biaxial	20	12	410	0.5-2
BO, RB, BP	Biaxial	20	6	650	2-4
CO, CR, CP	Biaxial	20	6	650	2-4
DO, DR, DP	Biaxial	20	12	371	0.5-2

c. In-Reactor Creep Studies (J. A. Tesk and S. D. Harkness)

Not previously reported.

A model concerning possible effects of neutron irradiation on climb-controlled creep in austenitic stainless steel is being developed. The model involves modification of the theory of Ansell and Weertman* to include the effects of the interaction of neutron-generated interstitials and vacancies with dislocations. At present, the solution of the diffusion equation in the presence of a neutron flux results in an expression for the steady-state in-reactor creep rate at high stresses as

$$\epsilon \cong A_1 L \sigma^2 \left[A_2 D_s e + \frac{\sigma^2 b^2 L}{\mu k T} + b^2 J_{xs} \right],$$

where

A_1, A_2 are constants,

σ = the applied stress,

L = the average distance between barriers,

D_s = the self-diffusion coefficient,

b = the Burgers vector,

J_{xs} = the excess interstitial flux arriving at dislocations.

J_{xs} is a function of grain size, precipitate size and distribution, dislocation density, and all other possible sinks, such as voids and dislocation

*Ansell, G. S., and Weertman, J., Creep of a Dispersion-Hardened Alloy, Trans. Met Soc. AIME 215, 838 (1959).

loops. Under some conditions, i.e., high dislocation density or small grain size, J_{xs} is roughly proportional to the neutron flux for a given neutron spectrum. J_{xs} is computed by using the computer program of Harkness.*

Precipitation-hardened alloys are expected to show a second-power stress dependence for in-reactor climb-controlled creep at moderate to high stresses under flux conditions capable of producing appreciable steady-state vacancy and interstitial supersaturations.

C. Engineering Development--Research and Development

1. Instrumentation and Control

a. Boiling Detector (T. T. Anderson)

(i) Acoustic Method

(a) Boiling-sodium Spectra in Simulated Reactor Geometries (T. T. Anderson)

Last Reported: ANL-7581, p. 102 (June 1969).

It is proposed to place acoustic sensors directly into a sodium environment to improve the resolution of prototype acoustic boiling detectors. This could be achieved with the existing 1150°F Gulton accelerometers that were specially ordered for sodium-immersion service. Use of these accelerometers in the CCTL sodium flowtests of the Mark-II FFTF subassembly is being considered.

(b) Irradiation and Resistance Tests of Piezoelectric and Insulator Materials (T. T. Anderson and S. L. Halverson)

Last Reported: ANL-7618, p. 106 (Sept 1969).

Irradiation of lithium niobate with high-energy electrons (1-2.2 MeV) from the Van de Graaf accelerator will resume in November; scheduling difficulties delayed further tests in September and October. Electronic test apparatus has been set up to obtain more complete characterization of the lithium niobate during electron bombardment: (1) direct measurements of crystal impedance, whose magnitude and phase at radiofrequencies of 0.1-32 MHz are plotted on an X-Y recorder, and (2) swept-frequency scans of the crystal-transducer sensitivity to incident acoustic

*Harkness, S. D., and Li, Che-Yu, "A Model for Void Formation in Metals Irradiated in a Fast Neutron Environment," Proceedings IAEA Symposium on Radiation Damage in Reactor Materials, Vienna, Austria, June 1969.

energy, which permits an X-Y recording of transducer sensitivity versus frequency to be made during irradiation for both sonic and ultrasonic waves induced in the test fixture.

(c) Development of High-temperature Detector (A. P. Gavin)

Last Reported: ANL-7581, pp. 99-100 (June 1969).

A test rig has been constructed for evaluating use of lithium niobate in high-temperature transducers. The rig consists of a 0.5-in.-dia stainless steel rod that transmits acoustic energy into a tubular furnace cavity, a nickel rod attached to the stainless steel rod to reduce thermal gradients, and a clamp assembly for spring-loading the crystal against the end of the nickel rod.

(d) Tests of High-temperature Detectors in Water, Furnace, and Sodium (A. P. Gavin)

Last Reported: ANL-7581, pp. 99-100 (June 1969).

A furnace has been constructed for use in subjecting lithium niobate crystals to the combined effects of gamma radiation and temperature. The furnace design (1) minimizes gamma attenuation, (2) fits within the limited space in the gamma facility, (3) does not require forced-air cooling, (4) minimizes electrical pickup noise from the heater, and (5) maintains sodium-environmental temperatures without disturbing the gamma test-cell components.

The furnace consists of a central stainless steel tube, with nichrome ribbon noninductively wound over it, and surrounded by concentric radiation shields. The furnace has a 1-in. ID, 3-in. OD, and 12-in. length, and weighs 1 lb; it can produce a centerline temperature on the test fixture of 1500°F and an outside surface temperature of 300°F without forced cooling.

2. Heat Transfer and Fluid Flow

a. LMFBR Burnout Limitations (R. J. Schiltz and R. Rohde)

Last Reported: ANL-7606, pp. 104-105 (Aug 1969).

(i) Preparation of Apparatus. Documents are being prepared for safety and quality-assurance reviews. The 1.5-in. valves are being repaired and upgraded.

Welding of the main loop piping is about 10% complete. Precautions are being taken to ensure quality welding. A sample weld

joining a Type 304 stainless steel transition piece to the cast Type 347 stainless steel body of a 1.5-in. valve was made with the gas tungsten-arc process. Although the weld filler metal specified was Type 309 stainless steel-Cb wire and the requested procedure was ANL-CS-1001 (consumable insert), the unavailability of 1/8-in.-dia weld wire of Type 309 stainless steel-Cb for the fabrication of the consumable inserts led to changing the welding process to procedure ANL-CS-1007, which in turn led to (a) elimination of the consumable insert, (b) reducing the weld groove land from 1/16 to 1/32 in., and (c) greater current and weld wire fed into the root pass, obtaining full penetration. The sample weld was accepted by the safety committee, and approval was given for welding the remaining valves, with the requirement that the weld areas all be radiographed both before and after welding.

Welding procedure ANL-CS-1001, with Type 308 stainless steel consumable inserts and filler wire, is being used in welding the loop piping. Inspection consists of dye-penetrant testing of all root and final passes with 100% radiography of the final welds. All blind root passes and the final weld are being radiographed. All final welds are also being vacuum-leakchecked.

(ii) Analytical Prediction of Burnout Limitations

Last Reported: ANL-7518, pp. 97-99 (Nov 1968).

In ANL-7518 equations were presented for the computation of choked flowrates for the escape of sodium coolant through a constant-area channel. A computer program has been developed to investigate the solutions resulting from these equations for various proposed slip models, including the Fauske ($s = \sqrt{v_g/v_f}$) and Martinelli-Lockhart slip models. The resulting computed critical flows for the pressure range of interest (20-40 psia) and for qualities up to x = 0.1 are compared in Fig. III.C.1 with the critical flows based on the homogeneous flow model (slip s = 1). As expected, the Fauske and Martinelli slip models result in critical flows significantly higher than the homogeneous flow model. For higher qualities (above x = 0.05), the Fauske and Martinelli slips result in approximately the same critical flow as shown in Fig. III.C.1 for x = 0.01. The divergence becomes more pronounced as the pressure increases. Also, for purposes of comparison, critical flows (for x = 0.01) were computed based on the modified Armand formula for void fraction* and for the modified Balzhiser void-fraction correlation.**

The computations for the critical flows shown in Fig. III.C.1 are based on the physical properties of sodium given by MacFarlane.** These values are slightly higher than the values computed by Fauske;* the

*Fauske, H. K., Two-phase Critical Flow with Application to Liquid-metal Systems (Mercury, Cesium, Rubidium, Potassium, Sodium, and Lithium), ANL-6779 (Oct 1963).

**MacFarlane, D. R., An Analytic Study of the Transient Boiling of Sodium in Reactor Coolant Channels, ANL-7222 (June 1966).

differences are probably caused by the different physical properties used by Fauske, who used those given by Weatherford.*

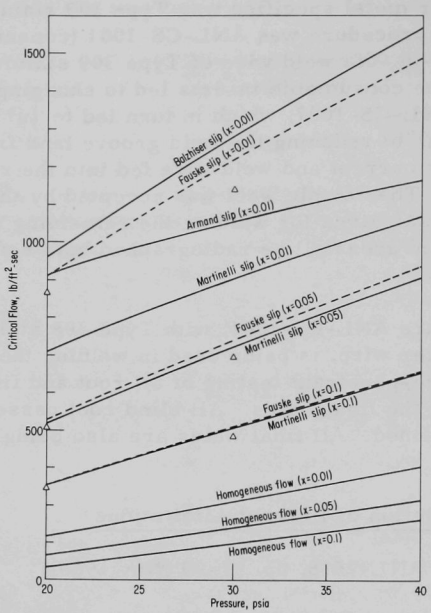

Fig. III.C.1

Computed Critical Flowrates for the Fauske and Martinelli Slip Models Compared with the Homogeneous Flow Model for Sodium (points computed by Fauske in ANL-6779 are indicated by Δ)

b. Nonboiling Transient Heat Transfer (R. P. Stein)

Last Reported: ANL-7606, pp. 105-108 (Aug 1969).

(i) Analyses of Heat-flux Transients. For a circular tube, the relationship to account for forced-convection heat transfer during wall-heat-flux transients (that was reported in ANL-7606 for a generalized annular duct) becomes

$$t_s - t_B = \frac{q}{h} + \frac{D}{2k}\left[R_1\left(\frac{\partial q}{\partial z} + \frac{\partial}{\partial \theta}\right) + R_2\left(\frac{\partial^2 q}{\partial z^2} + 2\,\frac{\partial^2 q}{\partial z \partial \theta} + \frac{\partial^2 q}{\partial \theta^2}\right)\right.$$

$$\left. + R_3\left(\frac{\partial^3 q}{\partial z^2} + 3\,\frac{\partial^3 q}{\partial z^2 \partial \theta} + 3\,\frac{\partial^3 q}{\partial z \partial \theta^2} + \frac{\partial^3 q}{\partial \theta^2}\right) + \ldots\right], \qquad (1)$$

where R_1, R_2, R_3, and β are dimensionless coefficients that are functions of Reynolds and Prandtl numbers (but are independent of θ and z), t_s = surface temperature of wall, t_B = fluid bulk temperature, q = heat-flux density from wall, h = fully developed heat-transfer coefficient for case of q uniform

*Weatherford, W. D., Jr., Tyler, J. C., and Ku, P. M., Properties of Inorganic Energy-Conversion and Heat Transfer Fluids for Space Applications, WADD TR61-96 (Nov 1961).

and steady, z = dimensionless axial distance = $\beta(\ell/D)$, ℓ = axial distance, D = hydraulic equivalent diameter, θ = dimensionless time = $\beta(\bar{u}\tau/D)$, $\bar{u}$ = average fluid velocity, τ = time, and k = fluid thermal conductivity.

Values of β and the coefficients R_k are listed in Table III.C.1. The values are based on the use of von Karman's universal velocity profile with eddy diffusivities for heat transfer equal to those for momentum transfer and uniform at their maximum values in the central region of the duct.

TABLE III.C.1. Values of Coefficients for Circular Tube

Re	Pr	β	$-R_1$	R_2	$-R_3$
10^4	0.00316	1.942	0.164	0.149	0.145
	0.01	0.727	0.146	0.131	0.128
	0.0316	0.343	0.110	0.978	0.949
	1.0	0.166	0.0104	0.00900	0.00862
3.16×10^4	0.00316	0.706	0.147	0.133	0.130
	0.01	0.319	0.113	0.102	0.0992
	0.0316	0.195	0.0674	0.0602	0.0583
	1.0	0.138	0.00368	0.00327	0.00315
10^5	0.00316	0.302	0.117	0.106	0.103
	0.01	0.178	0.0722	0.0648	0.0628
	0.0316	0.138	0.0334	0.0299	0.0289
	1.0	0.119	0.00135	0.00120	0.00116
3.16×10^5	0.00316	0.165	0.0764	0.0688	0.0668
	0.01	0.124	0.0364	0.0326	0.0316
	0.0316	0.112	0.0138	0.0124	0.0120
	1.0	0.106	0.000482	0.000432	0.000417
10^6	0.00316	0.114	0.0392	0.0352	0.0341
	0.01	0.101	0.0151	0.0136	0.0131
	0.0316	0.0968	0.00516	0.00463	0.00448
	1.0	0.0949	0.000169	0.000152	0.000147

Coefficients that will pertain to an approximation of a pin bundle are being computed. The approximation considers each pin to be surrounded by an equivalent annular space with turbulent velocities and eddy diffusivities corresponding to a zero shear condition at a fictitious outer wall.

A research plan has been prepared for further work. Part of the research will be performed as a doctoral dissertation under the AUA-ANL fellowship program. It will include further analytical investigations and experiments with sodium. The analytical investigations will include an attempt to obtain engineering-prediction relationships for cases

with flow transients. The objectives of the experiments are to verify the engineering relationships developed and to determine or confirm the coefficients that appear in these relationships. For example, for a circular tube with a linear heat flux in time and uniform in space, the only coefficient that appears in Eq. (1) is R_1, and an experiment with such a heat flux should allow determination of R_1. According to Eq. (1), the same information should also be obtained from a steady-state experiment with an axially linear heat flux.

Three facilities have been considered for the experiments: (a) the sodium-sodium heat exchanger loop (see Progress Report for February 1968, ANL-7427, p. 114), (b) the LMFBR "Burnout Limitation" loop (see Progress Report for September 1968, ANL-7500, p. 106), and (c) another loop used for the Flow-Coastdown Experiment (see Progress Report for September 1968, ANL-7500, p. 125). The first two loops use sodium; the flow-coastdown equipment will use NaK. Of the three facilities, only the sodium-sodium heat exchanger loop has been built and operated. The other two will be under construction for several months. The sodium-sodium heat exchanger test equipment seems to be the best alternative for these experiments, but will require modification to make it meet present stringent LMFBR requirements related to quality assurance and safety. Also, the present test section must be replaced with one in which the heat flux to the sodium can be measured carefully. Heaters will be installed in the test section; electrical-resistance heaters that can be electrically insulated from the test section wall, and electron-bombardment heaters, are being considered.

c. Electron-Bombardment-Heater (EBH) Development
(R. D. Carlson)

Last Reported: ANL-7577, pp. 164-165 (April-May 1969).

(i) Tests with Single Pin (1/4-in. OD x 36 in.)

Not previously reported.

Because most current design studies indicate that the probable LMFBR fuel-pin geometry will be 1/4-in. OD by 36-in. long with 0.040-in. spacing, the primary emphasis in the development of the EBH has been shifted to that heater geometry.

Figure III.C.2 shows the apparatus that has been designed and is being constructed to test 1/4-in.-OD x 36-in.-long pins in sodium at up to 1000°F. This apparatus will allow testing such pins to heat fluxes greater than 5×10^6 Btu/hr-ft^2 without the need of building a high-temperature sodium loop for that purpose. The 1/4-in.-OD EB-heated pin will be surrounded with a 1/16-in. annulus of stagnant sodium that is contained in a 3/8-in.-dia, 0.005-in.-wall stainless steel tube that is brazed to a copper

block. The heat generated by the EB-heated pin will be conducted through the sodium, the stainless steel tube, and the copper to the water cooling jacket. The total amount of sodium required for this test is only 31 g. When the heat flux to the sodium is 5×10^6 Btu/hr-ft^2, the heat flux to the water will be less than 5×10^5 Btu/hr-ft^2. Thermocouples placed on the 3/8-in. stainless steel tube will determine the uniformity of the heat flux. The whole apparatus will be placed inside the vacuum chamber now being used for testing electron-bombardment heaters.

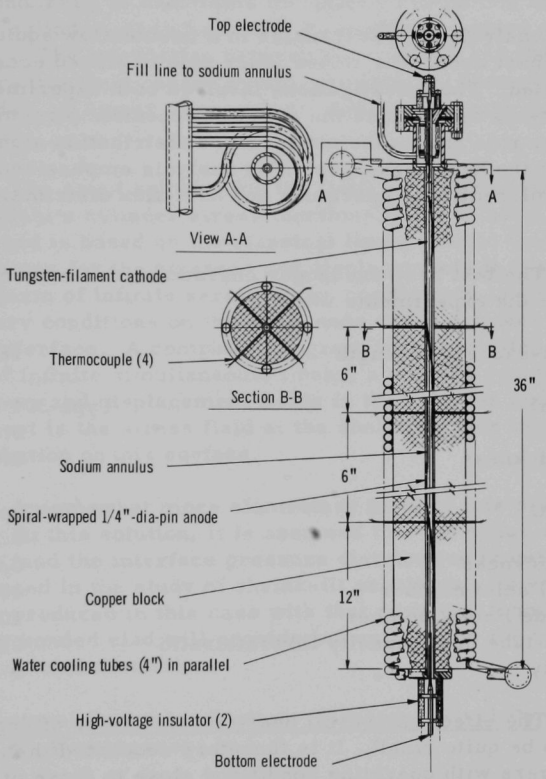

Fig. III.C.2. Apparatus for Testing 1/4-in.-OD by 36-in.-long Electron-bombardment-heated Pins in Sodium at up to 1000°F

(ii) Preparation of 7-pin Cluster (1/4 in. OD x 36 in.)

Not previously reported.

Test sections for clusters of 1/4-in.-OD by 36-in.-long pins are being designed. These clusters will have a 36-in.-long heated length to mockup the core fuel section and an 18-in.-long unheated length

to mockup the upper blanket section. The test section is sized to accommodate 7- and 19-pin clusters. Instrumentation to measure temperature, pressure, void fractions, and rate of voiding in these bundles is being considered.

d. Heat Transfer in Liquid-Metal Heat Exchangers (R. P. Stein)

Last Reported: ANL-7513, p. 114 (Oct 1968).

Analysis of heat transfer in a counterflow sodium-to-sodium double-pipe heat exchanger whose inner pipe is placed eccentrically has been completed. The investigations involved both experiments and analysis. The experiments determined the effect of eccentric placement on the overall heat-transfer rate and on the temperature distribution along and around the outer pipe of the heat exchanger. The analysis emphasized determination of the circumferential temperature and heat-flux distributions at the inner-pipe wall.

The test heat-exchanger characteristics and range of operating conditions of the experiments were:

Active heat-exchanger length	18 in.
Outer pipe	
Material	Type 304 stainless steel
OD	0.625 in.
Wall thickness	0.020 in.
Inner pipe	
Material	70/30 Cupro-nickel
OD	0.375 in.
Wall thickness	0.012 in.
Tube-side Peclet number	400-680
Annulus-side Peclet number	100-670
Annulus-to-tube heat capacity flowrate ratio	0.5-4.0
Eccentricity	0-100%

The effect on overall heat-transfer rates of eccentric placement was found to be quite small. It is therefore concluded that, for liquid-metal heat exchangers with operating conditions close to those of the experiments, practical engineering-design calculations can ignore the effect of eccentricity on overall heat-transfer rates. However, the effect of eccentric placement on circumferential-temperature and heat-flux distributions was found to be large. Thus, engineering-design calculations related, for example, to thermal-stress considerations, cannot ignore the effects of eccentricity.

A report describing the investigations has been drafted.

3. Engineering Mechanics

a. Advanced Thermoelasticity (R. A. Valentin)

Last Reported: ANL-7606, pp. 109-110 (Aug 1969).

(i) Solution of End-effect Problems Involving Nonplane Stress Fields in Short Cylinders and Contact Stresses between Cladding and Fuel. An analysis is underway to determine the axially symmetric deformation of a solid circular cylinder, of finite length ℓ_c, perfectly bonded to a thin shell of length $\ell_s > \ell_c$. The interaction between the cylinder and the shell results from the temperature field caused by uniform internal heat generation within the cylinder. A linear temperature variation through the shell thickness is assumed.

The exact solution for the finite cylinder is obtained with the aid of Youngdahl's cylinder stress functions. The solution for the shell is approximate and is based on the classical linear elastic theory of thin shells. Expressions for the stresses and displacements in the cylinder are obtained in the form of infinite series whose coefficients are determined from the boundary conditions on the plane ends of the cylinder and at the cylinder-shell interface. A computer program will be written to solve the resulting sets of infinite simultaneous, linear, algebraic equations and to evaluate the stress and displacement fields in the cylinder and shell. Of particular interest is the stress field at the shell-cylinder interface and the shear distribution on this surface.

A somewhat more elementary form of this problem is nearing completion. In this solution, it is assumed that the shear stress is identically zero, and the interface pressure distribution is determined by a method often used in the study of shrink-fit problems. Comparison of the deformation produced in this case with that resulting from the solution for the perfectly bonded clad will provide information on the importance of shear forces in clad distortion.

b. Structural Dynamics Studies--Structure-Fluid Dynamics (M. W. Wambsganss, Jr.)

(i) Flowtest Single Cylinder

Last Reported: ANL-7581, pp. 103-105 (June 1969).

A series of flowtests involving a single-cylindrical element in parallel-flow has been planned. Rod displacement and wall pressure fluctuations will be measured. The objective of the tests will be to determine the effect of various flow spoilers on the vibrational response of the rod; an attempt will be made to characterize the various flow spoilers by a pressure

measurement. Theoretical considerations will be employed, and predicted response, based on the characterization of the particular flow spoiler, will be correlated with rms displacement data. Initiation of these tests is being delayed until a suitable acoustic filter is devised for the structural dynamics test loop. The filter is required to obtain meaningful pressure measurements.

(ii) Preparation of Two Structural-Dynamics Test Loops (B. L. Boers and P. L. Zaleski)

Last Reported: ANL-7606, pp. 110-111 (Aug 1969).

Construction activity on the large test loop is essentially complete. All welds have been inspected and found satisfactory; the hydrostatic pressure test has also been performed. When the supplier delivers the control valve, the loop will be operated and its flow characteristics measured.

Work is continuing on the development of a filter to attenuate satisfactorily the low-frequency acoustic disturbances present in the small test loop. Such an acoustic filter probably also can be adapted for use on the large test loop.

(iii) Effect of Initial Curvature on Stability of Tube in Parallel Flow (S. S. Chen)

Last Reported: ANL-7618, pp. 110-111 (Sept 1969).

A topical report on the vibration and stability of a tube conveying fluid has been drafted. The report considers the problems of free vibration, forced vibration, parametric response, and the effects of initial curvature and the Coriolis force.

D. Chemistry and Chemical Separations*

1. Fuel Cycle Technology--Research and Development

a. Molten Metal Decladding

(i) Engineering Design, Analysis, and Evaluation (R. D. Pierce)

Last Reported: ANL-7618, pp. 112-113 (Sept 1969).

A liquid-metal-decladding process is under investigation as a head-end step for the processing of irradiated LMFBR fuels by the aqueous solvent-extraction method. A conceptual design study of a

*Sodium Chemistry--Research and Development is reported in Sect. I.C.

liquid-metal plant capable of processing 5 tonnes/day of stainless steel-clad LMFBR oxide fuel (see ANL-7618) specifies that two decladding vessels be used alternately on a 24-hr-on, 24-hr-off cycle. As an alternative, a continuous decladding concept has been explored that provides for extended continuous use of a single decladding vessel. In the operation of the conceptual continuous decladder (which has the same basic design as the batch decladders), baskets containing fuel assemblies are introduced through five ports into baskets in the molten zinc; after decladding is complete, the baskets, now containing fuel, are removed. These operations are done on a staggered schedule to optimize the use of the cranes and cell space. In addition, zinc solution is continuously pumped from the decladder, and make-up zinc is continuously added as particulate metal (to avoid the use of vessels for liquid-zinc makeup). The zinc solution is pumped to a mixer-settler, where it is contacted with molten salt to remove fuel fines. If necessary, the zinc solution is filtered to remove steel constituents before it is recycled to the decladder. The molten salt may also be recycled to the decladding vessel as the cover layer for suppression of zinc vapor and as a partial trap for iodine.

(ii) Engineering Development (R. D. Pierce)

Last Reported: ANL-7618, p. 114 (Sept 1969).

(a) Decladding Rates. Complete analytical results have been obtained for an experiment (see Progress Report for June 1969, ANL-7581, pp. 109-110) to evaluate Sb-18 at. % Cu alloy as a decladding solvent for Type 304 stainless steel. A 1-hr exposure at 900°C of a stainless steel coupon attached to an agitator revealed a dissolution rate more than ten times the rate for a Type 304 stainless steel coupon exposed to zinc at 800°C in the same manner. Although zinc has been tentatively selected for the reference flowsheet because of its low cost and compatibility with graphite construction material, Sb-Cu alloy appears to be an excellent backup decladding solvent.

(b) Materials Evaluation. Evaluation continued of the corrosion resistance of the 6-in.-dia graphite crucible coated with 30 mils of vapor-deposited tungsten (see Progress Report for July 1969, ANL-7595, p. 114). An alloy of Zn-29 at. % Mg and a salt mixture of $MgCl_2$-30 mol % NaCl-20 mol % KCl-3 mol % MgF_2 were added to the crucible, and stirred for 96 hr at 750°C. The salt and metal were poured out of the crucible, sampled, and analyzed. The salt and metal phases contained 38 and 187 ppm tungsten, respectively, continuing the downward trend in tungsten pickup in this series of experiments with one crucible. The probable source of the tungsten is a small amount of loosely adherent coating.

(iii) Behavior of Volatile Fission Products (R. D. Pierce)

Last Reported: ANL-7618, p. 115 (Sept 1969).

(a) Laboratory Process Development. In the present pyrochemical decladding concept, the stainless steel cladding of LMFBR fuel assemblies is to be dissolved in molten zinc at 800°C. (This procedure is also applicable to the removal of Zircaloy cladding.) A cover salt is proposed to suppress zinc vaporization. Fluoride cover salts are preferred over chlorides to avoid any possibility that residual chloride might contribute to corrosion in the aqueous dissolution step, which follows decladding. Of eight fluoride cover-salt systems considered, the LiF-35 mol % NaF-10 mol % CaF_2 eutectic was selected for initial experiments. This eutectic has an acceptably low melting point and can be easily purified. The distribution of iodine among metal, salt, and gas phases released during the decladding step will be investigated.

2. General Chemistry and Chemical Engineering--Research and Development

a. Thermophysical Properties

(i) Phase Diagram Study of the Ternary System U-Pu-O (P. E. Blackburn and A. E. Martin)

Last Reported: ANL-7581, pp. 111-112 (June 1969).

The study of the U-Pu-O ternary system is currently focused on the establishment of the hypostoichiometric boundary of the fluorite phase, $(Pu_y, U_{1-y})O_{2\pm x}$, at high temperatures at several sections through the system. This is being done by equilibrating liquid uranium-plutonium alloys with uranium-plutonium oxide crucibles for oxygen. As was reported in ANL-7581, a detailed examination of the products of one of the equilibrations by means of an electron-probe microanalyzer (EPM) disclosed some of the problems inherent in the use of this method in the ternary system. It seemed likely, however, that satisfactory equilibrations could be achieved during two-stage processes of equilibration.

The two-stage equilibration technique (see ANL-7581) has now been applied successfully in six experiments at five temperatures from about 1860 to about 2170°C. The oxygen analyses of the crucibles from these equilibrations, expressed in oxygen-to-metal ratios, i.e., $O/M = O/(U+Pu)$, are plotted versus temperature in Fig. III.D.1. The data define the hypostoichiometric boundary of the fluorite phase at 19.8 at. % Pu, the composition of the mixed oxide powder from which the crucibles were formed. (As used here, at. % Pu is the atomic per cent of plutonium with respect to the two major cationic constituents, i.e., at. % Pu = $[Pu/(U+Pu)] \times 100$. Thus, oxygen and all impurity elements are not included in the expression.) For reference

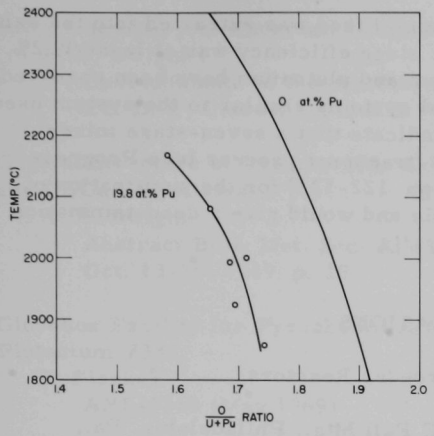

Fig. III.D.1. Hypostoichiometric Boundary of the Fluorite Phase in the U-Pu-O System at High Temperatures at 0 and 19.8 at. % Pu

purposes, the data from the U-UO_2 system,* which can be considered to be at a section through the ternary system where the at. % Pu is zero, are included in Fig. III.D.1. Thus, it is apparent that the hypostoichiometric boundary at 19.8 at. % Pu is more hypostoichiometric than the boundary at 0 at. % Pu by 0.17 to 0.20 O/M units in the temperature range of this study.

Before the above experiments were carried out, it was necessary to establish the direction of the tie lines in the two-phase field under study at the temperatures of the planned experiments. This was accomplished by the EPM examination of alloys and oxide growths formed between the alloys and oxide crucibles in relatively short-term tests at temperatures of interest. The tie-line directions were found to be essentially independent of temperature. For example, the alloy compositions for proper equilibration with crucibles with 19.8 at. % Pu ranged from 10.5 at. % Pu at 1860°C to 10.9 at. % Pu at 2170°C.

b. Liquid Metal-Salt Technology

(i) Liquid Metal-Salt Contactors (R. D. Pierce)

Last Reported: ANL-7606, p. 117 (Aug 1969).

Operating characteristics of a single-stage mixer-settler for the contacting of molten metal with liquid salt at high temperature have been determined, and a run has been performed in which cerium was transferred from Mg-Cu alloy to a halide salt to measure the stage efficiency of the mixer-settler. The pump output was determined as a function of pump speed and the relative levels of metal and salt in the mixer.

The experimental procedure for determining stage efficiency of the mixer-settler consisted of equilibrating $MgCl_2$-30 mol % NaCl-20 mol % KCl-2 mol % MgF_2 with Mg-33 at. % Cu alloy containing cerium and ^{141}Ce tracer. In the initial run, the temperature was 675°C, the speed of the 3-in.-dia paddle was 785 rpm, the salt flow was 25 cm^3/sec, the metal flow was 17 cm^3/sec, the salt-to-metal ratio was 1.5, and the residence time in the mixing chamber was 20.5 sec. The effluent metal from the settling chamber was sampled and analyzed. Preliminary results

*Edwards, R. K., and Martin, A. E., Thermodynamics, Vol. 2, Proc. Symp. Vienna, 1965, IAEA, Vienna (1966). p. 423.

show that 99.2% of the cerium in the metal feed was extracted into the salt in the mixing chamber; therefore, the stage efficiency was at least 99.2%. Rates of extraction into salt for cerium and plutonium have been observed to be similar* in work with salt-metal systems similar to the system used in this investigation. These results indicate that a seven-stage mixer-settler proposed in the reference salt-transport process (see Progress Report for October 1968, ANL-7513, pp. 122-123) for the purification of plutonium would be technically feasible and would give a decontamination factor of 10^6.

PUBLICATIONS

Acoustic Boiling Detection in Fast Breeder Reactors
T. T. Anderson and F. H. Just
Abstract Bull. Met. Soc. AIME Fall Mtg., Philadelphia, Pa., Oct. 13-16, 1969, p. 170

Vibratory Compaction: III, Rate of Entry
J. E. Ayer and F. E. Soppet
J. Am. Ceram. Soc. 52, 414-416 (August 1969)

Neutron Image Intensifier
H. Berger
Encyclopaedic Dictionary of Physics, Suppl. Vol. 3 (1968)

Neutron Image Storage
H. Berger
Encyclopaedic Dictionary of Physics, Suppl. Vol. 3 (1968)

Some Experiments in Fast Neutron Radiography
H. Berger
Abstract Bull. Met. Soc. AIME Fall Mtg., Philadelphia, Pa., Oct. 13-16, 1969, p. 61

Fast Neutron Capture by Vanadium and Titanium
N. D. Dudey, R. R. Heinrich, and A. A. Madson
J. Nucl. Energy 23, 443-456 (1969)

Application of Activation Analysis and Ge(Li) Detection Techniques for the Determination of Stable Elements in Marine Aerosols
N. D. Dudey, L. E. Ross, and V. E. Noshkin**
Modern Trends in Activation Analysis, Proc. 1968 Int. Conf., Gaithersburg, Md., October 7-11, 1968. U.S. Dept. Commerce, Nat. Bur. Std. Spec. Publ. 312, Washington, June 1969, pp. 55-61

*Walsh, W., Argonne National Laboratory, private communication (Sept 1966).
**Woods Hole Oceanographic Institute.

Alloy Chemistry of Thorium, Uranium, and Plutonium Compounds
A. E. Dwight
Developments in the Structural Chemistry of Alloy Phases, Ed. B. C. Giessen. Plenum Press, New York, 1969, pp. 181-226

Crystal Structure of Intermetallic Compounds in the $U(Co,Ga)_2$, $U(Ni,Ga)_2$ and $(U,Cu,Ga)_2$ Alloys
A. E. Dwight
Abstract Bull. Met. Soc. AIME Fall Mtg., Philadelphia, Pa., Oct. 13-16, 1969, p. 10

Glovebox Facility for Pyrochemical Research and Development Work with Plutonium-238
J. Fischer
ANL-7568 (May 1969)

Displacement-Transducer Assembly Used in Studying the Parallel-Flow-Induced Vibration of Reactor Fuel Rods
J. A. Jendrzejczyk and M. W. Wambsganss
J. Acoust. Soc. Am. 46(3), 826-827 (Sept 1969) Letter

Determination of the Fast Fission Yield of ^{141}Pr Using Neutron Activation Analysis
R. P. Larsen, K. K. S. Pillay, and R. J. Meyer
J. Radioanal. Chem. 3, 233 (1969)

Fast-Neutron Scattering from Germanium
D. B. Lister and A. B. Smith
Phys. Rev. 183, 954-963 (July 20, 1969)

Mass Transfer Diffusion Mechanisms and Cobalt Oxide
P. S. Maiya and W. K. Chen
Abstract Bull. Met. Soc. AIME Fall Mtg., Philadelphia, Pa., Oct. 13-16, 1969, p. 78

Analog Fine Structure and Asymmetry
P. A. Moldauer
Nuclear Isospin, Proc. 2nd Conf., Pacific Grove, Calif., March 13-15, 1969, Ed. J. D. Anderson. Academic Press, New York, 1969, pp. 415-419; also Bull. Am. Phys. Soc. 14, 961 (Oct 1969) Abstract

Averaging Methods in Nuclear Reaction Theory
P. A. Moldauer
Phys. Rev. Letters 23, 708-711 (Sept. 29, 1969)

Microanalysis of Highly Radioactive Reactor Fuels
R. Natesh, B. J. Koprowski, and E. M. Butler
Proc. Fourth National Conf. on Electron Microprobe Analysis, Calif. Inst. Technol., Pasadena, Calif., July 16-18, 1969, Paper No. 46

Diffusion Behavior in Uranium-Plutonium Oxide Fuel Irradiated in a Fast Neutron Flux
R. Natesh, D. R. O'Boyle, and E. M. Butler
Proc. Fourth National Conf. on Electron Microprobe Analysis, Calif. Inst. Technol., Pasadena, Calif., July 16-18, 1969, Paper No. 47

Synthesis and Fabrication of (U,Pu)C Nuclear Fuel Pellets from U-Pu Alloy
P. A. Nelson, D. E. Grosvenor, S. Vogler, N. P. Quattropani, and P. W. Krause
Bull. Am. Ceram. Soc. 48, 863-866 (Sept 1969)

Equilibrium Phase Studies in Fast-Reactor Fuel Alloys
D. R. O'Boyle, D. E. Busch, and J. E. Sanecki
Proc. Fourth National Conf. on Electron Microprobe Analysis, Calif. Inst. Technol., Pasadena, Calif., July 16-18, 1969, Paper No. 45

Structure and Composition of Metallic Fission Product Phases in Irradiated Oxide Fuel
D. R. O'Boyle and A. E. Dwight
Abstract Bull. Met. Soc. AIME Fall Mtg., Philadelphia, Pa., Oct. 13-16, 1969, p. 41

The Application of Signal-Processing Techniques to Signals from Electromagnetic Test Systems
C. J. Renken
Abstract Bull. Met. Soc. AIME Fall Mtg., Philadelphia, Pa., Oct. 13-16, 1969, p. 92

Grain Boundary Damping in Copper-Nickel Alloys
J. T. A. Roberts and P. Barrand*
Abstract Bull. Met. Soc. AIME Fall Mtg., Philadelphia, Pa., Oct. 13-16, 1969, p. 154

Thermal Expansivities, Thermal Conductivities, and Densities of Vanadium, Titanium, Chromium, and Some Vanadium-Base Alloys (A Comparison with Austenitic Stainless Steel)
F. L. Yaggee, E. R. Gilbert, and J. W. Styles
J. Less-Common Metals 19(1), 39-51 (Sept 1969)

*Manchester University, England.

IV. NUCLEAR SAFETY RESEARCH AND DEVELOPMENT

A. LMFBR Safety--Research and Development

1. Coolant Dynamics

a. Sodium Expulsion (R. M. Singer and R. E. Holtz)

(i) Transient Convective Flow and Heat Transfer

Last Reported: ANL-7581, pp. 121-122 (June 1969).

(a) Preparation of Apparatus. The test section for the transient flow loop was completed after considerable difficulty with the 20-mil thermocouples. The thermocouples became very brittle after the high-temperature braze to their adapters; even slight bending could cause shorting of the circuit. One of the thermocouples attached to the wall was lost and several others were replaced by 40-mil thermocouples. The response time for the 40-mil couples is slightly greater, but still reasonable for this experiment.

After being welded into place on the test section, the thermocouples were cycled thermally and then calibrated against each other in an oil bath to 350°F. All thermocouples were within 1.5°F of the mean. Then the test section was washed in ethyl ether to remove the mineral oil. The test section is being given a final leakcheck before being installed in the loop.

(ii) Static Expulsion Tests

Last Reported: ANL-7606, pp. 124-126 (Aug 1969).

A new test section has been installed and data are being collected. This test section has nine wall and three liquid thermocouples as opposed to the three wall and three liquid thermocouples in the earlier system. An improved pressure tap and standoff is also incorporated to prevent thermally shocking the pressure transducer.

(a) Collection and Analysis of Data from Initial System. A preliminary examination of the raw data on vapor growth rates (expulsion velocity) and initial and collapse pressure pulses does not reveal any unexpected results. These data are being analyzed in more detail.

(iii) Forced-convection Expulsion Tests

Last Reported: ANL-7606, p. 126 (Aug 1969).

(a) Preparation of Transient Test Loop. Assembly of the loop is continuing. All the piping, except for the test section, is in place and has been helium-leakchecked. Precise measurements of the test section are underway (distances between pressure taps, internal diameter, etc.). The filament transformers for the electron-beam heater are being installed, as are general loop-control and -monitoring devices.

b. Liquid-Vapor Dynamics (H. K. Fauske and M. A. Grolmes)

Last Reported: ANL-7548, pp. 117-119 (Jan 1969).

(i) Pressure Drop in Sodium Liquid-Vapor Flows. Sodium two-phase critical-flow and void-fraction data reported previously* have shown two-phase critical flowrates in good agreement with the model proposed** and the liquid volume-fraction measurements agree with the well-known Lockhart-Martinelli correlation. In view of these results, detailed axial pressure profiles obtained in the same experiments have been analyzed. Thus we suggest a method for predicting sodium two-phase pressure gradients that: (a) is reasonably accurate, (b) is consistent with critical-flow criteria, and (c) is based on well-known correlations employed in nonmetallic two-phase pressure-drop calculations.

For steady two-phase compressible flow in a horizontal constant-area duct, the overall momentum and continuity equations can be combined to yield the expression for the axial pressure gradient:

$$\frac{dP}{dz} = \frac{-\tau_w(S/A)}{1 - G^2(-dv_{2P}/dP)}, \qquad (1)$$

where $\tau_w(S/A)$ is the wall shear force per unit area, P is pressure, z is distance, τ_w is wall shear, S is channel perimeter, A is flow area, G is mass flowrate. The term v_{2P} is given by

$$v_{2P} = \frac{x^2}{\alpha} v_g + \frac{(1-x)^2}{1-\alpha} v_\ell, \qquad (2)$$

where x is the quality, α is the void fraction, and v_g and v_ℓ are the specific volumes of the vapor and the liquid, respectively. The void fraction α can be evaluated from the Lockhart-Martinelli correlation at equilibrium

*Reactor Development Program Progress Reports for October 1968, ANL-7513, p. 131, and for January 1969, ANL-7548, pp. 117-118.

**Fauske, H. K., Two-phase Critical Flow with Application to Liquid Metal Systems, ANL-6779 (Oct 1963).

quality x. For the sodium data reported here, the use of equilibrium quality is justified on the basis of simultaneous measurements of axial pressure and temperature.

In evaluating the wall shear force, an approach used with success in nonmetallic flows is suggested. The ratio of the two-phase wall shear force to that of liquid alone is taken as $(1 - x)^2/(1 - \alpha)^2$, so that

$$\tau_w \frac{S}{A} = \frac{2c_f v_\ell G^2}{D} \left[\frac{(1 - x)}{(1 - \alpha)}\right]^2, \tag{3}$$

where the friction factor c_f is $0.079/Re^{1/4}$, D is the diameter, G is the mass flowrate, and Re is the Reynolds number.

It is consistent with Eq. (1) that the critical flowrate is given by

$$G_c = [-1/(dv_{2P}/dP)]^{1/2} \tag{4}$$

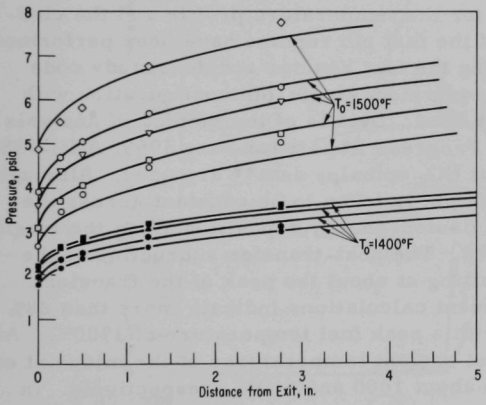

Fig. IV.A.1. Calculated (Curves) and Measured (Data Points) Pressure Profiles for Sodium Liquid-Vapor Flows for Stagnation Temperatures of 1400 and 1500°F

evaluated at the duct exit, again, with the use of equilibrium quality and Lockhart-Martinelli void fraction.

Axial pressure profiles computed according to the above method, i.e., based on given exit pressure and stagnation enthalpy, are compared with sodium two-phase pressure measurements in Fig. IV.A.1. Choked flows occur at the end of the test section, and thus the pressure-drop data shown are for flow regimes in which both momentum and frictional losses are important. Good agreement is illustrated between predicted and measured pressure profiles.

2. Fuel Meltdown Studies with TREAT

a. Transient In-pile Tests with Ceramic Fuels (C. E. Dickerman)

Last Reported: ANL-7618, pp. 128-130 (Sept 1969).

(i) Checkout-2 Mark-II Loop Experiment. The second Mark-II loop-checkout meltdown experiment on an oxide fuel pin (see ANL-7618)

resulted in vigorous coolant expulsions and sharp pressure pulses. Figure IV.A.2 shows the instrument data from the transient. Shown are output from test-section inlet and outlet flowmeters, inlet and outlet pressure transducers, and thermocouples at inlet, outlet, and center. The large, relatively smooth signal for the outlet (variable reluctance) pressure transducer is the radiation response of the instrument. Superimposed on this signal are three prominent spikes.* The maximum pulse recorded by either transducer was only about 35 atm. Conversion of thermal energy to kinetic at the time of failure can be estimated from the flowmeter data. The circulating sodium coolant above the sample (~250 g) was accelerated by about 12 m/sec at the indicated time of failure. This yields a kinetic energy of about 18 J. Including the energy expended in downward expulsion at that time, the total kinetic energy transferred to the sodium at the time of failure is ~25 J. Total energy added to the pin (above the reference level of 400°C) at the time of failure was about 1.88×10^3 J/g. Thus, the energy conversion was less than 2×10^{-3}%. Neutron radiographs taken of the loop after the transient did not reveal any detectable fragments of fuel, indicating that extreme dispersal occurred.

The calculations for the temperature profile and the cladding deformation up to the time of the fuel pin rupture have been performed by the Safety Analysis Section using the fast reactor accident study code SAS1A. In these calculations, an equivalent single-pin configuration with an inlet coolant flow of 4 m/sec is used. Details of the method of analysis have been described earlier (see Progress Report for June 1969, ANL-7581, p. 117) except that the most recent UO_2 enthalpy data** are used. Although the radial power distribution in the pin is taken to be constant across the pin, the observed variation in the fission-energy deposition along the length of the fuel pin is explicitly included. The heat-transfer subroutine of the code predicts the onset of fuel melting at about the peak of the transient. At the time of the pin failure, present calculations indicate more than 88% of fuel to be in the molten state with a peak fuel temperature of 3900°C. At this time, the average cladding and coolant temperatures at the midpoint of the top pellet are calculated to be about 1000 and 660°C, respectively. In other words, the increase in exit coolant temperature is calculated to be 260°C. This increase is significantly larger than the experimental value, and the detailed model of the calculation is being reviewed to trace the possible sources of this discrepancy, and its significance.

The performance of the cladding is calculated by the fuel-deformation subroutine of the code. Present calculations, in agreement with the results obtained for some other TREAT transient experiments (see Progress Report for August 1969, ANL-7606, p. 123), indicate that the

*Figure IV.A.2 shows the radiation response of the outlet transducer in the correct polarity. The checkout-1 data graph, Fig. IV.A.7, p. 129, ANL-7618, has the outlet transducer response negative.

**See ANL-7618, pp. 132-133 (Sept 1969), and also Hein, R. A., and Flagella, P. N., Enthalpy Measurements of UO_2 and Tungsten to 3260°K, GEMP-578 (1968).

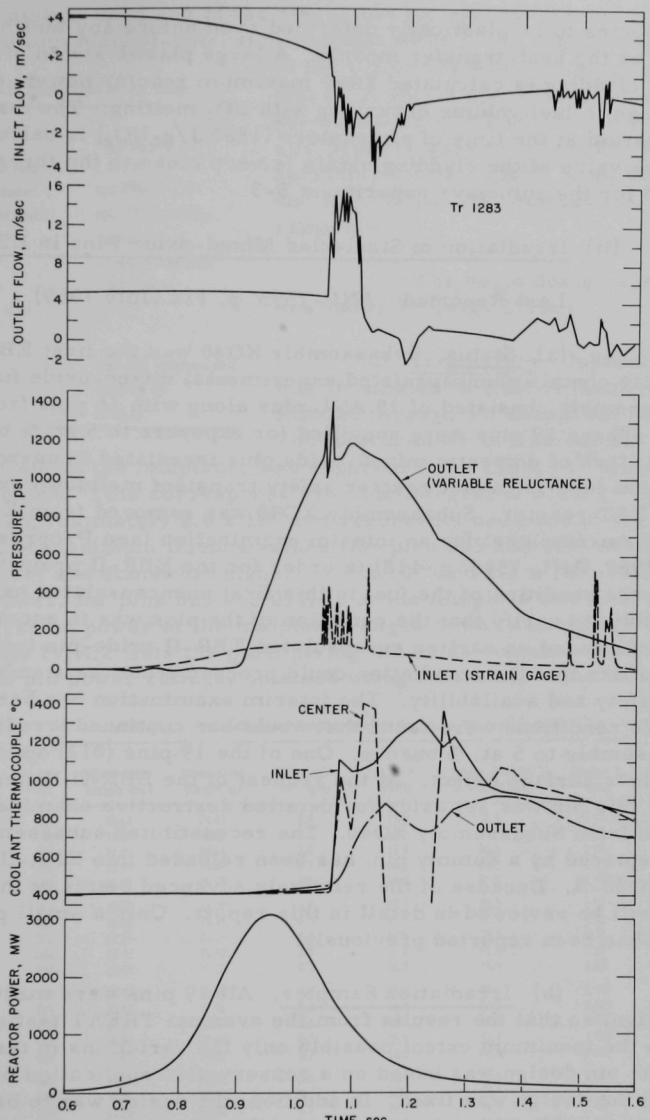

Fig. IV.A.2. Instrument Data from Checkout-2 Mark-II Loop Experiment

cladding begins to be plastically deformed even before any fuel melting is predicted by the heat-transfer module. A large plastic strain of the stainless steel cladding is calculated after maximum reactor power, due to the large change in fuel volume occurring with UO_2 melting. The maximum cladding strain at the time of pin rupture (1880 J/g-UO_2) is calculated to be 5.3%. This value of the cladding strain is very close to the threshold strain calculated for the autoclave experiment S-3.

(ii) Irradiation of Steel-clad Mixed-oxide Pins in EBR-II

Last Reported: ANL-7595, p. 118 (July 1969).

(a) Status. Subassembly XO40 was the first EBR-II subassembly to contain unencapsulated experimental mixed-oxide fuel pins. The subassembly consisted of 19 ANL pins along with 16 pins from General Electric. These 19 pins were specified for exposure to 5 at. % burnup, to provide a stock of domestic mixed-oxide pins irradiated in unencapsulated environment for use in fast reactor safety transient meltdown experiments in the TREAT reactor. Subassembly XO40 was removed from EBR-II at the 3 at. % burnup level for an interim examination (see Progress Report for July 1969, ANL-7595, p. 118) in order for the EBR-II project staff to ascertain the condition of the fuel in this first unencapsulated oxide-pin subassembly, to verify that the condition of the pins was in accord with expectations based on earlier encapsulated EBR-II oxide-pin irradiations, and to confirm that the irradiation could proceed from the standpoint of EBR-II safety and availability. The interim examination has been completed. No conditions were found that would bar continued irradiation of the subassembly to 5 at. % burnup. One of the 19 pins (012) appeared to have a minor surface defect. At the request of the EBR-II Experiment Manager, this pin was set aside for detailed destructive examination as a "lead" pin from Subassembly XO40. The reconstituted subassembly, with pin 012 replaced by a dummy pin, has been reloaded into EBR-II as Subassembly XO40-A. Because of the relatively advanced status of this irradiation, it will be reviewed in detail in this report. Only a small part of the following has been reported previously.

(b) Irradiation Samples. All 19 pins were made to the same design, so that the results from the eventual TREAT testing would reflect to the maximum extent possible only the variations in test conditions. The pin design was based on a conservative application of data available when the design was fixed. In addition, the design was to be similar to those of other EBR-II irradiations then underway, and the design was to be consistent with TREAT experimental apparatus.

Each sample is made in three parts. The central part is the fueled section, which consists of a section of cladding tubing, 17.250 in. long, containing the fuel stack, one natural UO_2 insulator pellet, and one

tantalum disk at each end of the stack, and top and bottom end plugs. Steel top and bottom blanket-extension sections were made separately and welded to the top and bottom end plugs of the central piece. A spiral spacer wire was wound around each completed test pin at the EBR-II site prior to assembly into XO40. Before assembly into a TREAT loop, the steel top and bottom blanket sections are cut off remotely.

TABLE IV.A.1. Specifications for Pin Design

Fuel	
Composition	$(U_{0.8}Pu_{0.2})O_2$
Oxygen-to-metal ratio	1.97-2.00
Uranium enrichment	93% ^{235}U
Plutonium enrichment	91% (^{239}Pu + ^{241}Pu)
Form	Pellets
Pellet density	82-86% of theoretical
Pellet diameter	0.245-0.247 in.
Length of fuel stack	11 in.
Cladding	
Material	Type 304L stainless steel
Diameter	0.290-in. OD
Wall	0.020 in.

The basic design specifications are shown in Table IV.A.1.

(c) Irradiation. Subassembly XO40 was irradiated in EBR-II position 5B2 for Runs 30 through 35, except for Run 30D. The total number of fissions for the centerline at XO40, at the midplane, was reported to be 112 x 10^{18} fissions per gram of oxide. This corresponds to a flux integral of 2.4 x 10^{22} nvt total, of which approximately 2.0 x 10^{22} nvt represents neutrons of 0.8 MeV and above. The maximum fluence values (for pins 025 and 031, nearest the core center) are somewhat higher: 2.6 x 10^{22} and 2.2 x 10^{22}. Maximum fission power, for pins 025 and 031, is at the midplane and is 190 W/g of oxide. Fission power at the midplane ranges down to about 177 W/g for 001. Table IV.A.2 lists the pins, giving the oxide contents and the nominal maximum pin power ratings, obtained using a nominal value of 191 W/g for

TABLE IV.A.2. Pin Loadings and Relative Smeared Density of ANL Pins in XO40

Pin No.	Mixed-oxide Length (in.)	Mixed-oxide Weight (g)	Mixed-oxide W/L (g/ft)	Maximum Power[a] (kW/ft)	Smear Density (% theoretical)	Atom Ratio of Oxygen to Metal
001	10.65	74.41	8.4	16.0	78.5	1.99
002	11.08	78.66	8.5	16.2	79.5	1.99
003	11.07	79.54	8.6	16.4	80.5	1.99
004	10.79	78.45	8.7	16.6	81.8	1.99
006	10.81	79.57	8.8	16.8	82.5	1.99[b]
007	10.88	74.04	8.2	15.7	76.5	1.98
011	10.88	75.45	8.3	15.8	78.0	1.98
012	10.89	76.25	8.4	16.0	78.5	1.98
014	10.93	78.72	8.6	16.4	81.0	1.98
016	10.94	76.05	8.3	16.2	78.0	1.98
018	10.91	78.03	8.6	16.4	80.3	2.005
021	10.87	77.56	8.6	16.4	80.2	2.005
022	10.90	78.01	8.6	16.4	80.3	1.98[c]
023	10.96	79.64	8.7	16.6	81.7	2.005
024	11.00	79.87	8.7	16.6	81.3	2.005
025	10.88	80.02	8.8	16.8	82.6	2.005
026	10.81	80.12	8.9	17.0	82.5	2.005
029	10.81	76.98	8.5	16.2	79.5	1.99
031	11.06	79.23	8.6	16.4	79.8	1.99[d]

[a]Power rating at midplane, figured using a nominal value including gamma heating of 191 W/g of oxide.
[b]Top pellet, 2.005.
[c]Pellets 1-6, 8, bottom are 2.005.
[d]Pellets 1-7 are 2.005.

each of the 19 pins.* Maximum power ratings can be converted to average by dividing by the maximum-to-average ratio of 1.12. These values of fluence and fission rates have a possible uncertainty of 10 to 20%.

Irradiation temperatures were calculated for all 19 pins, using a method described previously.** Maximum outer cladding surface temperatures calculated for the pins ranged between 956 and 988°F. Maximum inner cladding surface temperatures were calculated to fall in the range 1026-1068°F.

(d) 3 at. % Burnup Interim Examination. The nondestructive interim examination at 3 at. % burnup consisted of the following:

1. visual inspection and optical photography;
2. neutron radiography;
3. diameter measurements;
4. weighing;
5. temperature measurements of four selected elements.

After removal from the reactor, the subassembly was cleaned of sodium and disassembled following standard Fuel Cycle Facility (FCF) procedures. Sodium remaining on the subassembly surfaces was removed by wet argon gas, followed by a demineralized water flush.

The pins were given a general visual inspection through a FCF air cell window, then viewed and photographed close up using the FCF periscope. Condition of the 19 pins appeared to be good, with the possible exception of pin 012. Some areas were covered with what appeared to be a thin surface film of sodium oxide, and there were some small surface film spots, but no macroscopic deposits. The spiral spacer wires were still apparently taut and in good contact with the pin. The largest spacer-cladding gap noted was estimated conservatively to be less than 0.005 in.

Neutron radiography showed no internal defects. The pellet structure visible by X-ray examination before irradiation was no longer prominent, and evidence of central voids could be seen in all pins. Small but definite migration of fissionable material into the natural UO_2 end pellets was observed.

*Pins 025 and 031 have an estimated gamma heating rate in the oxide of 7 W/g additional for a total 197 W/g at the midplane. Gamma heating in the oxide of pin 001 is estimated at 6 W/g, for a total of 183 W/g. In view of experimental uncertainties, a single nominal power rating for all of the 19 pins was adopted for Table IV.A.2.

**Cushman, R. A., and McGinnis, F. D., EBR-II Reactor Heat Transfer: Experience with an Operating LMFBR, presented at the Tenth National Heat Transfer Conference, August 11-14, 1968, Philadelphia, Pa.

A nominal increase of cladding diameter $\simeq 0.3\%$ was measured. There were no anomalies in pin weights or pin temperatures.

b. Experimental Support (C. E. Dickerman)

Last Reported: ANL-7618, p. 131 (Sept 1969).

(i) Shipping Cask. The second package of vendor documentation for the TREAT Mark-II loop shipping cask was received. This cask will be required for TREAT experiments because there is no cask available that meets the AEC Department of Transportation regulations and that will hold the Mark-II loop (or similar TREAT irradiation apparatus). The second package consists of the vendor (i.e., shop) version of the ANL design drawings, and includes minor revisions. The entire vendor package is now under review to ensure that the cask will satisfy the detailed technical and safety requirements. Following the review and final agreement on any discrepancies, the design and analysis data package will be forwarded to the AEC for approval.

c. TREAT Operations (J. F. Boland)

(i) Reactor Operations. Pretransient neutron radiographs were obtained of ORNL Experiments TR-1 and TR-2, and a calibration transient was run on Experiment TR-1. These experiments contain fuel elements consisting of pelleted and sphere-pac PuO_2-UO_2 fuel clad in stainless steel. The fuel elements are in sodium-filled capsules. Data from the calibration transient agreed reasonably well with calculations, and the reactor is being loaded for the test transients on these experiments.

A partially bonded EBR-II fuel element was subjected to a flattop transient in a Mark-I packaged sodium loop. Posttransient neutron radiographs did not show any indications of cladding failure.

Neutron radiographs were made of 18 groups of EBR-II experimental capsules, one capsule from INC, two Mark-I sodium loops for EBR-II fuel experiments in TREAT, and TREAT experimental capsule S-4.

A new type of Statham pressure transducer was subjected to a transient irradiation to determine its sensitivity to radiation. The data showed this transducer was unsuitable for use on TREAT experimental capsules.

(ii) Development of Automatic Power Level Control System. Delivery of the hydraulic control-rod-drive system has been further delayed because the subcontractor again delivered unacceptable cylinders for the hydraulic actuators. An order for the cylinders is being placed with a vendor who has recently made similar cylinders that met our contractor's specifications.

3. Materials Behavior and Energy Transfer (M. G. Chasanov)

a. Theoretical Extrapolation of Measured Physical-property Data to Higher Temperatures

Not previously reported.

Knowledge of the pressure within an operating fuel pin is of importance to the reactor safety program. At normal operating temperatures, pressure from the buildup of gaseous fission products in the void, crack, and plenum regions of the fuel pin significantly contributes to the stresses placed on the cladding material. Under accident conditions, the combined vapor pressure of fission products and fuel may serve as a ballast force causing molten fuel to be extruded through a rupture in the cladding if such a rupture should occur. The vapor pressure is thus one of the factors that needs to be considered in determining the extent of fuel-coolant interaction.

The thermodynamic data needed for the calculation of partial vapor pressures of the fission products and of the fuel at the very high temperatures that may be reached during a reactor accident cannot be directly obtained by experimental means. Consequently, it is necessary either to find some basis on which to extrapolate existing experimental data taken at low temperatures to higher temperatures or to perform statistical-mechanical calculations of the thermodynamic properties based upon observed spectroscopic parameters.

Efforts have initially been placed on the development of a basic computer program suitable for calculating vapor pressures of fuel and fission products at normal operating temperatures; this same program will later be applicable to calculations of vapor pressures at very high temperatures when appropriate thermodynamic data are available.

For a fixed temperature, fuel density, relative void volume, percent burnup, and preburnup oxygen-to-uranium (O/U) ratio of the fuel, a set of simultaneous equations must be solved. These consist of (1) nonlinear equilibrium relations between the vapor species, oxygen, and the stable condensed phase of each fission product element and of the fuel, (2) mass constraints imposed by initial quantities and preburnup O/U ratio of the oxide fuel and by fast-neutron fission-product yields, and (3) an equation relating oxygen pressure to the O/U ratio of the fuel. The assumptions made are (1) that all vapor species are released to the void volume which is at constant and uniform temperature and (2) that the condensed fuel and fission-product phases are immiscible and have unit activity coefficients. Although there are as many unknown quantities as equations, it is found that the concentrations of all species depend simply on the O/U ratio of the

condensed fuel. By estimating the final (after-burnup) fuel composition, the concentrations of all species and a revised value of the final O/U ratio are obtained. Successive iterations are performed until the estimated and revised values of the after-burnup O/U ratio agree to within any required accuracy. Partial vapor pressures of fission products and fuel are then calculated from this final value.

Future work in this area will include updating and extension to higher temperatures of the necessary thermodynamic data, accounting for the possibility of compound formation between several fission-product elements, and attempts to improve upon the simplifying assumptions enumerated above.

4. 1000 MW(e) Safety Analysis Studies

a. Contract Management, Technical Review, and Evaluation (L. W. Fromm)

Not reported previously.

(i) Babcock & Wilcox Co. Subcontract. A contract has been established with Babcock & Wilcox for a 1000-MWe LMFBR Accident Analysis and Safety System (A^2S^2) Design Study, as part of the LMFBR Plant Safety Studies program. B&W has been working on the program definition phase and on Phase I, the survey of malfunctions and safety problems.

(a) Program Definition Phase. B&W prepared a detailed work plan on all phases of the work; it delineates the analytical tools, methods, and technical approach to be taken on all activities. The work plan was submitted to the Laboratory, which approved commencement of the Phase-I and -II work.

(b) Phase I: Malfunction and Safety Problem Survey. The malfunction survey was completed for those safety problems that have the potential for furnishing the design bases for core protective systems and engineered safety features. The cataloging of the potential malfunctions and faults is about 75% complete. In addition to the potential malfunctions and faults, the catalog will also include possible protective actions, monitored variables, and engineered safety features. Survey results also will be displayed graphically in a fault-tree diagram, which is ~90% complete.

Technical meetings were held between ANL and B&W on September 4 and 5, 1969 to exchange ideas on LMFBR safety-related activities and to explore the availability of analytical methods or models that could be applied to this study. B&W described computer codes such as FARED, TART, MARS, FIRE, and BANGO, as well as their applications.

ANL described the SAS1A, SAS1B, and VENUS codes, and presented information on some of the safety models being investigated at ANL. B&W is preparing a technical note that summarizes the methods and computer codes to be used in the A^2S^2 study and outlines the reasons for selecting these methods.

(c) Phase II: Accident Analysis and Selection of Safety Features. Preliminary literature survey and evaluation work has begun on Phase II. This work is mainly in the areas of accident-initiating conditions, accident analyses, and candidate safety features.

5. Violent Boiling (R. O. Ivins)

a. Violent Boiling with Molten Fuel and Sodium (D. R. Armstrong)

(i) Fragmentation and Mixing Experiments (D. Cho)

Last Reported: ANL-7581, pp. 125-127 (June 1969).

The process of breakup and dispersion of molten fuel in coolant depends on: (1) boiling characteristics at molten fuel-coolant interfaces, (2) initial dynamic conditions of contact, which might be determined by fuel-failure modes, and (3) arrangement, such as configuration of fuel pins and coolant channel. The boiling characteristics might be altered, depending on initial dynamic conditions of contact and geometrical arrangement. The present fragmentation studies are directed toward understanding the effects of violent boiling and initial dynamic conditions in a simple geometrical arrangement.

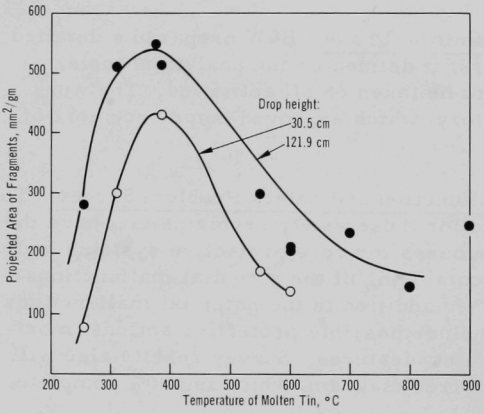

Fig. IV.A.3. Fragmentation of Molten Tin Quenched in Water

The effects of violent boiling can be seen in terms of molten-metal temperatures and the degree of coolant subcooling. Figure IV.A.3 shows the results obtained when a small amount of molten tin (<1 g) was dropped into water at room temperature. The results clearly indicate that the most extensive breakup occurs at metal temperatures near 400°C. A series of experiments has been performed to examine the effects of different degrees of water subcooling; the results are being analyzed.

b. Simulations of Fuel Dispersal (J. J. Barghusen)

Last Reported: ANL-7618, pp. 133-134 (Sept 1969).

(i) In-pile Experiments on Material Interactions during Nuclear Transients

(a) In-pile Experiments with UO_2 in Piston Autoclave. A fourth meltdown experiment (S-4) was performed in the sodium-filled piston autoclave at the TREAT reactor facility to measure pressures generated and momentum transfer during a nuclear transient of energy sufficient to rupture stainless steel-clad UO_2 fuel specimens. The experiment involved a reactor transient of 1050 MW-sec, resulting in a fission-energy release in the test fuel of 720 cal/g UO_2. The value of peak reactor power was 6650 MW, and the reactor period was 34 msec.

The fuel loading and configuration for this experiment were identical to those used for Experiment S-3 (see Progress Report for February 1969, ANL-7553, pp. 113-116). The test fuel loading consisted of an array of five rods containing 10%-enriched UO_2 pellets and four dummy rods filled with helium. Each fuel rod contained about 41 g UO_2, so there were 205 g in the entire array. The sodium (197 g) was heated to ~200°C before the transient.

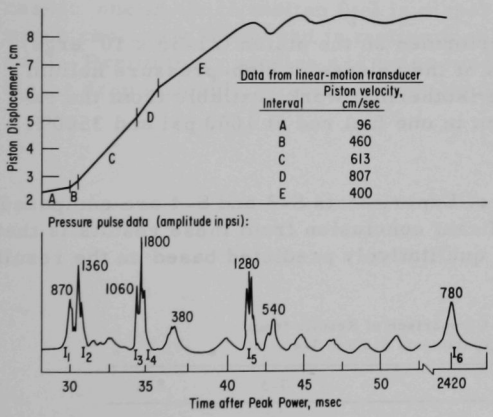

Fig. IV.A.4. Linear Motion and Pressure Response for Sodium Autoclave Test S-4

Preliminary results were reported in ANL-7618. Additional data on the nature of the pressure pulses and the piston response have been obtained. The pressure-response record (see Fig. IV.A.4) shows five large, discrete pressure pulses, and several minor pulses of amplitudes less than 550 psi. The first two pulses (I_1 and I_2) occurred about 30 msec after peak power. The integrated reactor power at the instant of the first pulse was about 705 MW-sec, equivalent to a fission-energy release in the test fuel of about 480 cal/g UO_2. These pulses were followed by a large pulse composed of two peaks less than 0.3 msec apart. The first peak of the double pulse occurred 34.4 msec after peak power and had an amplitude of 1060 psi; the second peak had an amplitude of 1800 psi. Although it is not certain that this double pulse represents separate pressurization

events, both peaks will be considered as individual impulses (I_3 and I_4). Impulse I_5, 1280 psi, occurred 42 msec after peak power. The final pulse (I_6) was significantly delayed, occurring 2.4 sec after peak power. This pulse is probably the result of flashing of superheated liquid sodium. At the instant of the pulse, the temperature of the sodium decreased from ~1700 to ~1000°C. Flashing of sodium at 1700°C would generate a pressure of ~900 psi.

The low-amplitude oscillations shown in Fig. IV.A.4 have a period of ~2 msec. Although several possible physical situations have been considered to explain this phenomenon, such as displacement of the transducer diaphragm or the presence of a small gas bubble in the tube connecting the transducer to the sodium cavity, it is not possible to attribute with certainty the observed behavior to any particular physical situation.

The output of the linear-motion transducer is reproduced in Fig. IV.A.4. As in the case of Experiment S-3, acceleration of the piston occurred simultaneously with the generation of the pressure pulses. The maximum piston velocity was 807 cm/sec, which occurred coincidentally to the 1800-psi pressure pulse (Impulse I_4). The apparent slowing down (deceleration) of the piston from 807 to 400 cm/sec (Interval E) might have been due to sodium bypassing the piston through machined slots in the piston cylinder during the final 2 cm of travel and forcing the sodium into the shock absorber.

The work performed on the piston ($21\text{-}36 \times 10^6$ ergs) can be explained readily in terms of the release of high-pressure helium bond gas from the fuel rods. The isothermal work available from the expansion of 0.8 cm^3 (STP) of helium in one fuel rod at 1000 psi and 3500°K to 25 psi is 38×10^6 ergs.

The results of Experiments S-3 and S-4 are compared in Table IV.A.3. The most significant conclusion from these results is that all observations from S-4 can be qualitatively predicted based on the results from Experiment S-3.

TABLE IV.A.3. Comparison of Results from Meltdown Experiments S-3 and S-4

	S-3	S-4
Reactor energy, MW-sec	669	1050
Fission energy in test fuel, cal/g UO_2	460	720
Reactor period, msec	53	34
Peak power, MW	2664	6650
Amplitude of largest pressure pulse, psi	540	1800
Impulse from pressure pulse, dyne-sec	8.5×10^4	18.4×10^4
Average pulse duration, msec	2.3	0.9
Maximum piston velocity, cm/sec	472	807
Maximum piston impulse, dyne-sec	7.7×10^4	9.5×10^4
Fission energy at first pressure pulse, cal/g UO_2	444	480
Maximum work done by piston, ergs	17.1×10^6	35.8×10^6
Maximum event temperature, °C	1100	>3000
Conversion nuclear to mechanical energy, %	0.7×10^{-3}	1.4×10^{-3}

c. Mathematical Models of Fuel-Coolant Dynamics (D. R. Armstrong)

Last Reported: ANL-7595, pp. 122-127 (July 1969).

(i) Fuel-Sodium Interaction and Heat Transfer Leading to Pressure Generation

(a) Parametric Model of Pressures due to Dispersal of Molten Fuel (D. Cho)

A reliable model for pressure generation resulting from molten fuel coolant interactions must take into consideration the processes of fuel-coolant interdispersion, heat transfer, and coolant expansion. A major question here concerns the interaction between two competing processes, i.e., the heating of coolant (which produces pressures) and the expansion of coolant (which reduces pressures). The question has been examined previously by employing a parametric model* where overall heat-transfer rates enter as a parameter.

A more detailed analysis than the parametric model can be made by solving simultaneously the pertinent equations of state, motion, and energy. It appears convenient to consider separately two cases: one in which molten fuel is dispersed in coolant, and the other in which coolant is dispersed in molten fuel. The latter case will be examined first. Preliminary studies are being made for the expansion of a cold bubble or drop suddenly formed in a hot liquid.

*See Progress Reports ANL-7561, pp. 100-103 (March 1969); ANL-7577, pp. 192-195 (April-May 1969); ANL-7595, pp. 122-127 (July 1969).

PUBLICATIONS

Discussion: A Pressure Pulse Model for Two-Phase Critical Flow and Sonic Velocity (by F. J. Moody)
H. K. Fauske and M. A. Grolmes
J. Heat Transfer 91(3), 381 (Aug 1969)

The Reaction of a Molten Sodium Spray with Air in an Enclosed Volume. Part I. Experimental Investigation
T. S. Krolikowski, L. Leibowitz, R. E. Wilson, J. C. Cassulo, and S. K. Stynes*
Nucl. Sci. Eng. 38, 156-160 (Nov 1969)

The Reaction of a Molten Sodium Spray with Air in an Enclosed Volume. Part II. Theoretical Model
T. S. Krolikowski, L. Leibowitz, R. O. Ivins, and S. K. Stynes*
Nucl. Sci. Eng. 38, 161-166 (Nov 1969)

On the Use of Non-Metallic Fluids to Simulate Sodium Expulsion
R. M. Singer
Nucl. Eng. Design 10(1), 72-78 (May 1969)

On the Role of Inert Gas in Incipient Boiling Liquid Metal Experiments
R. M. Singer and R. E. Holtz
Intern. J. Heat Mass Transfer 12(9), 1045-1060 (Sept 1969)

The Equivalence of Dynamic Loads for the Final Plastic Deformation of a Tube
C. K. Youngdahl
Proc. First Int. Conf. on Pressure Vessel Technology, Delft, The Netherlands, Sept. 29-Oct. 2, 1969. ASME, New York, 1969, pp. 89-100

*Wayne State University.